RADIATION DAMAGE IN $KMgF_3$:Mn AND $NaMgF_3$

By

MARK ALLEN YOUNG

Bachelor of Science

Oklahoma State University

Stillwater, Oklahoma

1972

Submitted to the Faculty of the Graduate College
of the Oklahoma State University
in partial fulfillment of the requirements
for the Degree of
DOCTOR OF PHILOSOPHY
July, 1976

RADIATION DAMAGE IN $KMgF_3$:Mn AND $NaMgF_3$

Thesis Approved:

Thesis Adviser

Dean of the Graduate College

ACKNOWLEDGEMENTS

The author is indebted to many friends and associates without whose constant assistance and advice this work could not have been realized. To Dr. E. E. Kohnke, Thesis Chairman, go a special thanks for his constant encouragement and for providing numerous stimulating discussions throughout the course of this study. Gratitude is further expressed to Dr. L. E. Halliburton who aided immensely in the analysis and interpretation of the ESR data and who was constantly available for consultation and advice in this regard. Financial support in the way of a Research Assistantship in conjunction with the Radiation Safety Program throughout the course of the graduate work is also gratefully acknowledged.

Finally, the author wishes to express his deepest gratitude and appreciation to his family and closest friends for their moral support throughout his university endeavors.

TABLE OF CONTENTS

LIST OF TABLES

LIST OF FIGURES

LIST OF FIGURES (Continued)

LIST OF FIGURES (Continued)

CHAPTER I

INTRODUCTION

The study of radiation damage in insulating materials has become an important part of solid state physics. The interest in this field was originally stimulated by the need to comprehend the problems introduced by radiation effects in fission reactors. In recent years, the feasibility of producing power from controlled thermonuclear fusion has grown, and with this development will come a renewed need to understand the characteristic radiation problems involved (1).

Interest in radiation damage extends well outside the realm of reactor technology, however. The potential use of radiation induced defects for information storage has been considered (2). Somewhat more exotically, the radiation damage features in lunar dust grains have been analyzed to yield information concerning the past and present activity of the Sun (3).

In order to fully understand the effects produced by the interaction of radiation with matter so that potential uses of these effects may be efficiently explored, a thorough comprehension of the underlying physics is mandatory. Furthermore, investigations of radiation effects for their own sake are important since such work can lead to insights into the properties of imperfections in solids.

Investigations of radiation damage in ionic crystals, and in particular the alkali halides, have been carried out extensively (4,5).

This has come about primarily because such crystals are easily studied by the experimental techniques employed in optical spectroscopy and electron spin resonance (ESR). Such investigations have yielded a wealth of knowledge concerning the defects formed by radiation.

The irradiation of ionic crystals results in producing defects which may be grouped into three broad classes (6): (A) electronic defects, which are associated with changes in valence states; (B) ionic defects, which involve displacement of lattice ions; and (C) gross imperfections, such as dislocation loops and voids. In the present study, emphasis was placed on defects which fall into the first two classes, and a further description of these defects will now be given.

Changes in valence states may occur for impurities introduced into the crystal intentionally (doped) or inadvertently in the growth process. These are the simplest radiation end products, and many examples may be found in the literature (7-12). The change of valence of impurities arises from capture of electrons or holes and may vary considerably depending on the type of impurity and the particular host lattice.

The electronic defect which is of importance in the investigation being reported here is the self-trapped hole or V_K center. The electronic structure of the V_K center in the alkali halides was first analyzed by Castner and Känzig (13). From the analysis of the V_K center ESR spectra, the configuration was found to consist of two nearest-neighbor <110> halide ions that have given up an electron (trapped a hole) and have subsequently moved together to form a halide $[X_2^-]$ molecular ion. The electron will then be trapped at some other defect within the crystal, commonly at an impurity. Thus the impurity

(electron trap) concentration within a crystal can greatly alter the number of V_K centers formed. Optical absorption bands associated with the V_K center have also been identified (14-16).

However, the study of V_K centers has not been limited to the alkali halides. Self-trapped holes have also been investigated in a number of other compounds, including the ammonium halides (17), cubic alkaline earth halides (18,19), and $KMgF_3$ (20). Furthermore, the study of hole centers is now being extended to materials with lower symmetry crystal structures such as tetragonal MgF_2 (21).

Ionic defects consist mainly of vacancies, vacancy aggregates, and interstitials. Extensive work has been carried out on negative-ion vacancies in ionic compounds. The anion vacancy that contains an electron is referred to as the F center. Spin resonance measurements on this center were first performed by Hutchison (22). The hyperfine interaction of the F center with surrounding nuclei can be resolved by means of ENDOR (electron nuclear double resonance), first developed by Feher (23). This technique yields detailed information concerning the spatial dependence of the charge density.

Prolonged irradiation, special heat treatment, or optical bleaching will produce vacancy aggregates. The basic F center aggregates have been designated M centers (two F centers) and R centers (three F centers). No direct observations have been made on positive-ion vacancy aggregates in halide compounds.

Displacing a lattice atom or ion from its normal lattice site will result in the production of both a vacancy and an interstitial. The combined defect is referred to as a "Frenkel defect". The interstitial species which has been studied extensively in the alkali halides is

referred to as the H center. The electronic structure of the H center was first analyzed in detail by Känzig and Woodruff (24). It was found that the fundamental interstitial produced in the alkali halides is a halide atom which has bonded to a lattice halide ion, thus sharing a single lattice site. The resulting center takes on the form of a molecular ion reminiscent of the V_K center. The structure of the H center in $KMgF_3$ has been determined, and a model has been developed based on a molecular ion configuration similar to that found for the alkali halides (25). The structures of the fundamental defects produced in halide materials are illustrated in Figures 1 and 2 for a NaCl-type lattice. A comprehensive review of the properties of electron and hole centers has been given by Klick (26) and Kabler (27) respectively. Having introduced the basic defects produced by the irradiation of halide crystals, it now remains to discuss the basic mechanisms by which these defects are formed.

At the outset of the formulation of the theory of radiation damage, before the identities of all the defects had been firmly established, there existed some controversy as to whether the primary defects formed in halide compounds were Frenkel defects or Schottky pairs consisting of cation and anion vacancies. The Schottky pair model originated from a suggestion by Seitz (28) that electronic deexcitation would occur at dislocations resulting in an "evaporation" of cation and anion vacancies from the dislocation. This model was subsequently rejected following the identification and characterization of the H center (24) and after simultaneous measurements of the expansion of a crystal and its increase in lattice constant yielded results which were inconsistent with a model based on the production of Schottky pairs (29). Thus Frenkel defects

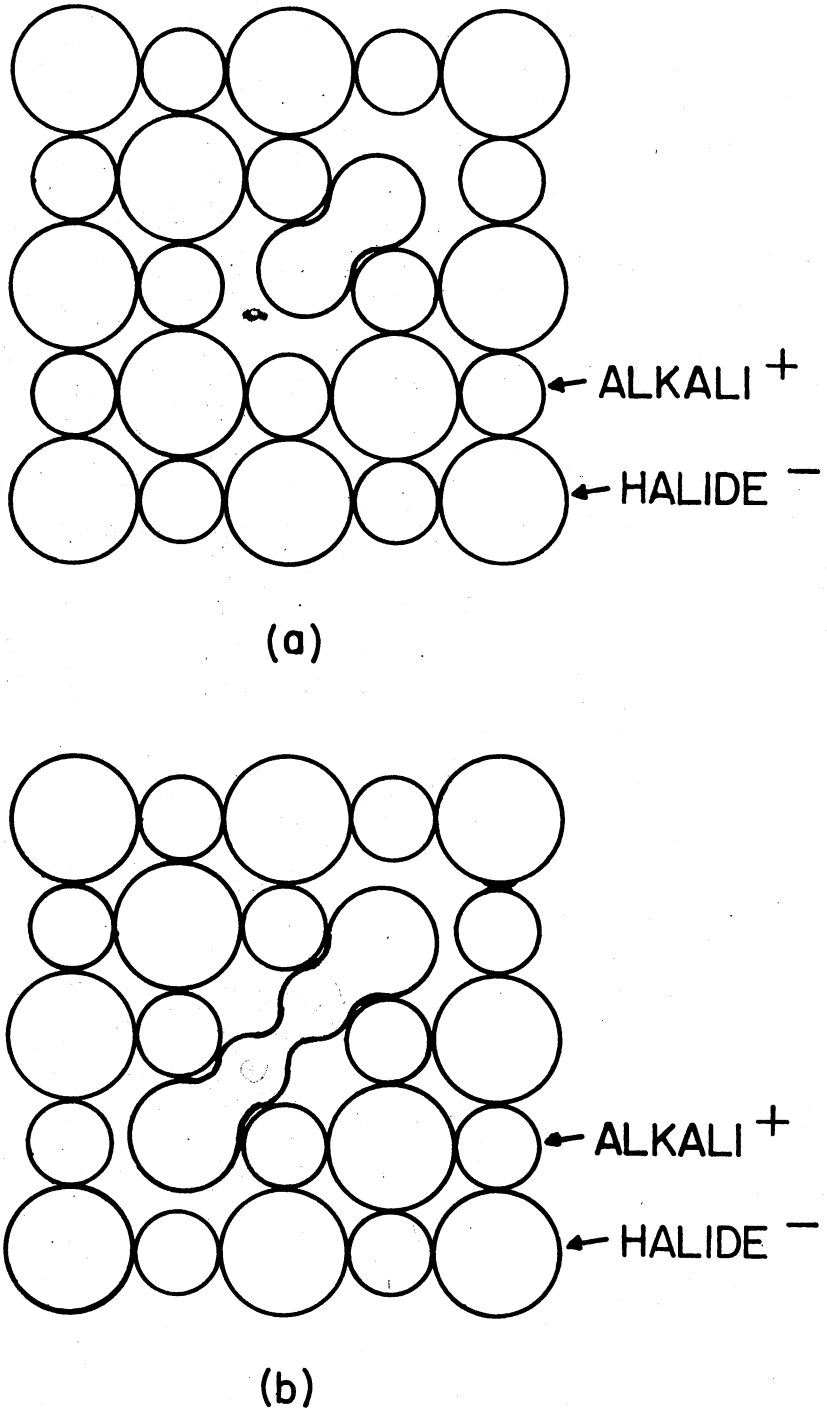

Figure 1. The Structure of the (a) V_K Center and (b) H Center in the Alkali Halides

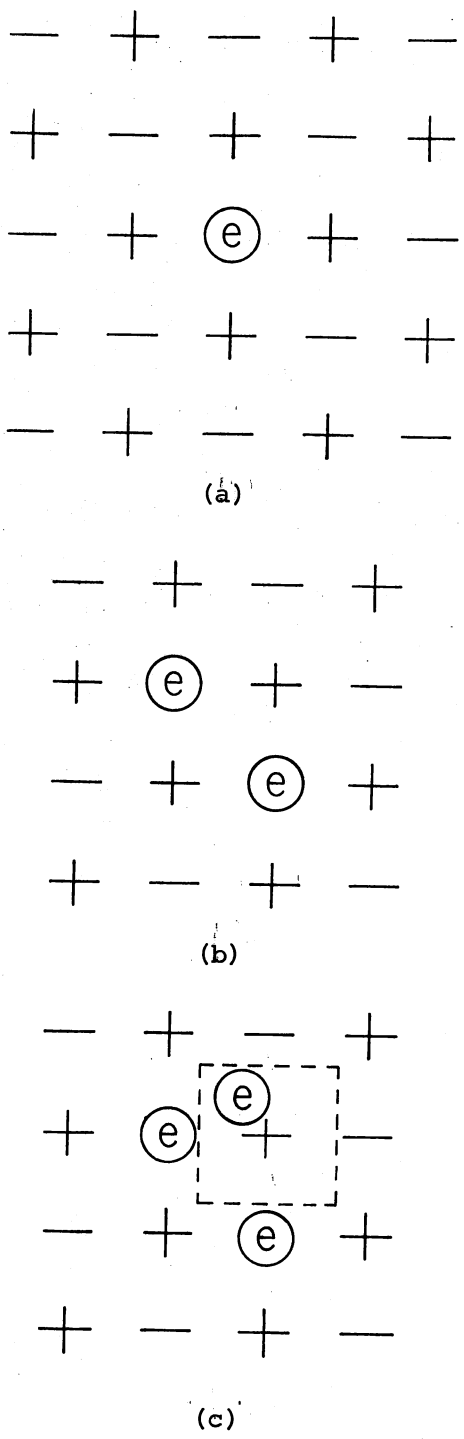

Figure 2. The Structure of the (a) F, (b) M, and (c) R Centers in the Alkali Halides

are the primary radiation damage products.

In the alkali halides defect production has been found to proceed quite efficiently, with Frenkel defects being formed through the mere application of ultraviolet light (30). Thus defect production must proceed through a conversion of electronic excitation energy into a form suitable for producing lattice defects, rather than by means of elastic collisions. Such a "radiolysis" process must then proceed through three basic steps: (I) an electronic excitation resulting in the production of a charged electronic defect in the lattice, (II) the conversion of this energy into kinetic energy of a lattice ion, and (III) the motion and final stabilization of the ion.

The initial electronic excitation leading to the production of a charged defect in the lattice is provided by the absorption of energy from the radiation field. When the source of radiation is high energy electrons, there will be a scattering of the incident electrons with the electrons of the crystal. An outline of the processes by which this energy is ultimately dissipated in the crystal may be found in nuclear physics texts (31) and will not be discussed here.

One of the first attempts to explain Frenkel defect production through radiolysis in the alkali halides was made by Varley (32) who suggested that the initially charged defects consisted of doubly ionized halide ions. If the doubly charged states had sufficiently long life-times, then the ions could be electrostatically ejected from their lattice positions into interstitial positions. However, calculated production efficiencies were too low compared with the experimental production rate for Frenkel defects at liquid helium temperatures (33). Furthermore, it is doubtful that the double-ionization state has a long

enough lifetime to allow ions to move before an electron is recaptured (34).

The presently accepted model for defect production in the alkali halides was arrived at through the observation that there existed a relationship between electron-hole recombination and the production of ionic defects. The so-called fundamental luminescence which arises through recombination of self-trapped holes with electrons during irradiation with ultraviolet light or x-rays was observed in KI to cease at a temperature (~ 100 K) at which F center production increased by an order of magnitude (35). This anticorrelation between fundamental luminescence and F center production has also been observed for a number of other alkali halides (36). The definitive experiment showing that electron-hole recombination does in fact produce Frenkel pairs was performed by Keller and Patten (37). In this experiment electrons trapped at impurities (Tl) in KCl were released at low temperature (25 K) by bleaching into the impurity absorption band, and the subsequent recombination with $[Cl_2^-]$ centers resulted in the formation of H centers in direct proportion to the number of self-trapped hole centers destroyed.

Thus radiolysis proceeds through the initial formation of electron-hole pairs (excitons). The formal theory for the excitonic production of defects in the alkali halides was originally put forth independently by Pooley (38) and Hersh (39). The theory assumes that the excitons take on the molecular ion configuration ($X_2^{=*}$). Their formation may be understood in terms of an initial ionic excitation:

$$X^- + h\nu \rightarrow X^{-*} \qquad (1)$$

followed by the formation of the self-trapped exciton.

$$X^{-*} + X^{-} \rightarrow X_2^{=*} \tag{2}$$

The $X_2^{=*}$ molecule may then deexcite through several distinct channels. The most important deexcitation paths are:

$$X_2^{=*} \rightarrow 2X^{-} + h\nu \tag{3}$$

- restoring the lattice and yielding luminescence;

$$X_2^{=*} \rightarrow 2X^{-} + h\nu_p \tag{4}$$

- resulting in phonon emission,

$$X_2^{=*} \rightarrow X_{int} + X^{-} + \text{F center} \tag{5}$$

- resulting in the production of Frenkel defects. Note that in the last deexcitation path it is the uncharged Frenkel pair that is produced (interstitial atom and F center) rather than the charged pair (interstitial ion and α center (halide vacancy)). This is supported by the experiments done by Ueta and co-workers (40) on the production of F centers in KCl through application of short (30 nsec) pulses of high energy electrons and then comparing the results for both virgin and preirradiated samples.

The interstitial atom moves from the vacancy (F center) via a replacement sequence along close-packed rows (<110> directions). Experiments have been performed (41) which show the importance of having focusing directions within the crystal so that the replacement sequence may proceed efficiently.

Radiation damage studies have been extended beyond the alkali halides to include such materials as the alkaline earth fluorides (42,43), $KMgF_3$ (44), and $RbMgF_3$ (45), where again the basic photochemical damage processes found for the alkali halides appear to be operative.

The presence of significant concentrations of impurities in halide compounds can affect the production rate of radiation-induced Frenkel defects in these materials (6). The production rate at lower temperatures may be enhanced through increased interstitial stabilization (46) and near room temperature may be suppressed as a result of "short-circuiting" of the excitonic production mechanism (47). Transition metal impurity ions are expected to suppress the damage rate since electron-hole recombination energy may be transferred to these ions resulting in excitation of the 3d optical transitions. The influence of transition metal ions on the defect production rate in the alkali halides has not been extensively studied because of the complexities introduced by the necessity for charge compensation (cation vacancies), although a paramagnetic center associated with Mn^{2+} in NaCl has been investigated by Itoh and co-workers and attributed to a Mn^{2+}-interstitial ion complex (48).

In $KMgF_3$ divalent transition metal ions may be introduced without the need for charge compensation. This compound is therefore more suitable for investigating the effect of 3d impurity ions on the excitonic radiation damage mechanism. As shown in Figure 3, $KMgF_3$ has the ideal (cubic) perovskite crystal structure. Based on their ionic sizes, transition metal ions are expected to substitute exclusively for Mg^{2+}

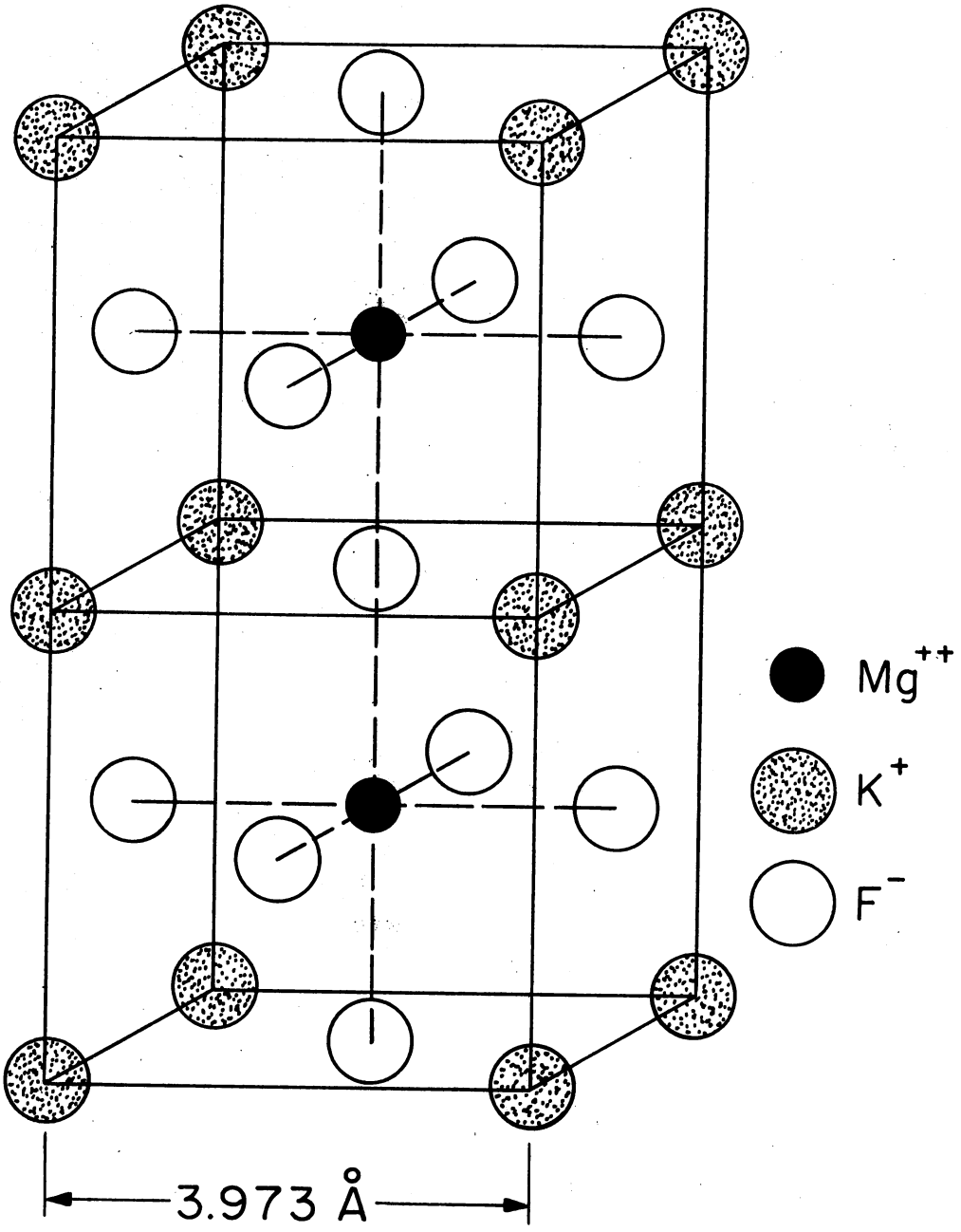

Figure 3. Crystal Structure of $KMgF_3$

in this material.*

In order to investigate the suppression of radiation damage in halide compounds due to the presence of transition metal impurities, Sibley and co-workers have conducted a series of radiation damage studies on $KMgF_3$ doped with Mn^{2+}. The initial study (50) confirmed that the presence of Mn^{2+} will partially suppress F center production in $KMgF_3$. This work also resulted in the characterization of an optical absorption band which was tentatively attributed to Mn^{2+} ions perturbed by an adjacent F center. The defect was shown to have <100> symmetry and could be selectively destroyed, but not reoriented, with optical bleaching. In a subsequent investigation (51), a detailed analysis of the luminescence associated with this center was performed, and it was determined that the oscillator strengths of the optical transitions for the perturbed Mn^{2+} ions were enhanced by approximately three orders of magnitude over those observed in $KMnF_3$. Recently, a second Mn^{2+}-F center type complex has been reported in $KMgF_3$ (52). This second center differs from the initially reported defect both in luminescence and optimum production conditions. The initially reported defect is produced primarily at 77 K or below and is currently believed to be a Mn^{2+}-F center-interstitial complex. The recently observed center is produced primarily at room temperature and is thought to be a Mn^{2+}-F center pair.

One objective of the present study was to use ESR to investigate radiation induced defects associated with Mn^{2+} in $KMgF_3$ in an effort to substantiate the defect models set forth by Sibley and co-workers, and

---

*Although the rare earth ion Eu^{2+} has been found to substitute primarily for K^+ (49).

thereby contribute to the present understanding of the suppression of radiation damage in halide compounds through the inclusion of transition metal impurities. These investigations were successful in identifying the ionized form of the Mn^{2+}-F center pair (Mn^{2+}-fluorine vacancy center). In a later section of this report, a complete analysis of the ESR spectrum associated with this defect will be given, together with details of its production and thermal decay characteristics. A treatment of the thermoluminescence obtained following the same irradiation procedure that produced the Mn^{2+}-fluorine vacancy center will also be given.

A further objective of this study was to determine the structure of the intrinsic self-trapped hole centers in $NaMgF_3$ as part of the extension of investigations of radiation damage in lower symmetry materials. $NaMgF_3$ is a pseudo-perovskite structured material strictly isomorphic with the original perovskite $CaTiO_3$ (53). The compound occurs naturally as the mineral neighborite and was first identified in the dolomitic oil shale of the Eocene River formation of South Ouray, Uintah County, Utah. Synthetic crystals were used in the present study.

X-ray powder diffraction patterns taken at different temperatures have shown (53) that $NaMgF_3$ is cubic above $900^{\circ} \pm 25^{\circ}C$ with a = 3.955Å, tetragonal from $760^{\circ}C$ to $900^{\circ}C$ with a = 3.942Å and c = 3.933Å (at $760^{\circ}C$), and orthorhombic below $760^{\circ}C$ with unit cell dimensions at room temperature of a = 5.363Å, b = 7.676Å, and c = 5.503Å. The room temperature crystal structure of $NaMgF_3$ is shown in Figure 4 (after Megaw (54). It can be seen that the structure is an orthorhombic tilt system. The underlying reason for this tilting, when compared to $KMgF_3$, may be understood upon examination of the ionic radii of the Na^+ ions (.95Å)

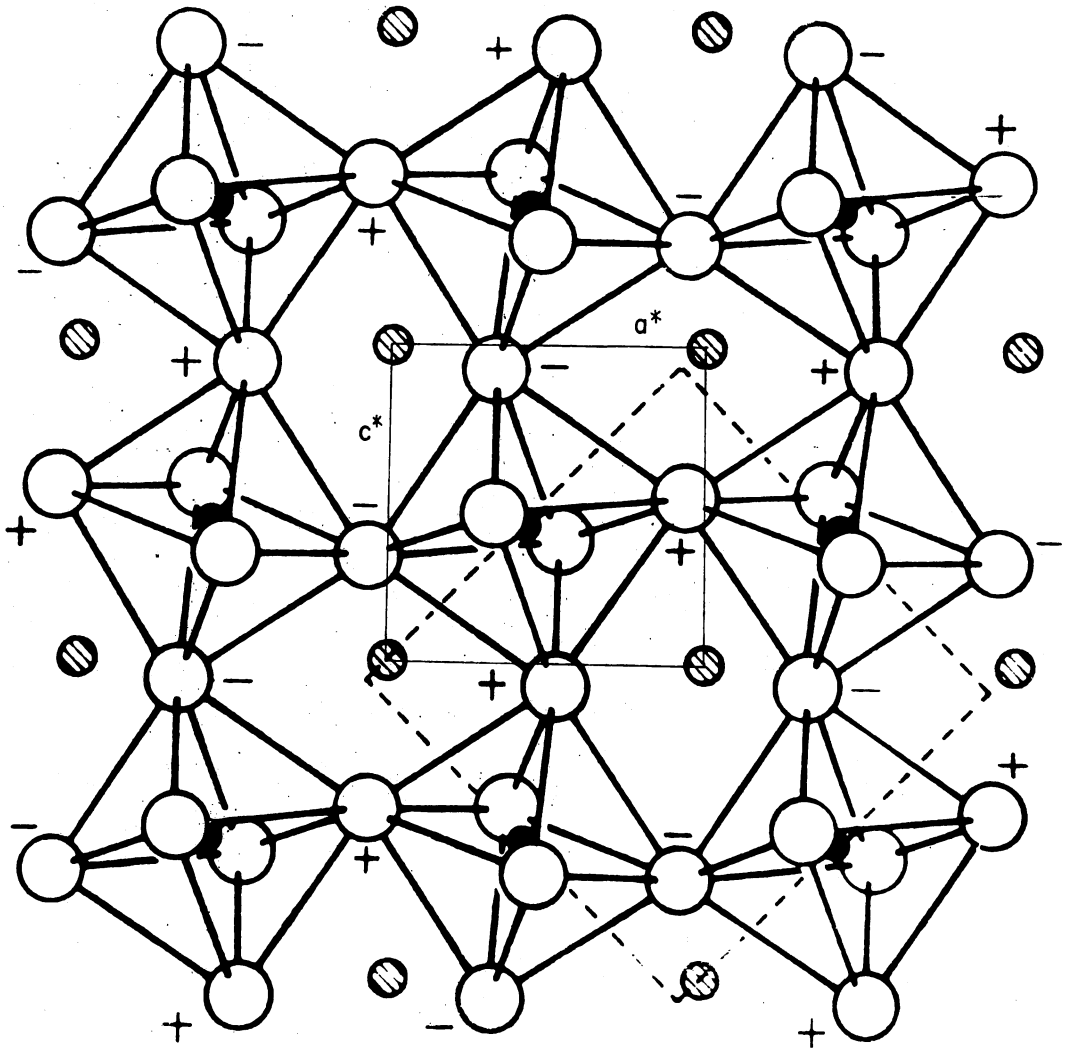

Figure 4. Crystal Structure of $NaMgF_3$

compared to that of K^+ (1.33Å). As a result of the smaller ionic radius, the Na^+ ions fail to fill the cavities between the octahedra. This results in a tilting of the octahedra in order to minimize the volume occupied by the Na^+ ion. The bonding in $NaMgF_3$ is ionic and the MgF_6 octahedra are therefore expected to remain regular at all temperatures (53). The layer of octahedra above and below the plane shown in Figure 4 are mirror images of the layer depicted, thus yielding a rather complex crystal structure. The tilting of the octahedra may be envisioned as occurring in two steps relative to the ideal perovskite structure and are illustrated in Figure 5. There is first a rotation (ω) about a tetrad axis perpendicular to the plane of the Figure (b). An example of a structure exhibiting this kind of tilting is the low temperature (<198 K) tetragonal form of $RbCaF_3$ (55). This is followed by a rotation (ϕ) about a diad axis for $NaMgF_3$ (c). In Figure 4, the orthorhombic unit cell is represented by dashed lines and the pseudocubic subcell is represented by full lines. It can be seen that the pseudocubic cell is determined roughly by the eight Na^+ ions surrounding each octahedron. The relationship between the dimensions of the unit cell and the pseudocubic cell may be represented in matrix form as:

$$\begin{bmatrix} a^* \\ b^* \\ c^* \end{bmatrix} = \begin{bmatrix} \frac{1}{\sqrt{2}} & 0 & 0 \\ 0 & \frac{1}{2} & 0 \\ 0 & 0 & \frac{1}{\sqrt{2}} \end{bmatrix} \begin{bmatrix} a \\ b \\ c \end{bmatrix} \qquad (6)$$

Thus, at room temperature $a^* = 3.792$Å, $b^* = 3.838$Å, and $c^* = 3.891$Å. The variation in the dimensions of the pseudocubic cell as a function of

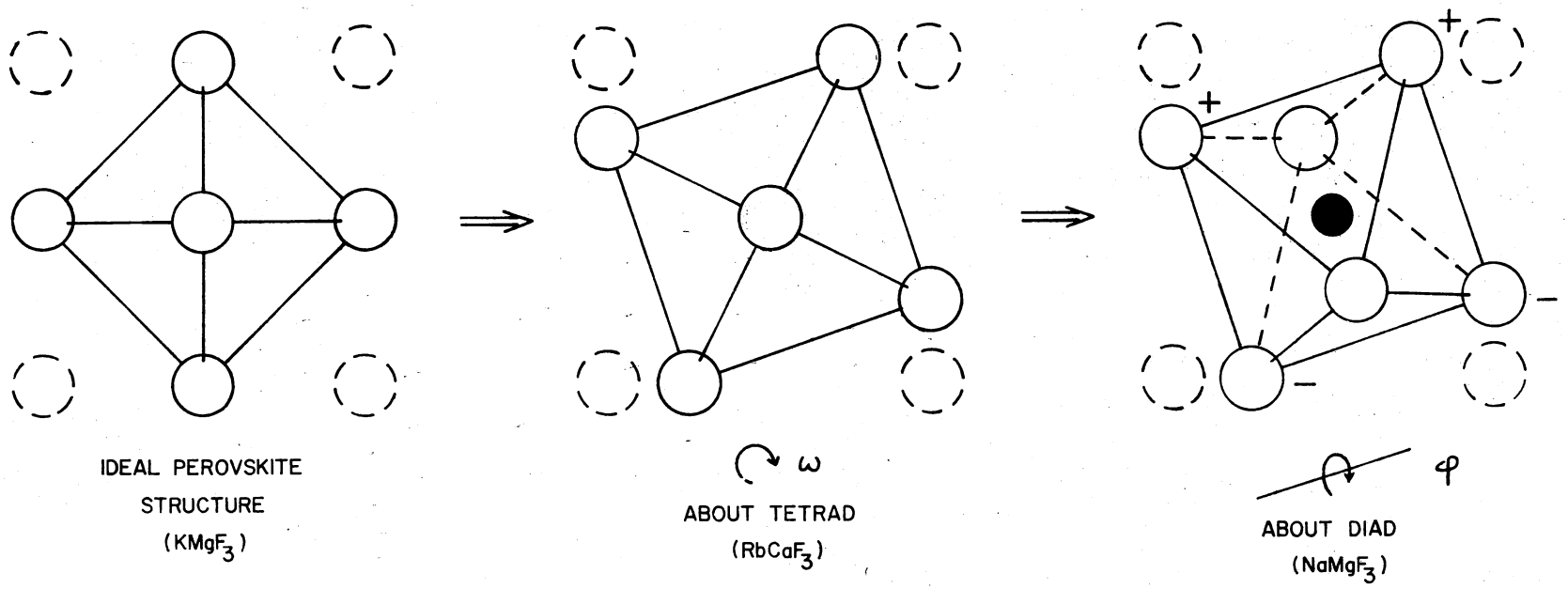

Figure 5. The Tilting of Octahedra in $NaMgF_3$ Compared to the Ideal Perovskite Structure

temperature is shown in Figure 6 (after Chao, et al. (53)). No determination of the crystal structure below room temperature has been made, but thermal conductivity data obtained below room temperature gave no evidence for any phase changes (56). The tilt angles of the octahedra may be related to the lattice parameters through the equations:

$$\omega = \cos^{-1}\left(\frac{\sqrt{2}a}{b}\right) \tag{7}$$

$$\phi = \cos^{-1}\left(\frac{a}{c}\right) \tag{8}$$

or in terms of the pseudocubic dimensions:

$$\omega = \cos^{-1}\left(\frac{a^*}{b^*}\right) \tag{9}$$

$$\phi = \cos^{-1}\left(\frac{a^*}{c^*}\right) \tag{10}$$

The predicted tilt angles at room temperature assuming that the octahedra remain regular are $\omega = 8.88^{\circ}$ (about the tetrad axis) and $\phi = 12.95^{\circ}$ (about the diad axis).

As a starting point for the study of V_K centers in this material, one should make use of the knowledge that has already been obtained for V_K centers in $KMgF_3$ which is also characterized by MgF_6 octahedra, but possesses no tilting. In $KMgF_3$, the self-trapped holes form along <110> directions (20), and there is a bent bond which arises primarily from the repulsion of the effective positive charge of the hole by the Mg^{2+}. The structure of this center is shown in Figure 7. It was then reasonable to expect that a similar bent bond would also be present in the V_K centers found in $NaMgF_3$. A new type of V_K center which results

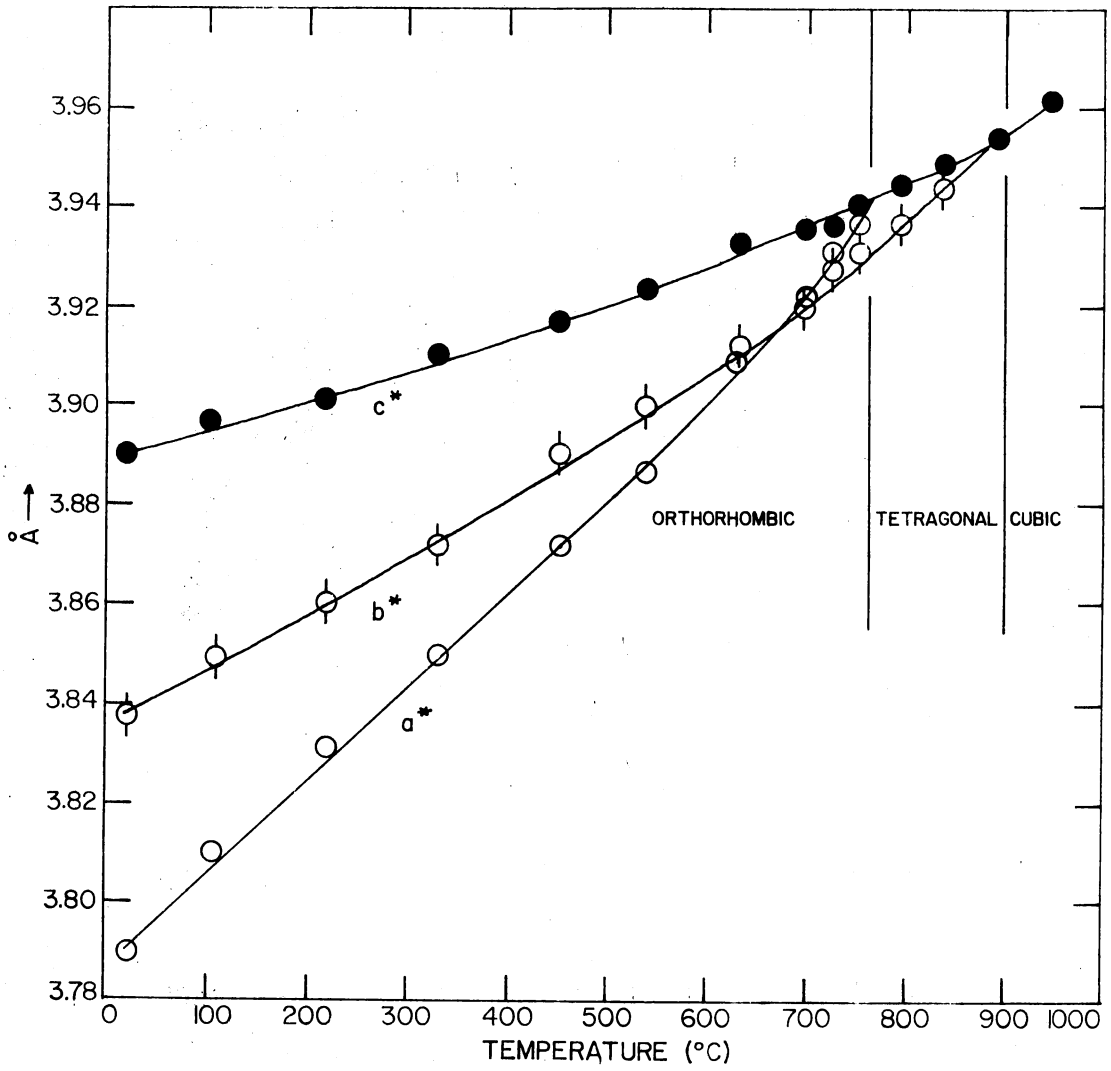

Figure 6. Variation in the Dimensions of the Pseudocubic Cell in $NaMgF_3$ as a Function of Temperature

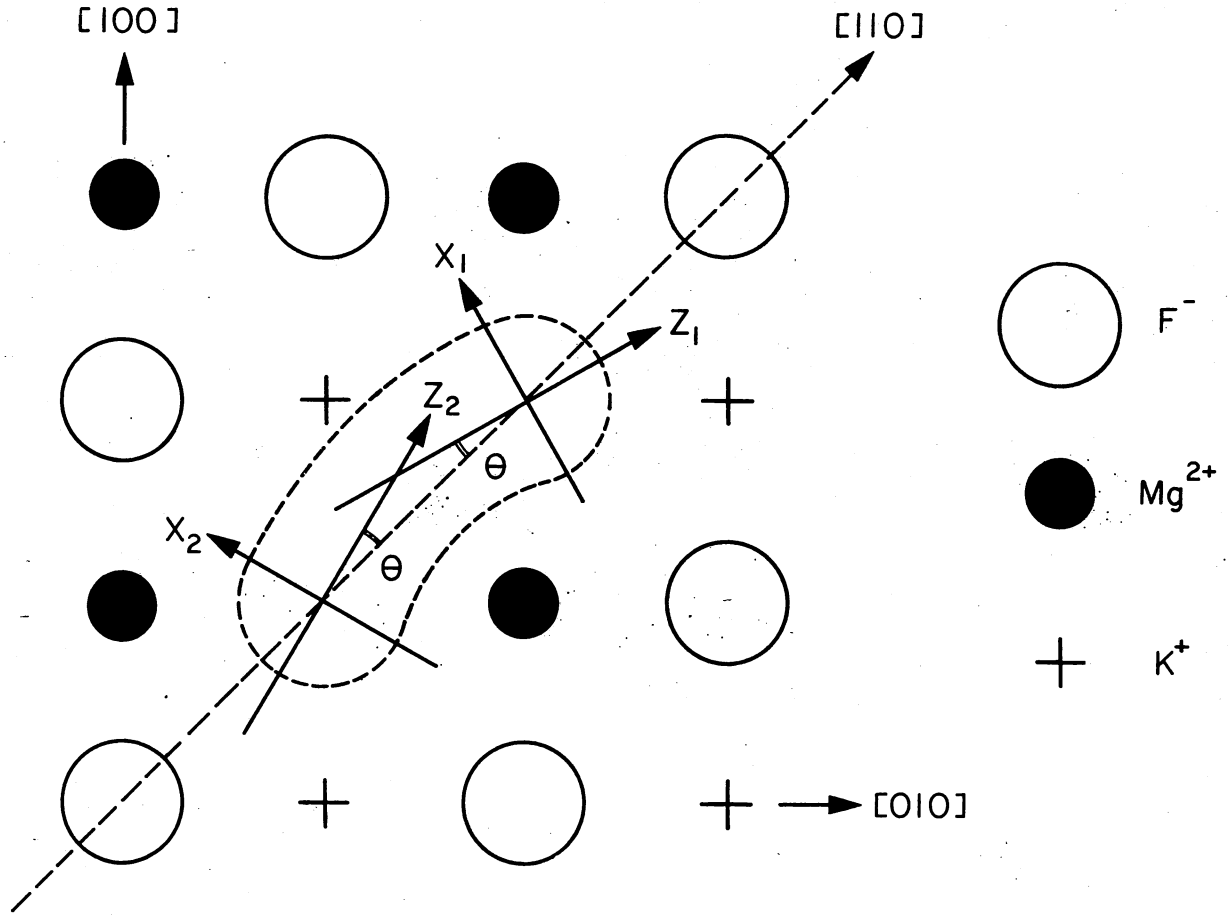

Figure 7. The Structure of the Self-Trapped Hole in $KMgF_3$

from the peculiar tilting of the octahedra in $NaMgF_3$ and which possesses ~ [100]-type symmetry was also analyzed. An additional result obtained from the analysis of the V_K center ESR spectra involved a determination of the tilt angles of the octahedra at low temperature (77 K).

A complete analysis of the intrinsic self-trapped holes in $NaMgF_3$ will be presented. The production and thermal decay characteristics will be correlated with complementary thermoluminescence measurements.

CHAPTER II

EXPERIMENTAL PROCEDURE

A. Crystals

Investigations of radiation damage in $KMgF_3$:Mn were carried out primarily on single crystals obtained from Oak Ridge National Laboratory. They were grown by the Stockbarger technique and were doped with approximately 400 ppm manganese. Additional crystals were grown in the Oklahoma State University Crystal Growth Laboratory by means of a modified Bridgman-Stockbarger technique and contained approximately 8000 ppm manganese. All samples were found to cleave along <100> planes.

Crystals of $NaMgF_3$ used in this study were also grown at Oklahoma State University by the Bridgman-Stockbarger technique. No impurity analysis was made, but ESR data taken at high gain for virgin crystals revealed the presence of Mn^{2+} as a trace impurity. Typical crystals possessed a characteristic twinning which complicated the analysis of ESR data. Such twinning is common for compounds with tetragonal or orthorhombic crystal structures. For example, several types of twinning have been observed in isomorphous $CaTiO_3$ (57). Only one type of twinning was discernable in $NaMgF_3$ based on the analysis of V_K center ESR data. This domain structure was believed to be similar to that found in orthorhombic $SmAlO_3$ (58). For this type of twinning the pseudocubic c* axis would be coincident in every domain whereas the a* and b* axes

alternatively interchange from one domain to the next. This proposed domain structure is consistent with that evident in the ESR data and will be discussed further in the experimental results. When samples were annealed, it was found that quenching to room temperature too rapidly resulted in cleavage into several fragments. One such crystallite was found to be essentially single, i.e., no discernable twinning was present from an initial observation of the ESR data. This sample was thus used for the detailed analysis of the ESR spectra. Samples could be cleaved parallel to any of the three pseudocubic faces.

For ESR measurements, the crystal dimensions were generally limited by the diameter of the inner quartz tubing of the finger dewar (Section C). Various sample sizes were used, but volumes were typically 50-100 mm^3. Samples of comparable size were used for thermoluminescence measurements.

B. Irradiation Procedure

Samples were irradiated primarily with 1.5 MeV electrons from a Van de Graaff accelerator at beam currents ranging from 5 to 15 μA. Typical irradiation times ranged from 10 to 30 minutes. For irradiations at room temperature samples were wrapped in aluminum foil and mounted on the face of an aluminum block which acted as a heat sink. The combination was then placed approximately 2 inches from the end of the accelerator tube. For irradiations at 77 K, samples were placed in an eight-ounce styrofoam cup filled with liquid nitrogen. The cup was positioned approximately 1 foot from the end of the accelerator tube, and an aluminum shield ~1 mm thick was placed in front of the cup in order to protect the accelerator tube window from any hazards which

might be introduced through the build-up of ozone in the liquid nitrogen. Such dangers were also reduced by limiting the irradiation time to 5 minutes per cup of liquid nitrogen. When smaller dose rates were desired, a ^{60}Co γ cell (~ 10^5 R/hr) was used. Bleaching with ultraviolet light was accomplished through the use of a 100 watt Hanovia low pressure Hg lamp.

C. ESR Measurements

Two methods were employed for mounting the samples in preparation for the ESR measurements. For all of the work done on $KMgF_3$:Mn, samples were mounted by a cleavage plane onto the end of a copper rod .125 inches long using silicon high vacuum grease. The rod-sample combination was then screwed into a 3/16" x 7" stainless steel rod and lowered into a 5 mm I.D. finger dewar filled with liquid nitrogen (see Figure 8). Using this method, samples had to be mounted prior to irradiation at 77 K. Although irradiation of the grease at 77 K was found to produce radicals which gave rise to ESR lines near g = 2, this did not hamper the investigations of $KMgF_3$:Mn since the cubic Mn^{2+} signals always present in the samples were in this same region of the spectrum.

The work done on $NaMgF_3$ did require an alternative method of mounting since ESR lines necessary in the analysis of the V_K center spectra were obscured by the spurious grease lines. This was accomplished by replacing the copper rod arrangement with stainless steel tubing equipped with an adjustable spring insert (see Figure 9). Samples could then be spring-loaded to a desired tension, thus by-passing the need for an adhesive agent. Using this technique, irradiations could be performed directly with unmounted crystals.

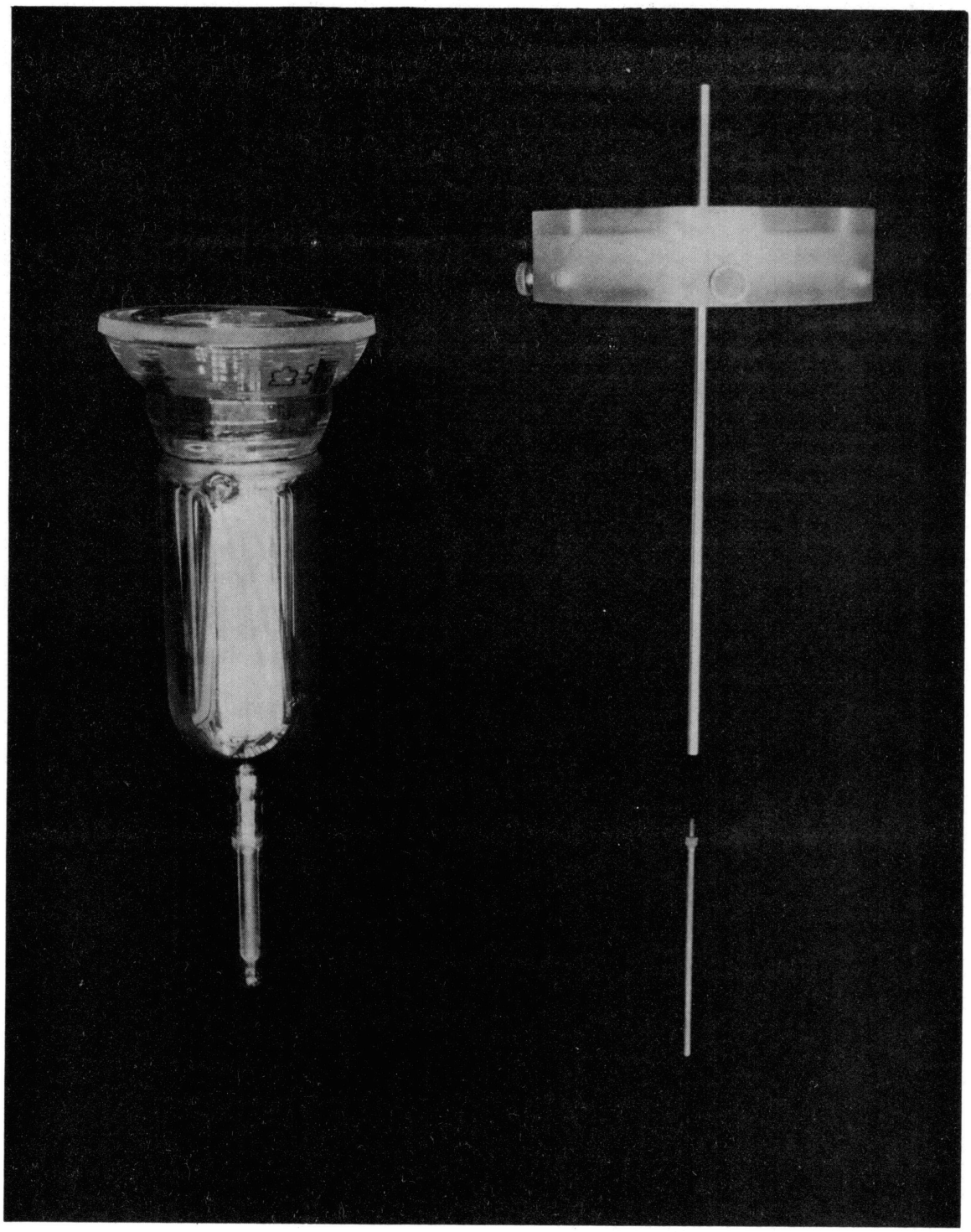

Figure 8. Liquid Nitrogen Finger Dewar Used in Conjunction With the Varian V-4531 Rectangular ESR Cavity

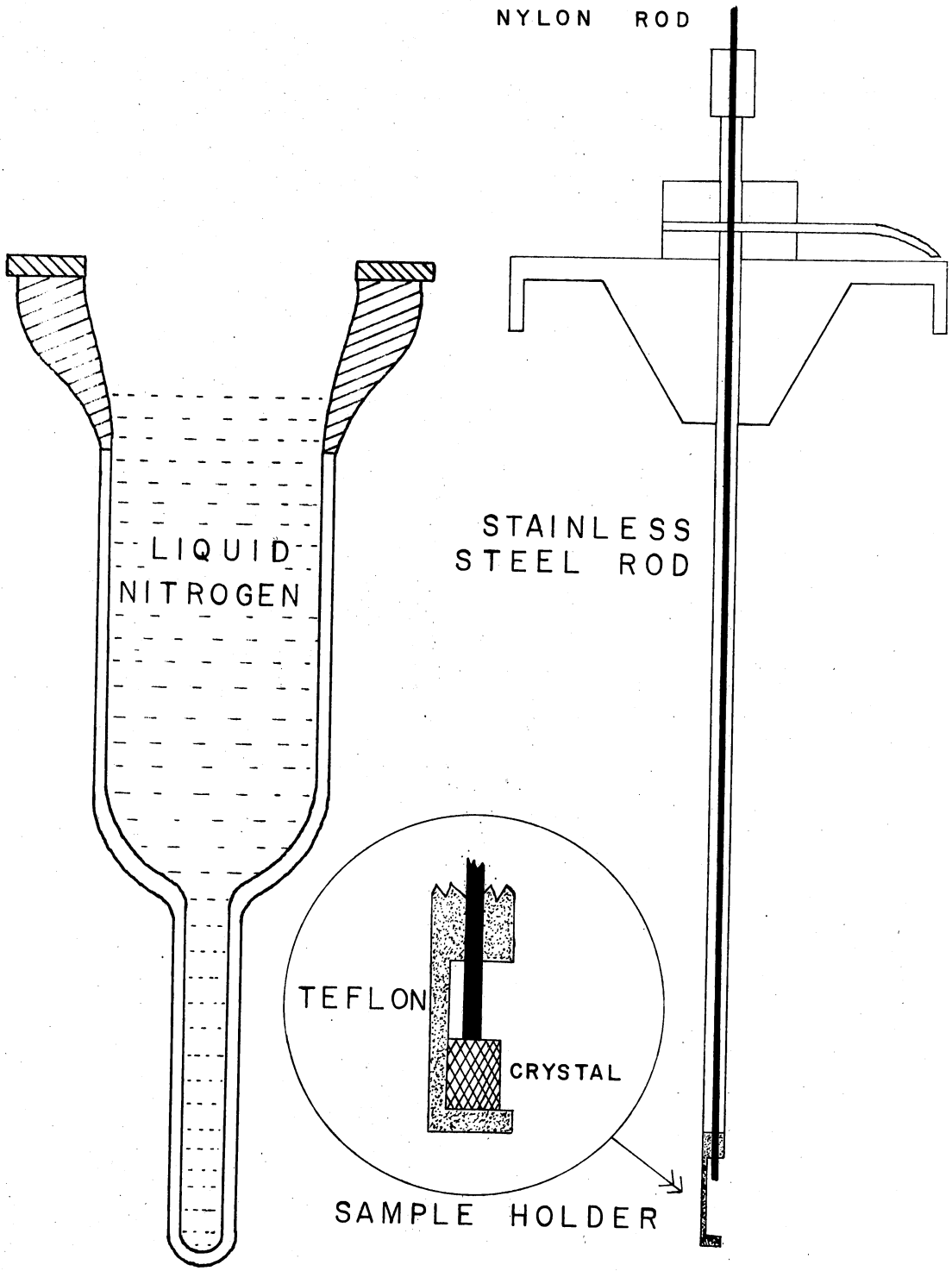

Figure 9. Holder Used in ESR Measurements of V_K Centers in $NaMgF_3$

Following this initial procedure, the finger dewar was placed in a Varian V-4531 rectangular cavity, and an ESR measurement was subsequently performed. All ESR measurements were made at 77 K. The ESR spectrometer was of the X-band homodyne variety and utilized 100 KHz field modulation. The static magnetic field was supplied by a Varian six-inch magnet. For pulse anneal studies, a Varian Variable Temperature Accessory was used in conjunction with the Varian V-4531 cavity. A more detailed description of both the spectrometer and variable temperature system may be found in reference 59.

The measurement of magnetic fields was accomplished through the use of an NMR (proton) probe. Several probes were constructed which were used in conjunction with a marginal oscillator (59). The source of protons for these probes was pure white glycerin, $C_3H_8O_3$. Using different probes, measurements of magnetic field from ~1780 gauss to ~7210 gauss could be achieved. In order to convert from the measured NMR resonance frequency to magnetic field the following relationship was used (60).

$$H(\text{gauss}) = 234.87\nu \text{ (MHZ)} \qquad (11)$$

Corrections had to be made for the fact that the sample position and probe position were not coincident. This correction was assumed to vary linearly with the magnetic field. Additional corrections were made to account for possible shifts in the microwave frequency occurring during the course of the field measurements.

D. Thermoluminescence Measurements

All TSL measurements were performed in the dewar shown in Figure

10. This dewar was designed for measurements following electron irradiation near liquid nitrogen temperature. Samples were mounted by means of a brass clamp onto a cold finger positioned within a stainless steel hull fitted with brass bellows and two windows. One window was made of aluminum and was positioned in front of the sample during electron irradiation. The other window was made of sapphire and was positioned in front of the sample during TSL measurements or during bleaching. The windows could be mechanically interchanged at any temperature $\geq$ 77 K by means of the bellows mechanism. All irradiations and TSL measurements were performed using a roughing pump vacuum to insure against condensation on the sapphire window. Luminescence was detected by means of a RCA 1P28 photomultiplier tube. Sample temperatures were measured by means of a copper-constantan thermocouple wedged between the sample and brass clamp. The TSL data was recorded by means of a Mosely 135 XY Recorder where the Y axis indicated the photomultiplier tube current (luminescence intensity) and the X axis gave the sample thermocouple voltage (temperature).

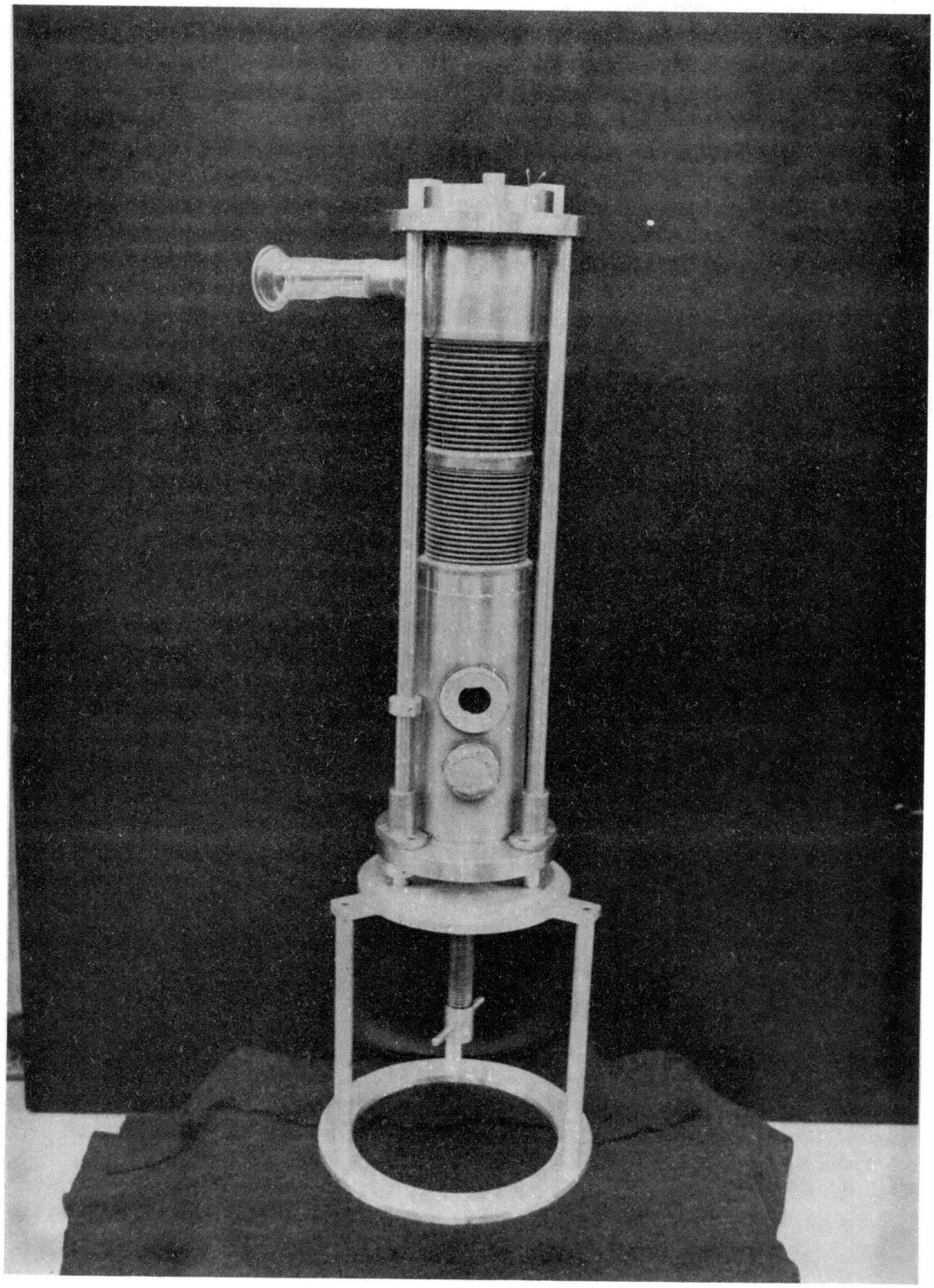

Figure 10. Dewar Used for Thermoluminescence Measurements

CHAPTER III

EXPERIMENTAL RESULTS

In this chapter the results of ESR and TSL measurements will be presented. The findings for $KMgF_3$:Mn and $NaMgF_3$ will be treated in two separate sections with the first section centering on experiments related to the Mn^{2+}-fluorine vacancy center. The second section will be devoted primarily to the ESR results obtained for the intrinsic self-trapped holes in $NaMgF_3$ and will also include a presentation of complementary TSL measurements. The detailed analysis of this data will be given in the following chapter.

A. The Mn^{2+}-Fluorine Vacancy Center

Prior to electron or γ irradiation, ESR measurements taken for single crystals of $KMgF_3$:Mn (400 ppm) yielded an intense and highly resolved spectrum which was recognized as arising from Mn^{2+} at sites of octahedral symmetry. This spectrum has been analyzed in detail by Ogawa and Yokozawa (61) and is shown in Figure 11. The complexity of the spectrum arises for several reasons. The octahedral crystal field splits the six-fold degeneracy of the $^6S_{5/2}$ ground state of the Mn^{2+} ion into a quartet and a doublet. The origin of this zero field splitting is not completely understood at present, but a comprehensive review of the theory is given in reference (62). The Zeeman splitting will then lift the remaining degeneracy of the energy levels correspond-

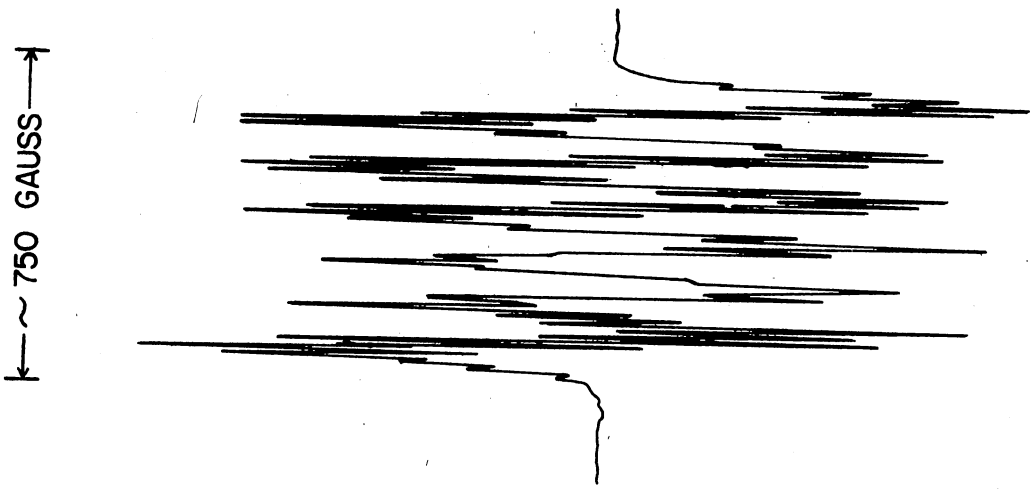

Figure 11. Cubic Mn^{2+} ESR Spectrum

ing to the magnetic substates defined by m_S = - 5/2, - 3/2, - 1/2, 1/2, 3/2, and 5/2. There is a further hyperfine splitting of these energy levels arising from interaction of the unpaired electrons with the ^{55}Mn nucleus. The corresponding nuclear spin I is 5/2, and therefore the associated magnetic substates are given by m_I = - 5/2, - 3/2, - 1/2, 1/2, 3/2, and 5/2. Finally, there is a superhyperfine splitting originating from interactions between the unpaired electrons and the six equivalent surrounding ^{19}F nuclei (I = 1/2). The ESR selection rules for the transitions between energy levels are $\Delta m_S = \pm 1$ and $\Delta m_I = 0$, and there are a total of 210 lines in the spectrum (including superhyperfine structure). For the case of octahedral symmetry, the hyperfine splitting is approximately one order of magnitude greater than the crystal field splitting. Thus considerable overlapping of lines occurs in the spectrum which consequently takes on the appearance of a six-line hyperfine group.

When crystals were electron irradiated at room temperature up to 30 minutes at 10 μA no new spectra were observed to grow in, and no discernable change in the cubic Mn^{2+} spectrum was detected. However, if following the room temperature irradiation the sample was exposed to an unfiltered mercury lamp at 77 K, then a new spectrum was generated. A typical spectrum obtained for an orientation of the static magnetic field parallel to a [100] direction is shown in Figure 12. Both the maximum splitting of the lines and the best resolution of the superhyperfine structure occurs for this orientation of the magnetic field. This spectrum was generated after a room temperature electron irradiation of 30 minutes at 10 μA followed by a 77 K uv bleach for 2 hours. The spectrum was characterized by division into six-line hyperfine groups and

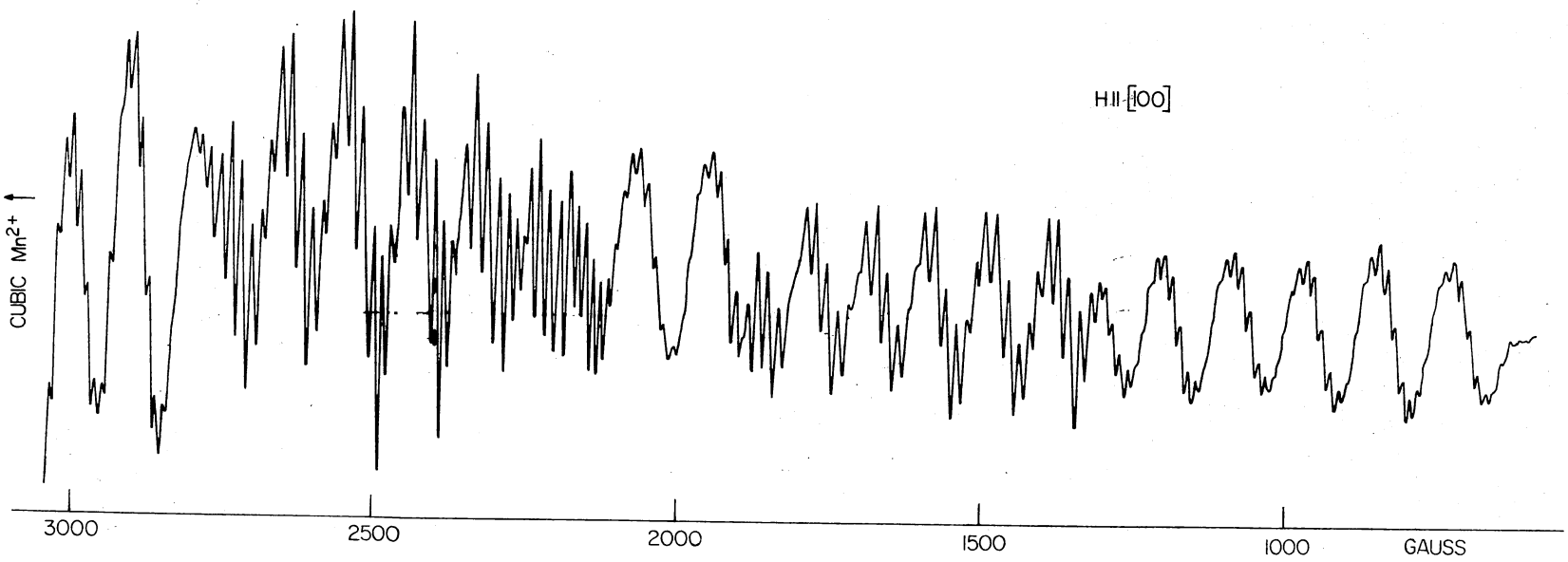

Figure 12. (a) Mn^{2+}-Fluorine Vacancy ESR Spectrum (Low Field)

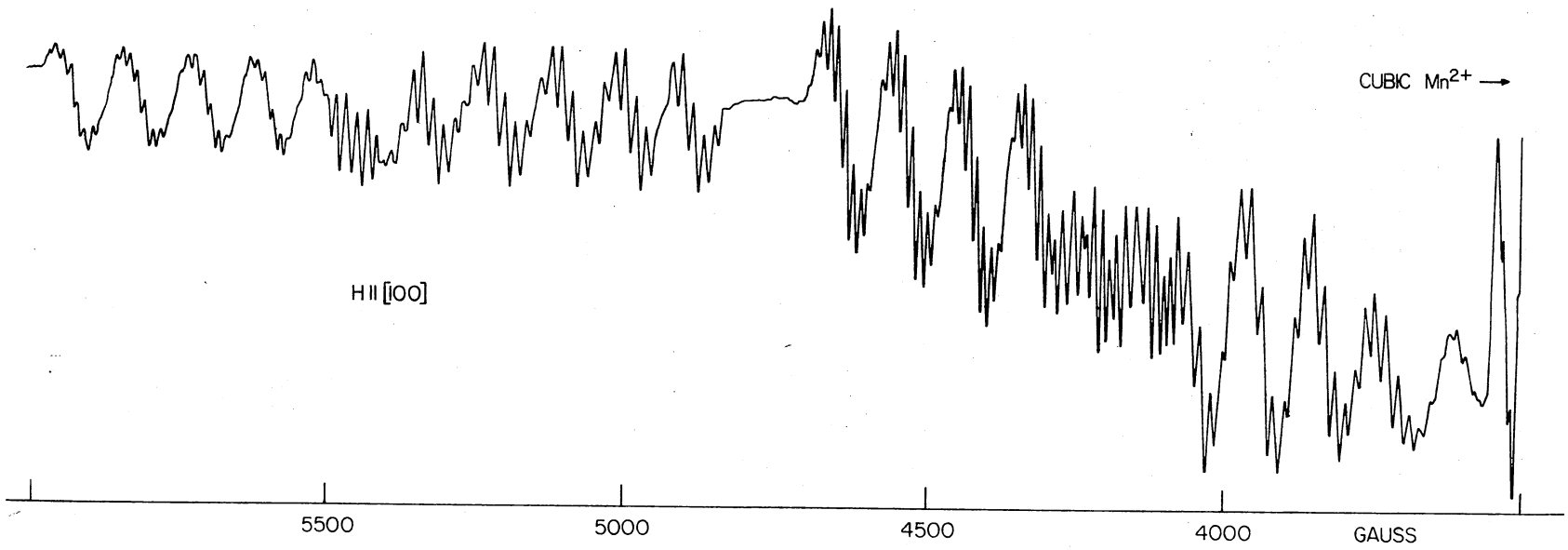

Figure 12. (b) Mn^{2+}-Fluorine Vacancy ESR Spectrum (High Field)

was thus attributed to Mn^{2+}. The range of the spectrum was found to extend roughly from less than 1000 gauss to nearly 6000 gauss which was indicative of a large crystal field splitting. This also indicated that the Mn^{2+} was at a site departing significantly from octahedral symmetry. The analysis of this spectrum, to be discussed in the next chapter, resulted in a model in which the initial room temperature irradiation creates an F center adjacent to a Mn^{2+} ion, and the subsequent uv excitation at 77 K removes the F electron leaving a Mn^{2+}-fluorine vacancy center. A further consequence of the analysis was that the crystal field did not possess perfect [100] axial symmetry, but was determined to have a rhombic contribution. As a result, the spectrum was broken up into three distinct groups of lines. One group (I) arises for orientations of the magnetic field parallel to the defect axis defined by the Mn^{2+}-fluorine vacancy. The other two groups (II and III) arise from orientations of the magnetic field perpendicular to the defect axis. A stick diagram of the complete spectrum constructed after the computer analysis of the data is shown in Figure 13. Due to complications introduced by the overlapping of lines from different groups and the presence of the cubic Mn^{2+} spectrum, not all of the line positions in the [100] spectrum were measured. Furthermore, lines occurring at field positions of less than ~ 1780 gauss were outside the range of the proton probe. Thus values of magnetic field for 22 line positions were measured and are indicated in the stick diagram. The corrected experimental field values together with those calculated in the analysis are shown in Table I. The microwave frequency during the course of these measurements was 9.242362 GHz. No magnetic field measurements were taken for any orientations of the magnetic field other than <100>.

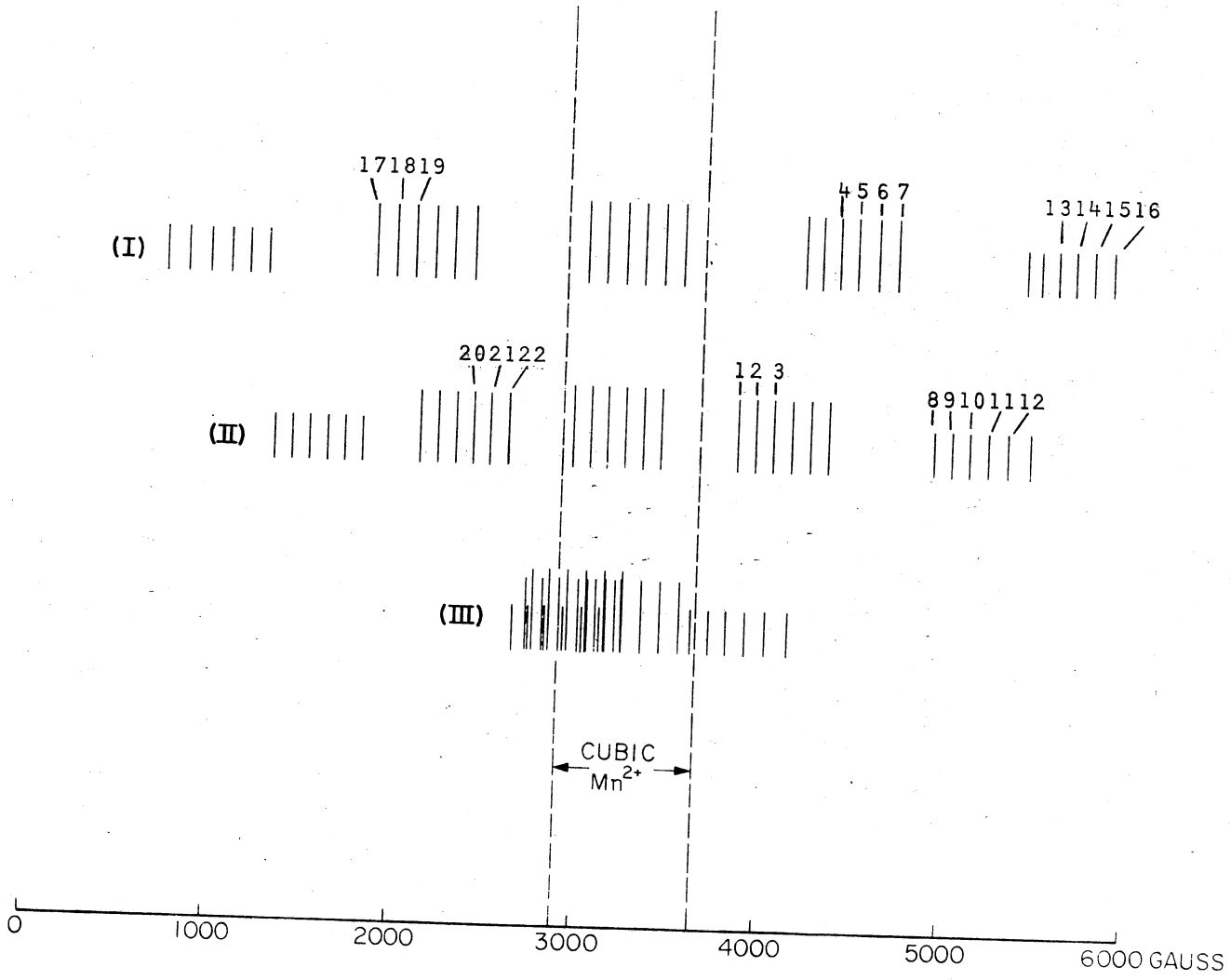

Figure 13. Stick Diagram for the Mn^{2+}-Fluorine Vacancy ESR Spectrum

TABLE I

CORRECTED FIELD POSITIONS (IN GAUSS) OF RESONANT LINES OF THE Mn^{2+}-FLUORINE VACANCY CENTER ESR SPECTRUM

Group I

Line	Experimental	Calculated
4	4395.18	4392.72
5	4495.40	4493.06
6	4598.11	4597.85
7	4703.17	4703.91
13	5585.55	5583.93
14	5680.71	5678.34
15	5782.47	5780.01
16	5888.71	5887.38
17	1864.03	1861.37
18	1972.47	1971.66
19	2079.56	2079.94

Group II

Line	Experimental	Calculated
1	3855.09	3853.90
2	3951.40	3952.13
3	4048.39	4049.47
8	4935.09	4930.49
9	5024.57	5022.81
10	5120.81	5120.88
11	5223.90	5225.81
12	5334.91	5336.47
20	2418.31	2416.17
21	2510.05	2510.60
22	2603.20	2605.17

This was due to the fact that both broadening and increased overlapping of the lines made it difficult to make absolute assignments for the transitions.

The superhyperfine structure, which arises through an interaction of the unpaired electrons with the five nearest neighbor fluorine nuclei, is only partially resolved. However the resolution is sufficient to distinguish group I resonances from group II since the superhyperfine structure on each hyperfine line differs for different orientations of the Mn^{2+}-fluorine vacancy center relative to the applied magnetic field. The two lowest field sets of hyperfine lines are shown in Figure 14.

Data was also obtained for the more heavily doped $KMgF_3$:Mn crystals (8000 ppm). However, no resolved superhyperfine structure could be observed in the ESR spectra generated using these crystals.

Band pass filters were used in order to determine the approximate wavelength of light necessary to produce the ESR spectrum. It was found that the spectrum could be easily produced using filters with transmissions centered at 2536Å and 3130Å, but using a 4000Å filter with comparable bleaching time the intensity of the spectrum was reduced by more than a factor of three. Thus an upper limit on the wavelength of light necessary for efficient production of the spectrum would lie in the range 3500-4000Å.

The results of a saturation study of the production of the ESR spectrum are shown in Figure 15 for an initial electron irradiation of 20 minutes at 10 μA. The temperature of the crystal was maintained at 77 K throughout the course of this saturation study. The data indicates that the Mn^{2+}-fluorine vacancies initially grow in very rapidly, then taper off to nearly a linear growth until saturation is achieved.

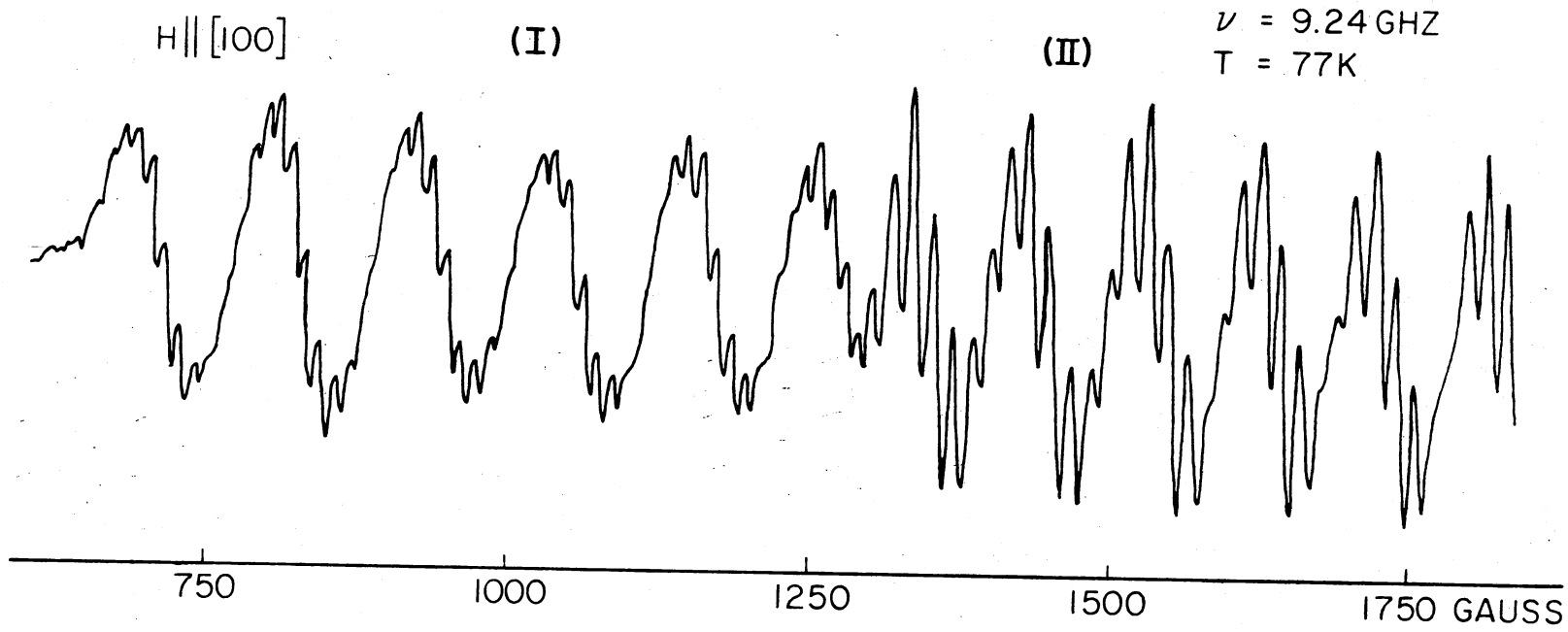

Figure 14. The Two Lowest Field Sets of Hyperfine Lines for the Mn^{2+}-Fluorine Vacancy [100] ESR Spectrum Illustrating the Difference in the Superhyperfine Patterns for Groups I and II

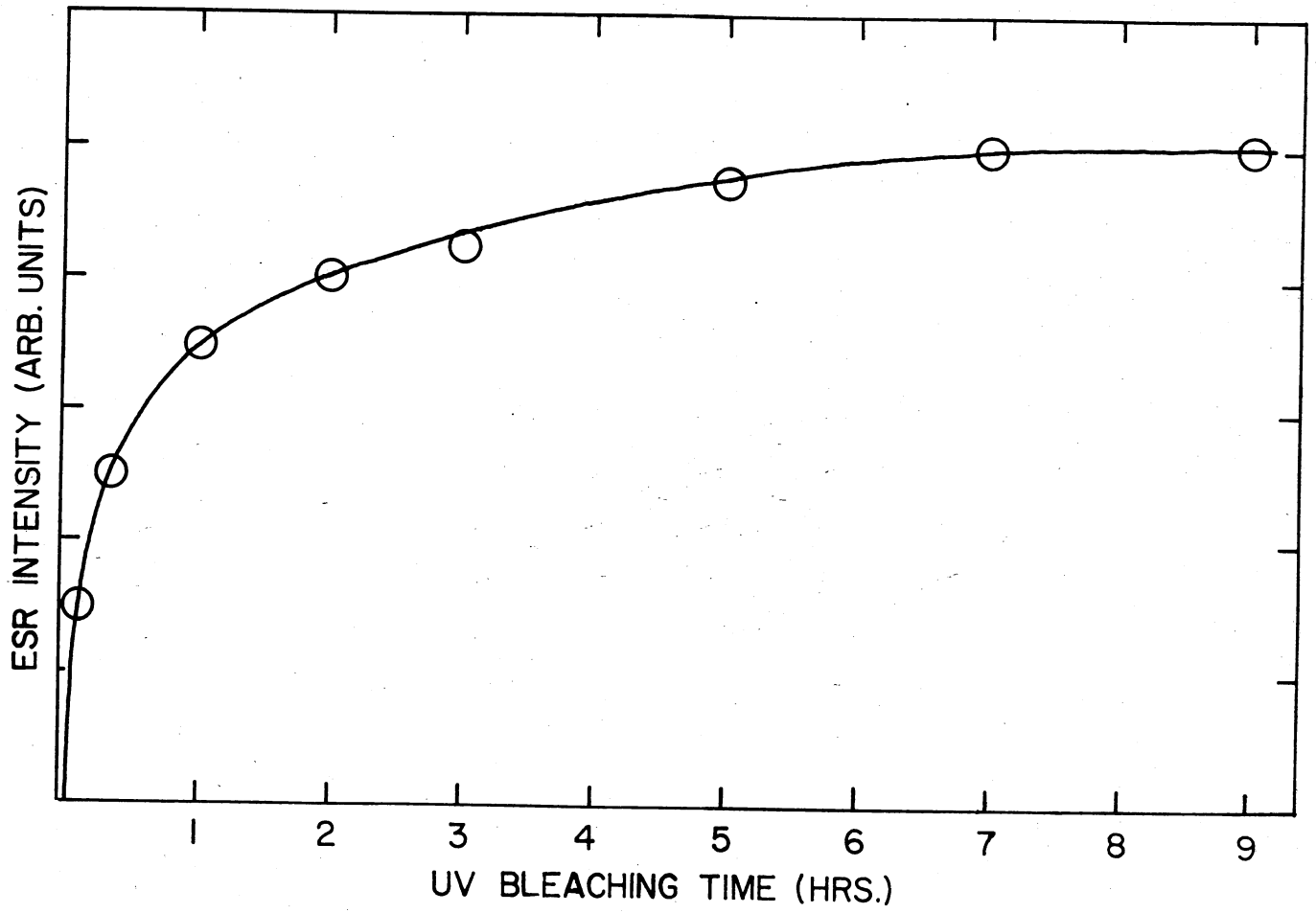

Figure 15. Saturation Study of the Mn^{2+} Fluorine Vacancy Center

Mn^{2+}-fluorine vacancy centers could also be generated by room temperature ^{60}Co γ irradiation (plus 77 K uv excitation), but this required irradiation times of ~ one day in order to produce enough Mn^{2+}-F center pairs to be observable.

Direct electron irradiation of virgin or annealed crystals at 77 K could also produce Mn^{2+}-fluorine vacancy centers. This procedure was not as effective in producing the centers compared to the previously described procedure. For example, electron irradiation for 45 minutes at 77 K produced a spectrum ~ 1/4 as intense as that found for an electron irradiation of 30 minutes at room temperature followed by 2 hours of uv bleaching at 77 K. ESR signals arising from intrinsic V_K centers were also observable in the spectrum obtained for direct electron irradiation at 77 K. However, when crystals were warmed through the first TSL glow peak (115 K) which corresponds to the thermal decay of the V_K centers, the intensity of the Mn^{2+}-fluorine vacancy spectrum remained unchanged.

The results of a pulse anneal study of the Mn^{2+}-fluorine vacancy spectrum are shown in Figure 16. This data was obtained by three minute pulse anneals at progressively higher temperatures. The monitoring temperature (i.e., the temperature of the nitrogen gas used in conjunction with the Varian Variable Temperature Accessory) was ~ 96 K. This study indicates that the thermal decay of the Mn^{2+}-fluorine vacancy center occurs at ~ 185 K.

After annealing to room temperature, the Mn^{2+}-fluorine vacancy centers can be regenerated by an additional uv bleach at 77 K. This regeneration effect is shown in Figure 17. In Figure 17(a), the sample was bleached for one hour at 77 K following the initial room temperature

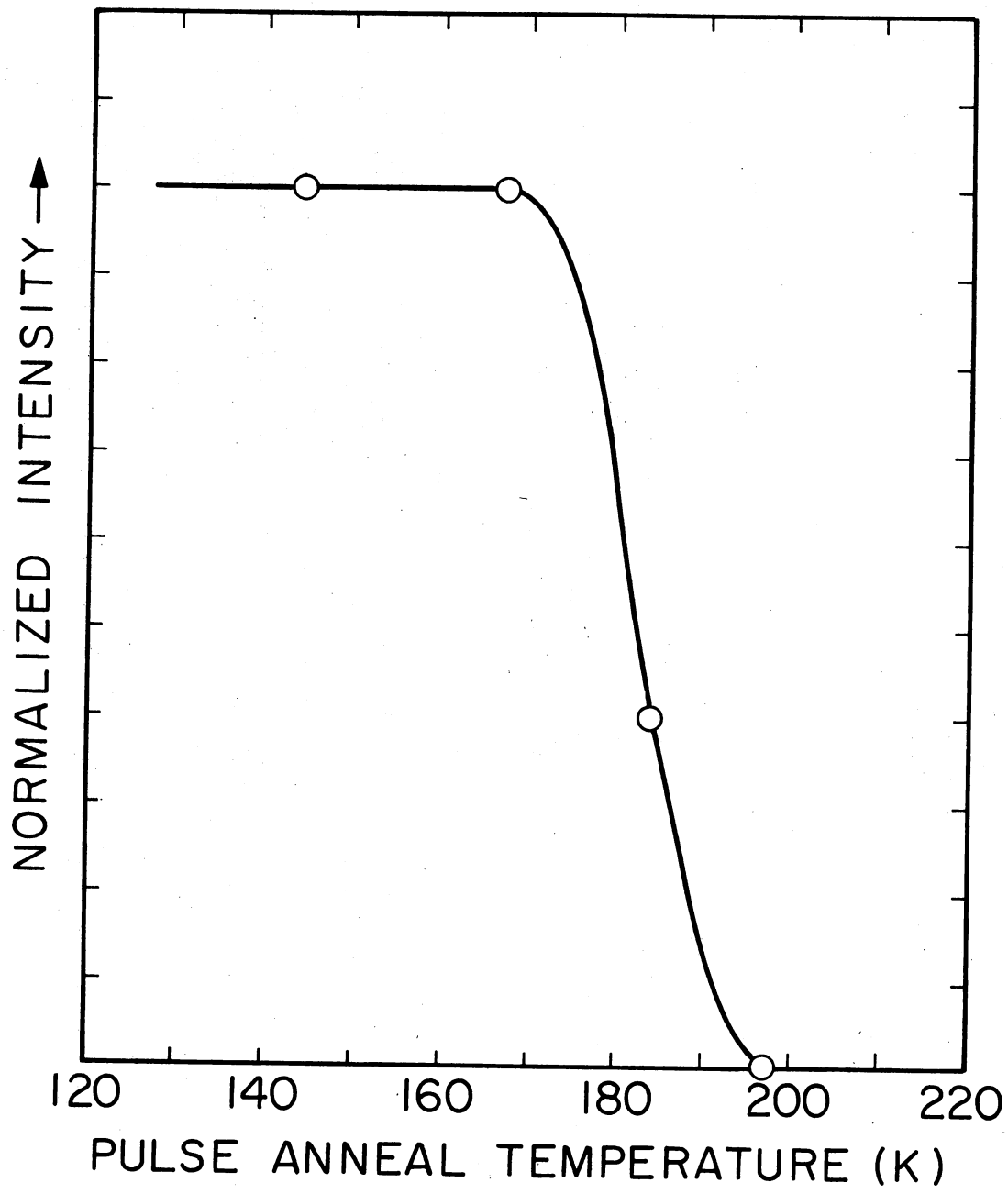

Figure 16. Pulse Anneal Study of the Mn^{2+} Fluorine Vacancy Center

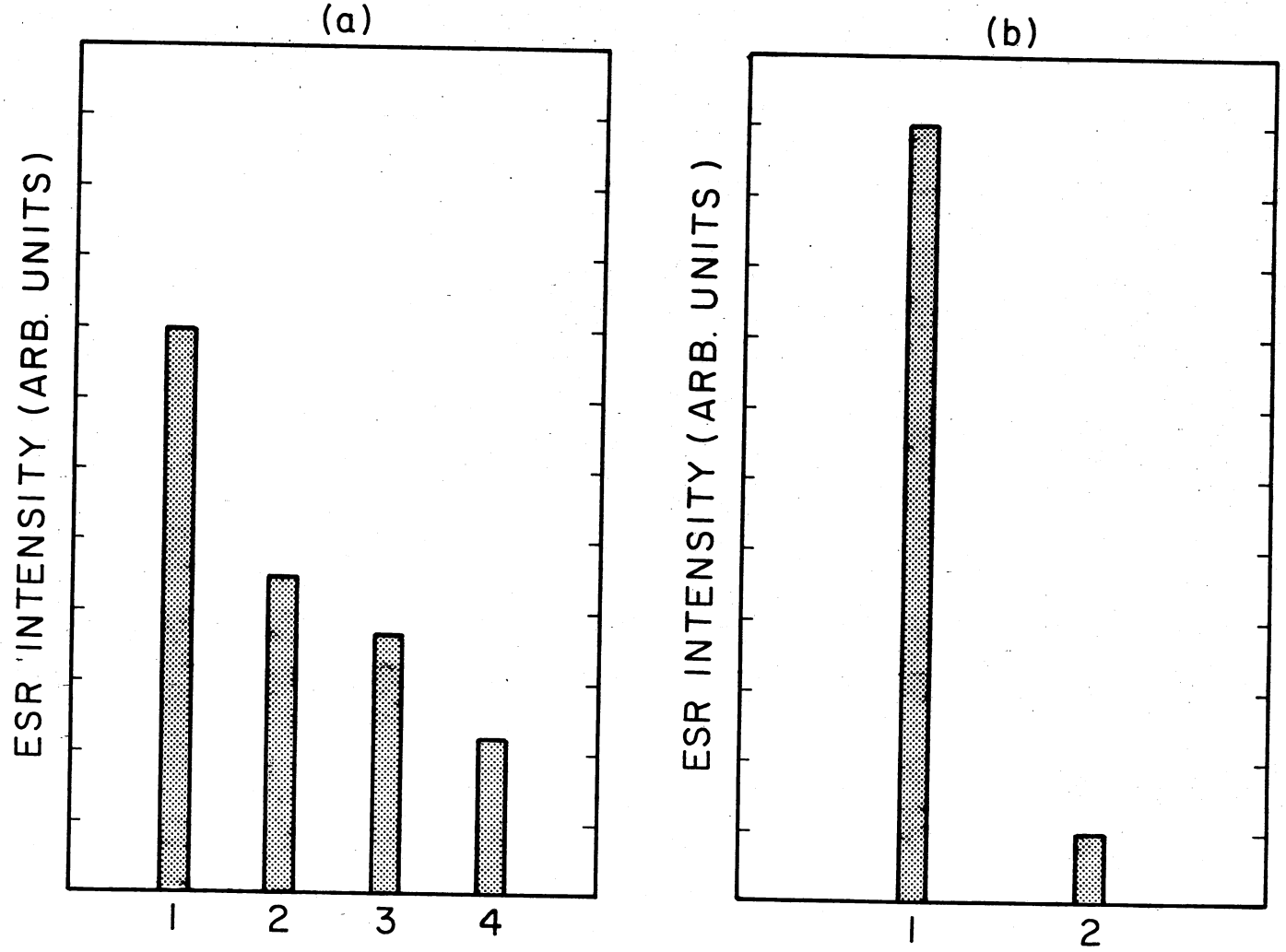

Figure 17. Regeneration of the Mn^{2+}-Fluorine Vacancy Center ESR Spectrum

electron irradiation after which the ESR intensity was measured (column 1). Columns 2, 3, and 4 represent the ESR intensity obtained by consecutively warming the sample to room temperature and rebleaching for one hour at 77 K without additional room temperature irradiation. In Figure 17(b), the sample was treated the same as in Figure 17(a) except the initial uv bleach was nine hours. The large relative difference between columns 1 and 2 indicates that the longer initial uv bleach destroyed a much larger percentage of Mn^{2+}-F center pairs in (b) than in (a).

Thermoluminescence (TSL) was generated between 77 K and room temperature using the same irradiation procedure that produced the Mn^{2+}-fluorine vacancy centers. The TSL is obtained only if crystals are electron irradiated prior to uv bleaching, i.e., uv bleaching of annealed or virgin crystals at 77 K will yield no TSL. Typical TSL data is shown in Figure 18 for an initial room temperature electron irradiation of 20 minutes. The solid curve was taken following an initial one hour uv bleach at 77 K. Each of the dashed curves were obtained without additional room temperature irradiation by warming the sample to room temperature and then rebleaching at 77 K in a manner similar to Figure 17(a). Thus the TSL exhibits a regeneration property similar to that found for the Mn^{2+}-fluorine vacancy centers. However, no TSL glow peaks (140 K, 160 K, 205 K, 236 K) coincide with the thermal decay of the Mn^{2+}-fluorine vacancy ESR spectrum. No detailed spectroscopic analysis was performed of the TSL emission, but visual observation of the emission indicated that the light was primarily 590 nm (63), characteristic of cubic Mn^{2+}.

When crystals of $KMgF_3$:Mn (400 ppm) were electron irradiated at

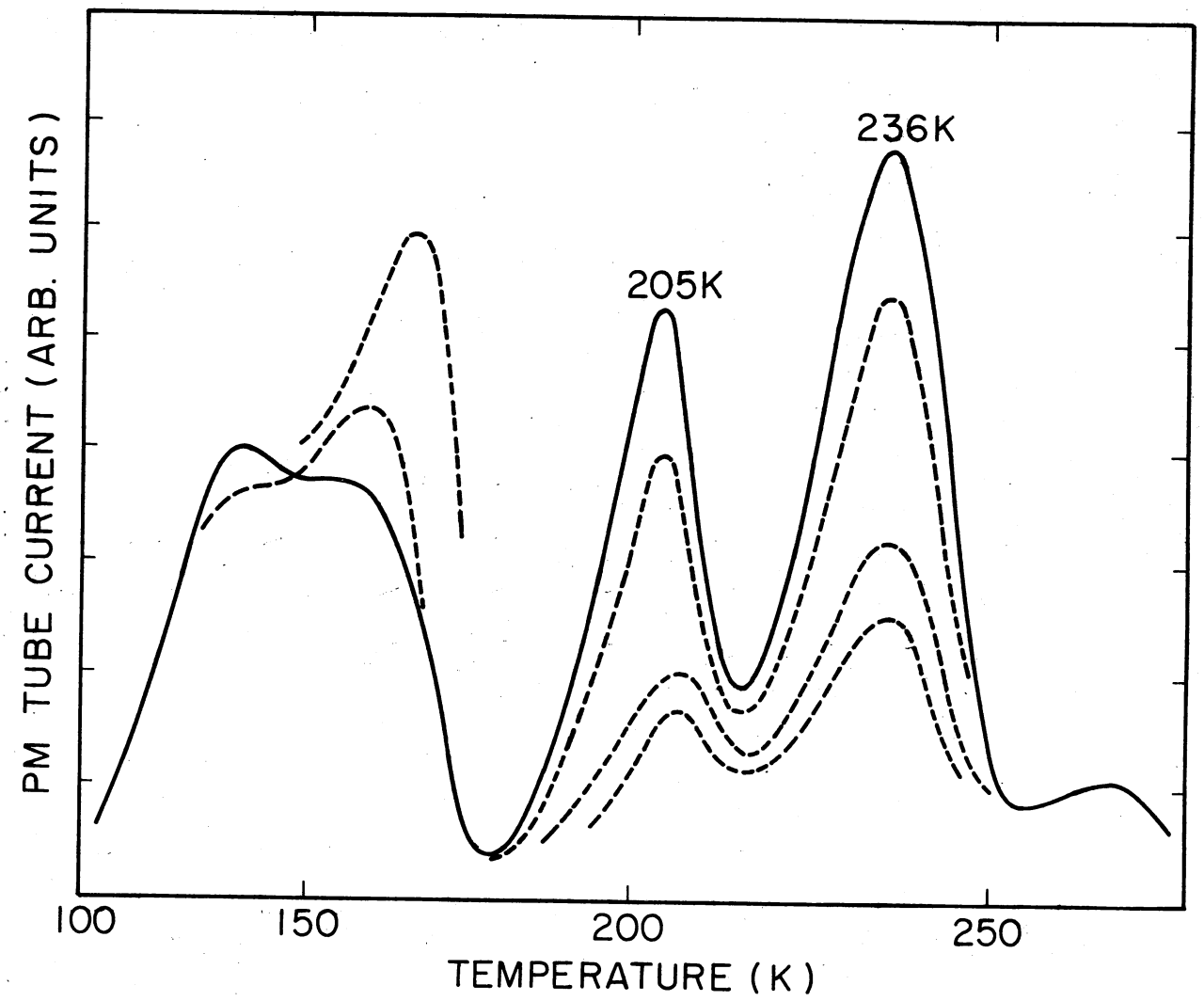

Figure 18. Thermoluminescence of $KMgF_3$:Mn

77 K and then warmed to room temperature, an additional rather weak ESR spectrum remained which was of unknown origin. This data could not be generated solely by electron irradiation at room temperature, and only the low field portion of the spectrum was examined. This spectrum is shown in Figure 19 and possesses well defined hyperfine structure. The spectrum is centered at ~ 850 gauss and shows no significant angular dependence for rotations of the magnetic field as much as $\pm 20^{\circ}$ off <100> directions. There appear to be 10-11 hyperfine lines in the spectrum with an associated splitting of ~ 50 gauss which is approximately half the hyperfine splitting for isolated Mn^{2+}. The spectrum could originate in Mn^{2+} pairs, since this would reduce the hyperfine splitting by approximately 1/2 and increase the number of hyperfine lines from 6 to 11. However, since irradiation was necessary to produce the spectrum, then isolated Mn^{2+} pairs are unlikely. This data was not analyzed in detail in this study, but is included here for the sake of completeness.

B. Intrinsic V_K Centers in $NaMgF_3$

When typical crystals of $NaMgF_3$ were electron irradiated at 77 K and an ESR measurement was subsequently performed, a complex spectrum was observed for an arbitrary orientation of the applied magnetic field. Through a consideration of results obtained for other halide compounds subjected to similar irradiation treatments, this spectrum was believed to arise from V_K centers. If crystals were oriented so that the applied magnetic field was approximately perpendicular to one of the pseudocubic faces, then the spectrum would exhibit a fairly high degree of symmetry. One such spectrum is shown in Figure 20 following electron irradiation for 20 minutes (10 μA) at 77 K. Upon warming the crystal to room tem-

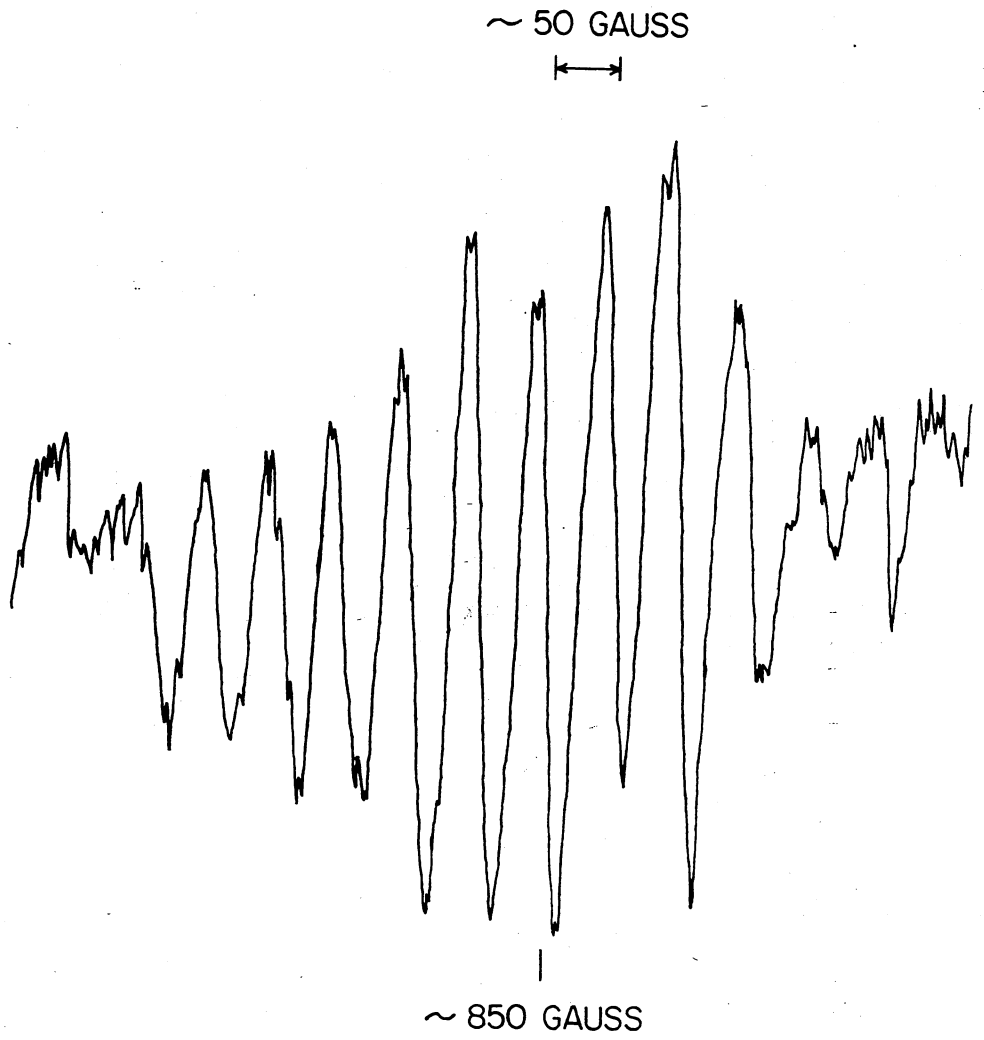

Figure 19. Unidentified ESR Spectrum Obtained After Electron Irradiation at 77 K Followed by Warming to Room Temperature

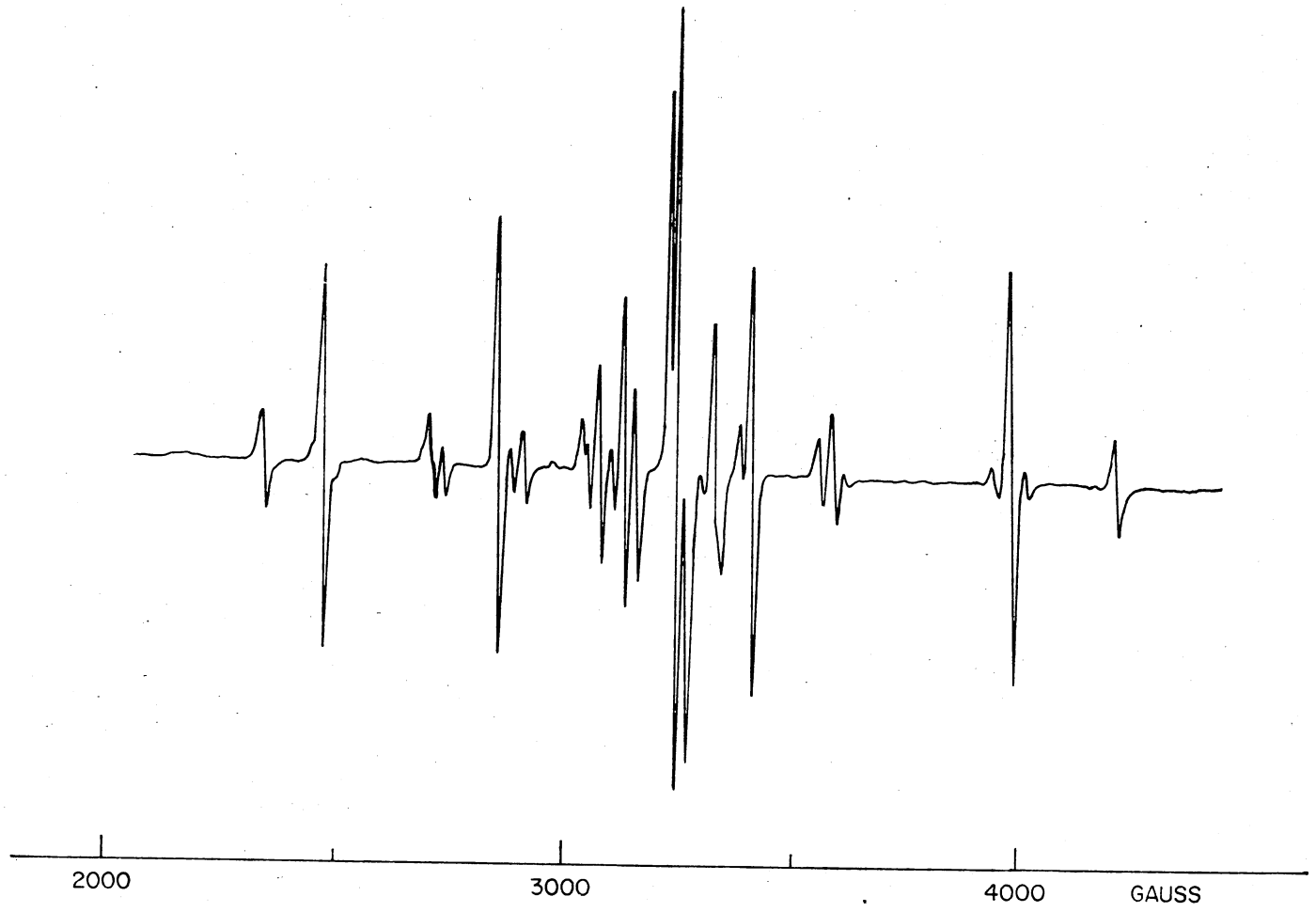

Figure 20. ESR Spectrum for $NaMgF_3$ Obtained Following Electron Irradiation at 77 K. H || [010], Typical Twinned Crystal

perature and then performing another ESR measurement at 77 K, there remained a spectrum which exhibited [100]-type symmetry, i.e., the maximum splitting of the lines occurred for an orientation of the applied magnetic field perpendicular to one of the pseudocubic faces. This spectrum is shown in Figure 21. The analysis of this data, given in the next chapter, yielded a model for the center giving rise to this spectrum (Figure 21) as originating in a self-trapped hole with its molecular axis aligned parallel to an [010] direction in the crystal. Note that lines 1 and 2 in the spectrum are not the same intensity as lines 3 and 4. In fact, these intensities were found to vary considerably from sample to sample as may be seen in Figure 22, which depicts a spectrum obtained in the same way as for Figure 21, but using a different arbitrarily chosen crystal. The lines arise from two mutually perpendicular orientations of the V_K center molecular axes, i.e., one orientation is approximately parallel to the magnetic field and the other orientation is approximately perpendicular to the magnetic field. This was verified experimentally by rotating the crystal 90^{o} about an axis perpendicular to the magnetic field and observing that the line positions interchanged (Figure 23). The variation in intensities was attributed to twin related domains in the crystal. Only one type of domain structure was discernable in the ESR spectra.

As described in Chapter II, a crystal was found which was determined to be essentially a single domain, i.e., there was no evidence of twinning as reflected in the V_K center ESR spectra. For this single domain crystal, the spectrum generated through the same irradiation procedure as for Figure 21 is shown in Figure 24. It can be seen that there is but one orientation of the center in this crystal as was ex-

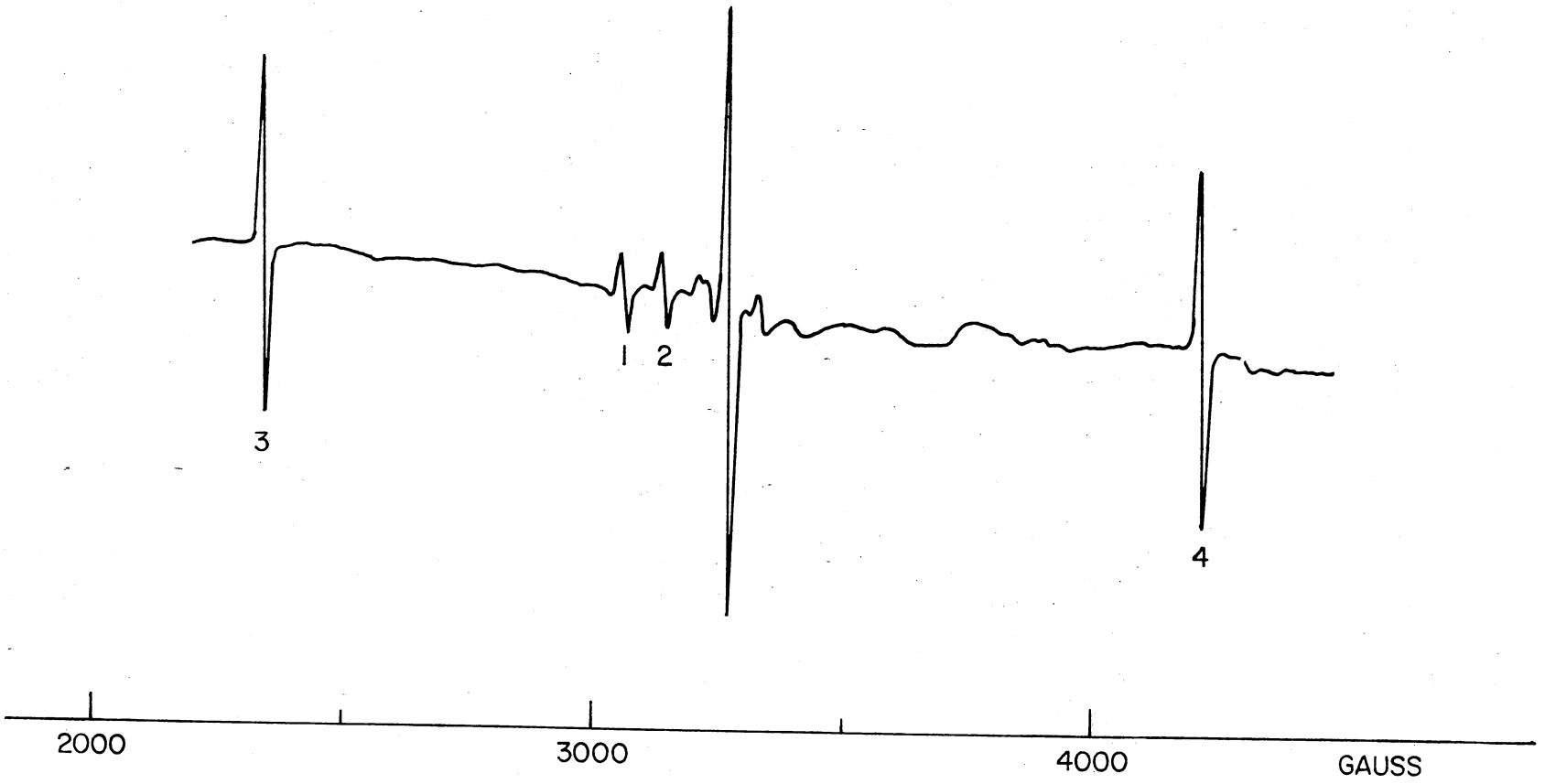

Figure 21. ESR Spectrum for $NaMgF_3$ Following an Anneal to Room Temperature. H || [010], Typical Twinned Crystal

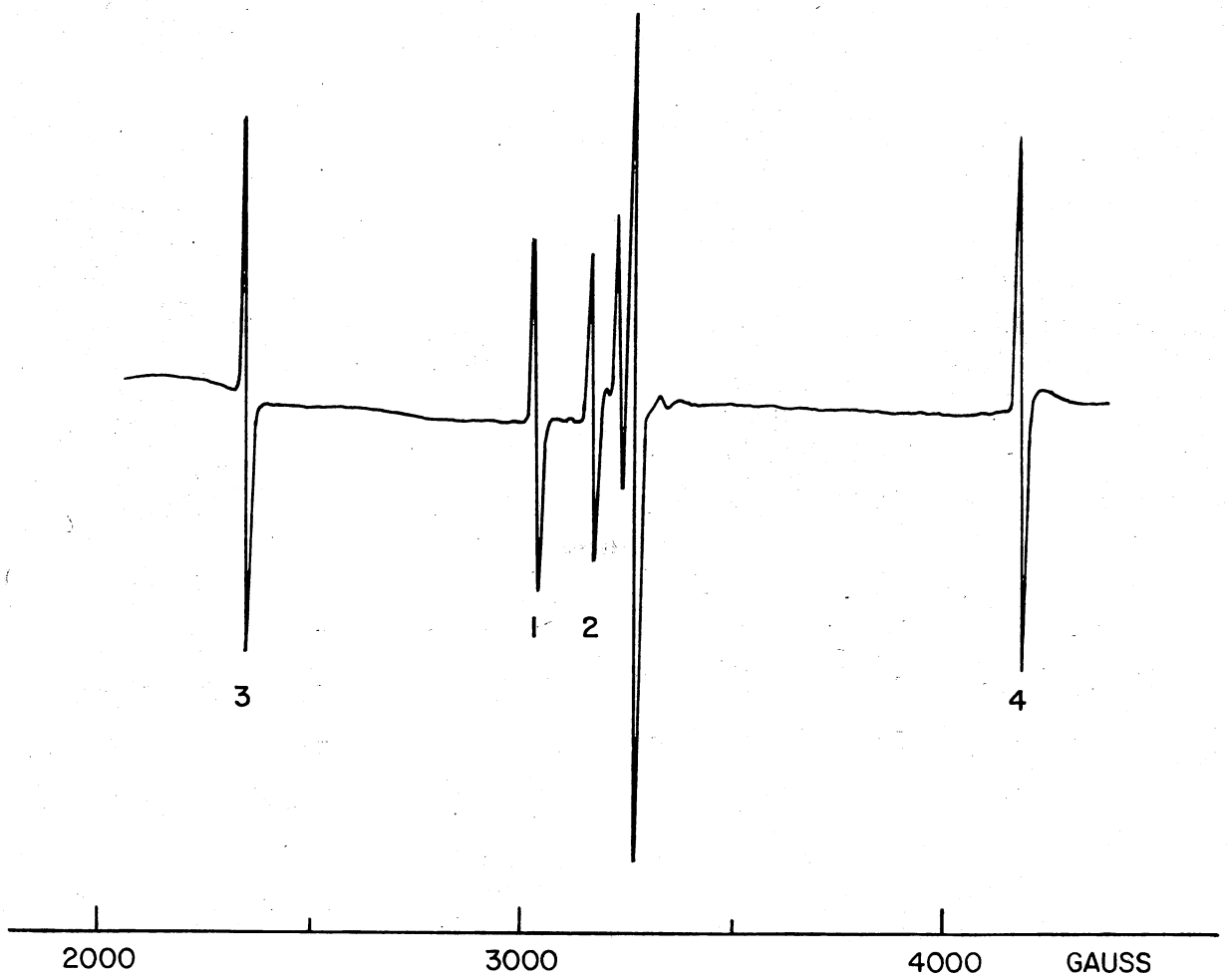

Figure 22. ESR Spectrum for $NaMgF_3$ Following an Anneal to Room Temperature. H || [010], Typical Twinned Crystal--Different Domain Structure

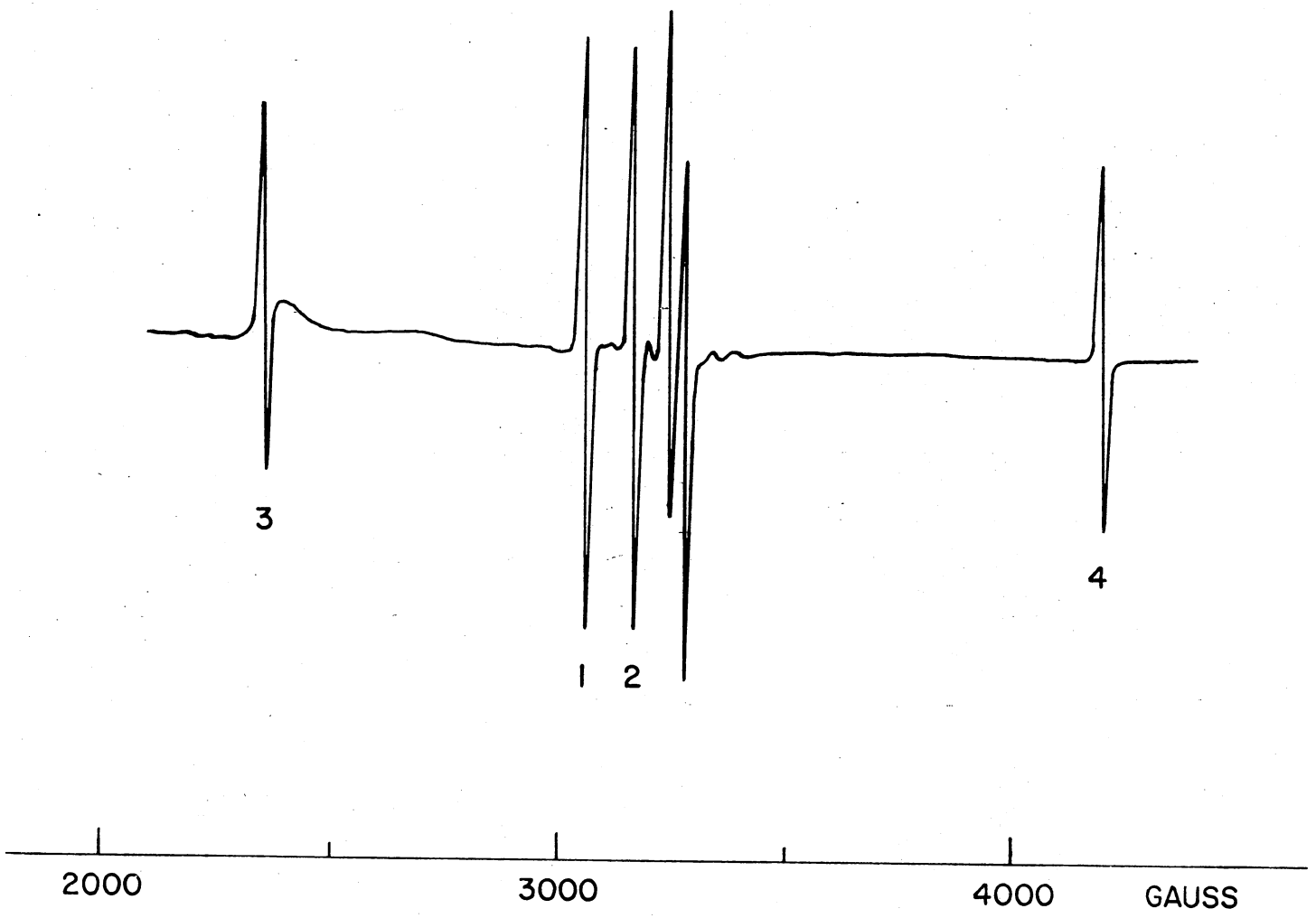

Figure 23. ESR Spectrum for $NaMgF_3$ Following an Anneal to Room Temperature. H || [100], Typical Twinned Crystal

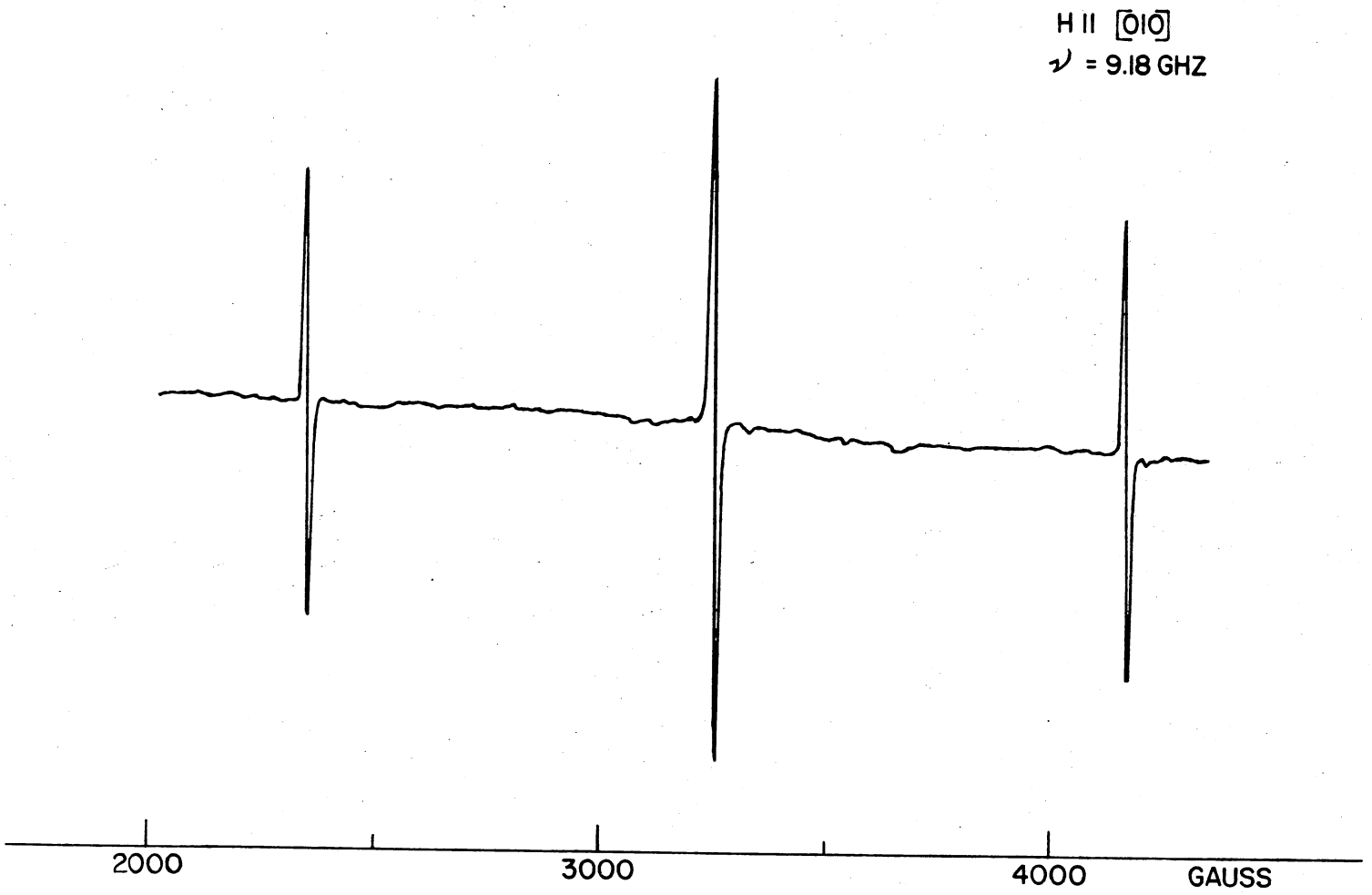

Figure 24. ESR Spectrum for $NaMgF_3$ Following an Anneal to Room Temperature. H || [010], Single Domain Crystal

pected. The other mutually perpendicular orientation would have originated in the other domain had it been present. Because of its symmetry, the defect giving rise to this spectrum will henceforth be referred to as a [100]-type V_K center.

The existence of the [100]-type V_K center allowed the magnetic field to be aligned unambiguously parallel to an [010] orientation of the cyrstal which is also parallel to the tetrad axis of rotation (see Chapter I), since the greatest splitting of the lines occurs when the magnetic field is parallel to the molecular axis of this defect. This experimental fact further aided the analysis of the spectrum generated immediately following electron irradiation at 77 K. The spectrum obtained following electron irradiation for 10 minutes at 16 μA using the single domain crystal is shown in Figure 25. Lines 1 and 14 arise from the [100]-type V_K center, thus verifying that this defect was produced by the initial irradiation at 77 K. The analysis (Chapter IV) of the other resonances in the spectrum (Figure 25) yielded the result that lines 2, 4, 6, 8, 9, 11 and 13 arise from V_K centers of the same type as those found in $KMgF_3$ in that they are formed between fluorines on the same octahedron. These will be referred to as [110]-type V_K centers. Lines 3, 5, 7, 10 and 12 arise from fluorine molecular ions, but no precise model has been developed for these centers in this study.

ESR measurements taken for 77 K electron irradiation times ranging from 20 seconds to 20 minutes invariably yielded the same spectrum, i.e., the ESR lines associated with all the V_K centers were observed to grow in simultaneously. For example, in Figure 25 the ratio of the intensity of line 13 (part of the [110]-type V_K spectrum) to line 14 (part of the [100]-type V_K spectrum) was always ~4.8 if the sample temperature

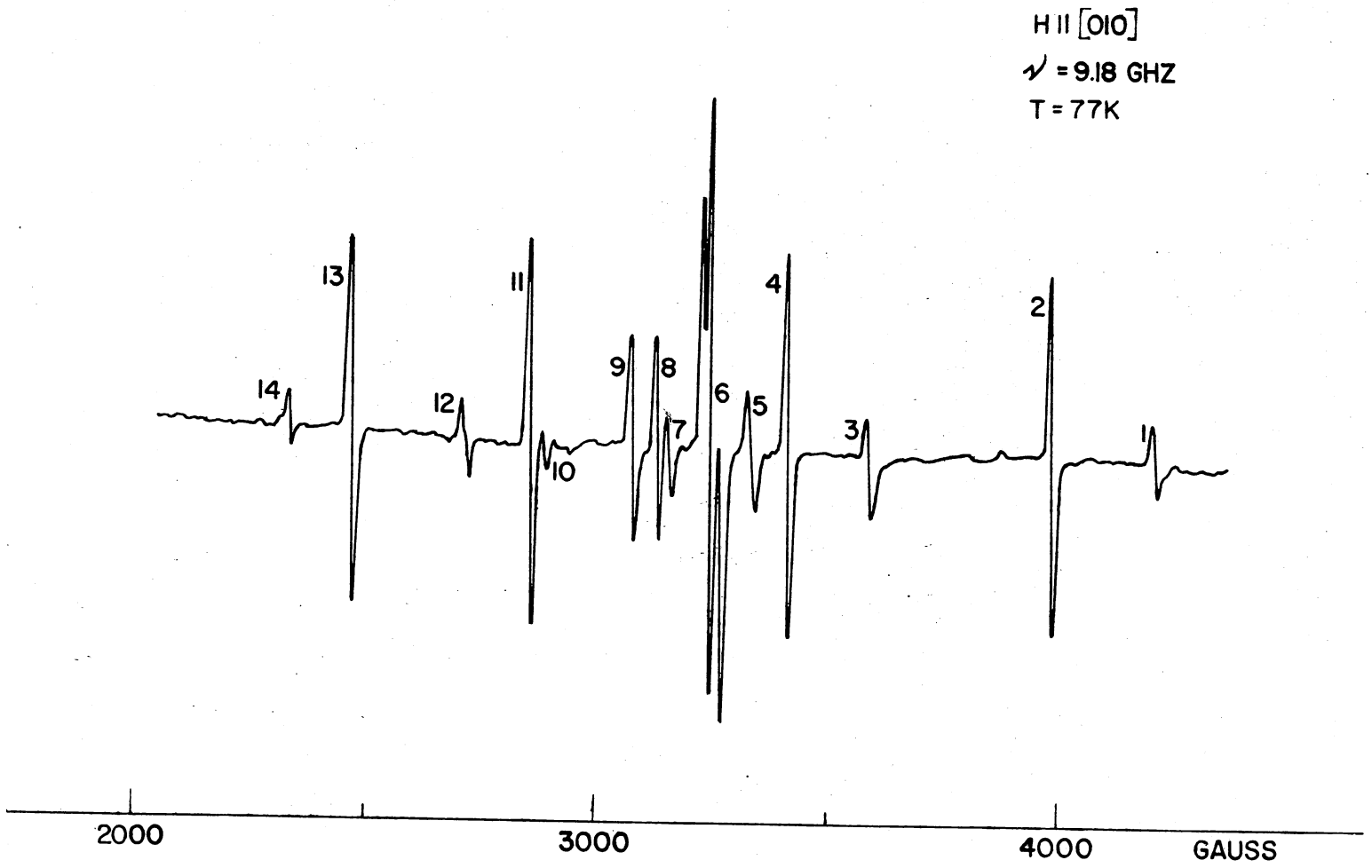

Figure 25. ESR Spectrum for $NaMgF_3$ Following Electron Irradiation at 77 K. H || [010], Single Domain Crystal

was maintained at 77 K. No detailed production study of the V_K centers was performed, but the intensity of the spectrum was found to saturate for electron irradiations of 10-20 minutes at 77 K.

The spectrum shown in Figure 25 is for an orientation of the applied magnetic field parallel to an [010] direction since, as stated previously, the maximum splitting of the lines associated with the [100]-type V_K center occurs for this orientation. The acuity of the lines associated with the [110]-type V_K center in this spectrum was not arrived at easily, i.e., fine adjustments of the magnet orientation and waveguide tilt were necessary before a precise alignment was obtained.

If after generating this spectrum (Figure 25) the crystal was rotated 90^{o} about an axis perpendicular to the applied magnetic field and a subsequent ESR measurement performed, the spectrum shown in Figure 26 was obtained. This data represents an orientation of the magnetic field parallel to a [100] direction and, as may be observed, is inequivalent to the spectrum obtained for the [010] orientation. This result was expected since these two orientations are crystallographically inequivalent, i.e., one orientation ([010]) was parallel to the tetrad axis of rotation and the other orientation ([100]) was perpendicular to this axis.

In this spectrum (Figure 26), lines 15, 16, 18, 19, 20, 21, 22, 23, 24, 25, 27, and 28 arise from the [110]-type V_K center, and the other lines (17 and 26) arise from unidentified fluorine molecular ions. For this orientation, the molecular axis of the [100]-type V_K center will be perpendicular to the magnetic field and will therefore give rise to lines in the center portion of the spectrum, i.e., underneath lines 21, 22, and 23.

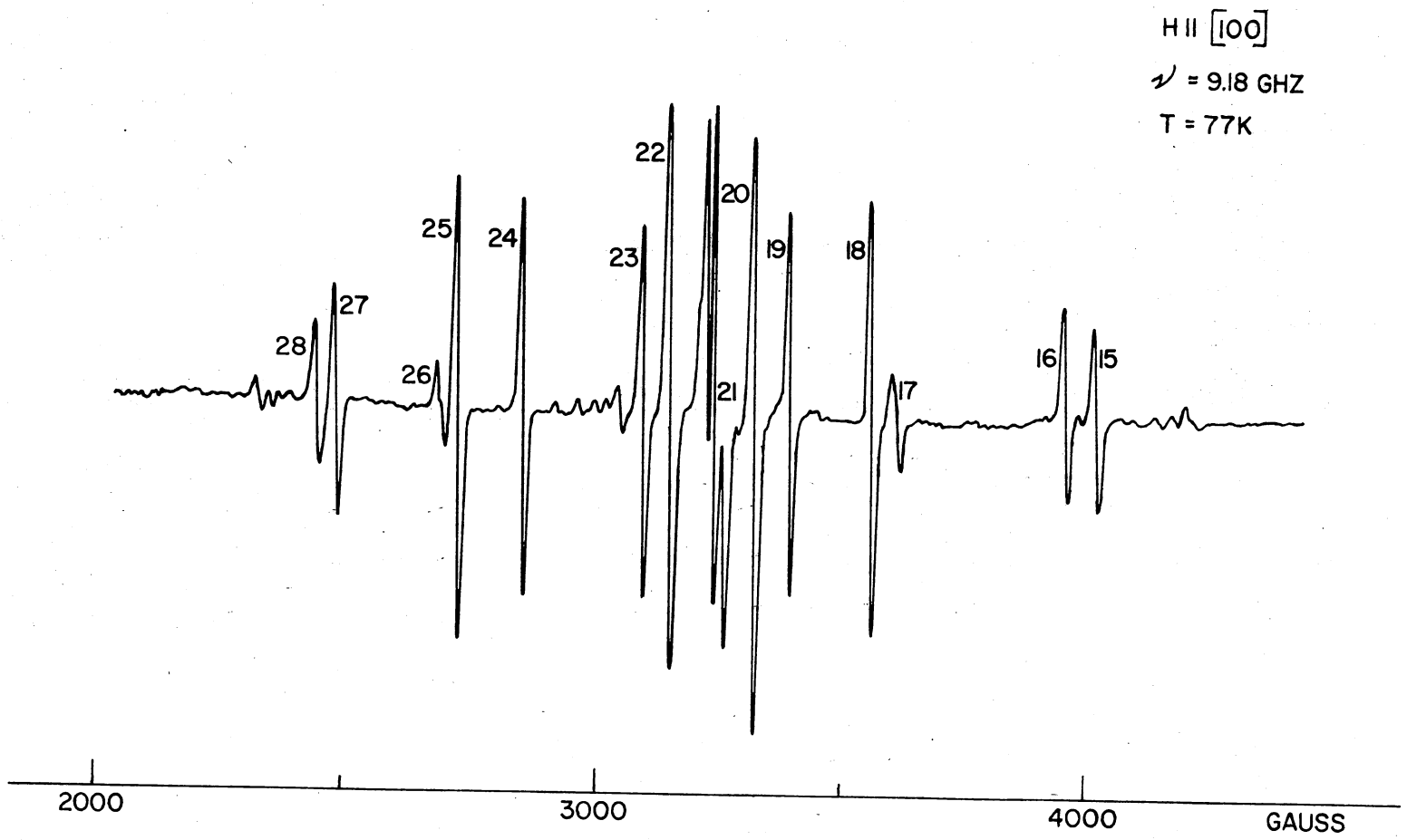

Figure 26. ESR Spectrum for $NaMgF_3$ Following Electron Irradiation at 77 K. H || [100], Single Domain Crystal

The influence of the domain structure in typical crystals may now be understood upon reexamination of Figure 21. If the spectrum shown in Figure 26 is superimposed onto that shown in Figure 25, the spectrum of Figure 21 will then be obtained upon adjusting the line intensities to account for the fact that the crystal was composed primarily of the domain associated with Figure 25.

The corrected experimental field values together with those calculated in the analysis are given in Table II for the resonances numbered in Figures 25 and 26. The microwave frequency during the course of these measurements was 9.1819680 MHz. No magnetic field measurements were performed for the resonances associated with the isolated [100]-type V_K center spectrum obtained after the [110]-type V_K centers were eliminated by warming to room temperature. This was due to the fact that an exact alignment of this center relative to the applied magnetic field could not be made with absolute certainty, somewhat paradoxically, because of the great simplicity of the spectrum, i.e., the acuity of the lines associated with the [110]-type V_K center was the strong criterion for exact alignment in the spectra obtained immediately after electron irradiation at 77 K, and this criterion was lost after warming the sample beyond the thermal decay temperature of the [110]-type V_K center.

When a sample was electron irradiated at 77 K and then exposed to the unfiltered output of a mercury lamp for ~ 5 minutes, a subsequent ESR measurement revealed that the V_K centers had been bleached, i.e., no V_K center resonances were observed. This behavior is typical for intrinsic V_K centers and is due to the release of electrons from traps annihilating the self-trapped holes. All types of V_K centers bleached

TABLE II

CORRECTED FIELD POSITIONS (IN GAUSS) OF RESONANT LINES FOR THE ESR SPECTRA ARISING FROM THE INTRINSIC SELF-TRAPPED HOLES IN $NaMgF_3$

H || [010]			H || [100]		
Line	Experimental	Calculated	Line	Experimental	Calculated
1	4201.44	---	15	4011.44	4016.98
2	3980.69	3952.38	16	3947.07	3949.23
3	3592.14	---	17	3612.84	---
4	3415.59	3431.85	18	3556.78	3562.98
5	3333.70	---	19	3402.93	3422.89
6	3251.17	---	20	3333.75	---
7	3157.62	---	21	3251.90	---
8	3137.10	---	22	3161.69	---
9	3082.14	---	23	3108.94	3089.21
10	2890.11	---	24	2871.50	2873.97
11	2859.61	2866.48	25	2740.35	2750.64
12	2717.42	---	26	2705.71	---
13	2473.99	2504.12	27	2494.56	2506.23
14	2344.96	---	28	2457.31	2468.71

equally at 77 K. After warming a sample to room temperature following a 77 K electron irradiation so that all that remained were the [100]-type V_K centers and then applying uv light after the sample had been recooled to 77 K, it was found that bleaching of the [100]-type V_K centers alone was not as effective as bleaching the entire spectrum obtained directly following the 77 K electron irradiation. This result was anticipated, since in the process of warming the sample to room temperature a large share of the trapped electrons which would have been bleached by the light were annihilated by the thermally activated [110]-type hole centers.

The results of a pulse anneal study of the V_K centers formed through electron irradiation at 77 K are shown in Figure 27. This data was obtained by pulse annealing for three minutes at progressively higher temperatures. The monitoring temperature was 89 K. The figure is divided into two parts. In Figure 27(a) the thermal decay of the [110]-type V_K center spectrum is depicted and shows that this center becomes thermally unstable at approximately 120 K. In Figure 27(b) it can be observed that at this same temperature (120 K) the [100]-type V_K center spectrum, which was present initially at 77 K, increases in intensity and does not become thermally unstable until near room temperature (~ 295 K). Tolerances of at least ±10 K must be placed on these transition temperatures due to the fact that in the transfer of the crystal from the liquid nitrogen bath to the microwave cavity, which was maintained at ~ 89 K by flowing nitrogen gas, the crystal temperature rose beyond the transition temperature as could be ascertained by comparing the intensity of the [110]-type V_K center spectrum to that of the [100]-type V_K center, and this could have influenced the temperature

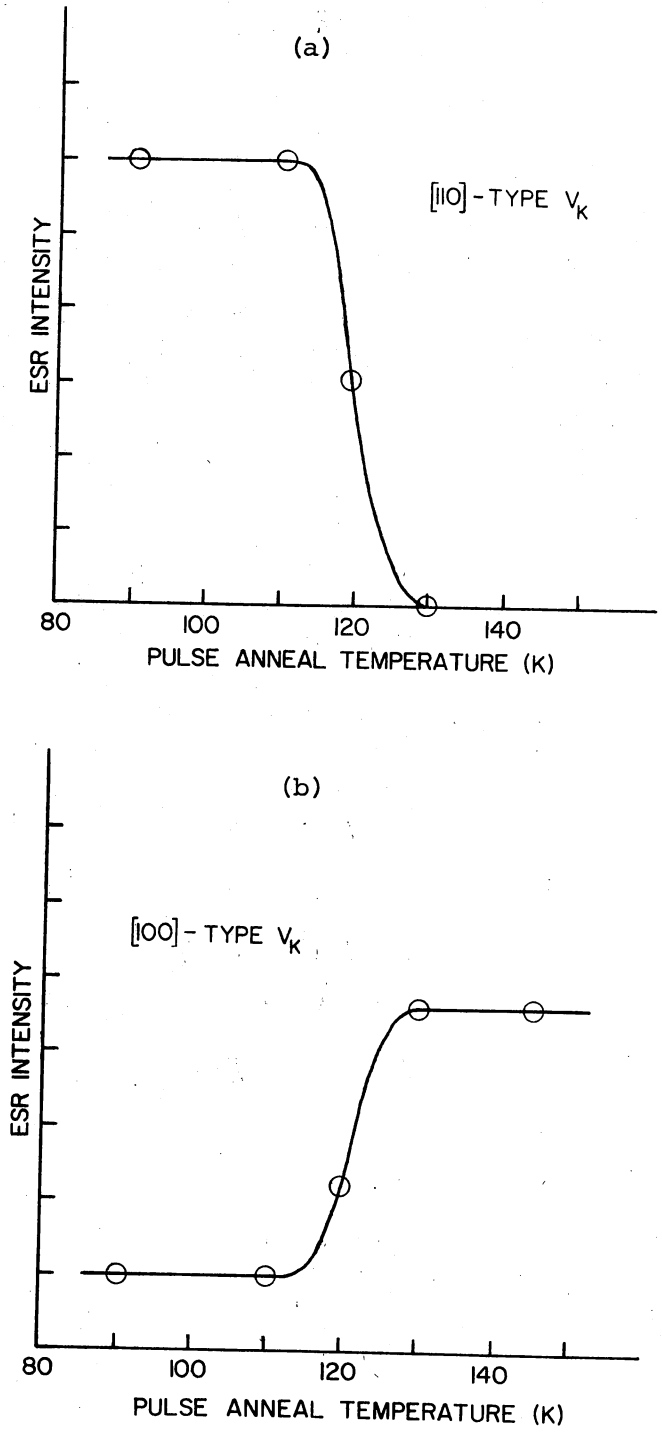

Figure 27. Pulse Anneal Study of the Intrinsic V_K Centers Produced in $NaMgF_3$ by an Electron Irradiation at 77 K. (a) Thermal Decay of the [110]-Type V_K Center; (b) Thermal Decay of the [100]-Type V_K Center

of maximum change in the intensity of the spectra. Furthermore, the thermal decay temperature of the [100]-type V_K center (295 K) was not explicitly obtained in the pulse anneal study, but was arrived at in consideration of the fact that a few of these centers could still be detected if crystals were allowed to remain at room temperature in darkness up to 10 minutes.

Thermoluminescence was also obtained between 77 K and 600 K following electron irradiation at 77 K. A typical TSL measurement is shown in Figures 28(a), (b), and (c) following a 77 K electron irradiation of 5 minutes at 10 μA. TSL glow peaks were found to occur at temperatures of 133 K, 180 K, 212 K, 246 K, 286 K, 317 K, 365 K, 402 K, and 573 K. The glow peak at 133 K, which was by far the strongest peak in the TSL data, is associated with the thermal decay of the [110]-type V_K centers, and the luminescence thus competes with the conversion of these holes into [100]-type V_K centers.

A reduction in the TSL intensity was found to occur if following the 77 K electron irradiation samples were exposed to the unfiltered output of a mercury lamp. In Figure 29 is shown the TSL obtained between 77 K and room temperature following a 77 K electron irradiation for 5 minutes at 10 μA followed by application of uv light for 30 minutes. As a result of the uv bleach, the TSL intensity was reduced by more than two orders of magnitude, but was still easily discernable. This result was indicative of the high relative sensitivity of the TSL technique, since only 5 minutes of uv bleaching was required to completely annihilate the V_K center ESR spectra under comparable experimental conditions.

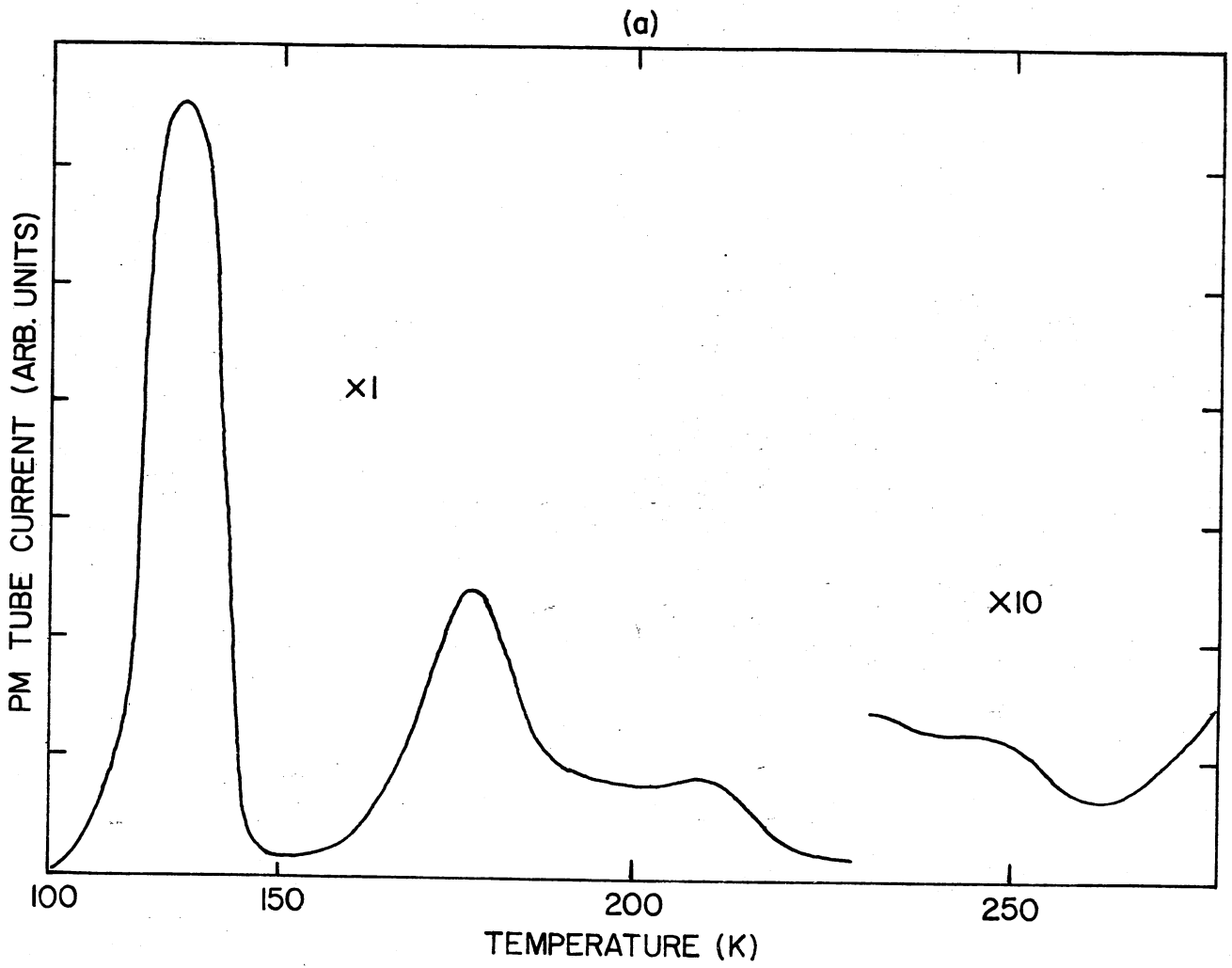

Figure 28. Thermoluminescence Obtained for $NaMgF_3$ Following Electron Irradiation at 77 K: (a) 100 K → 273 K

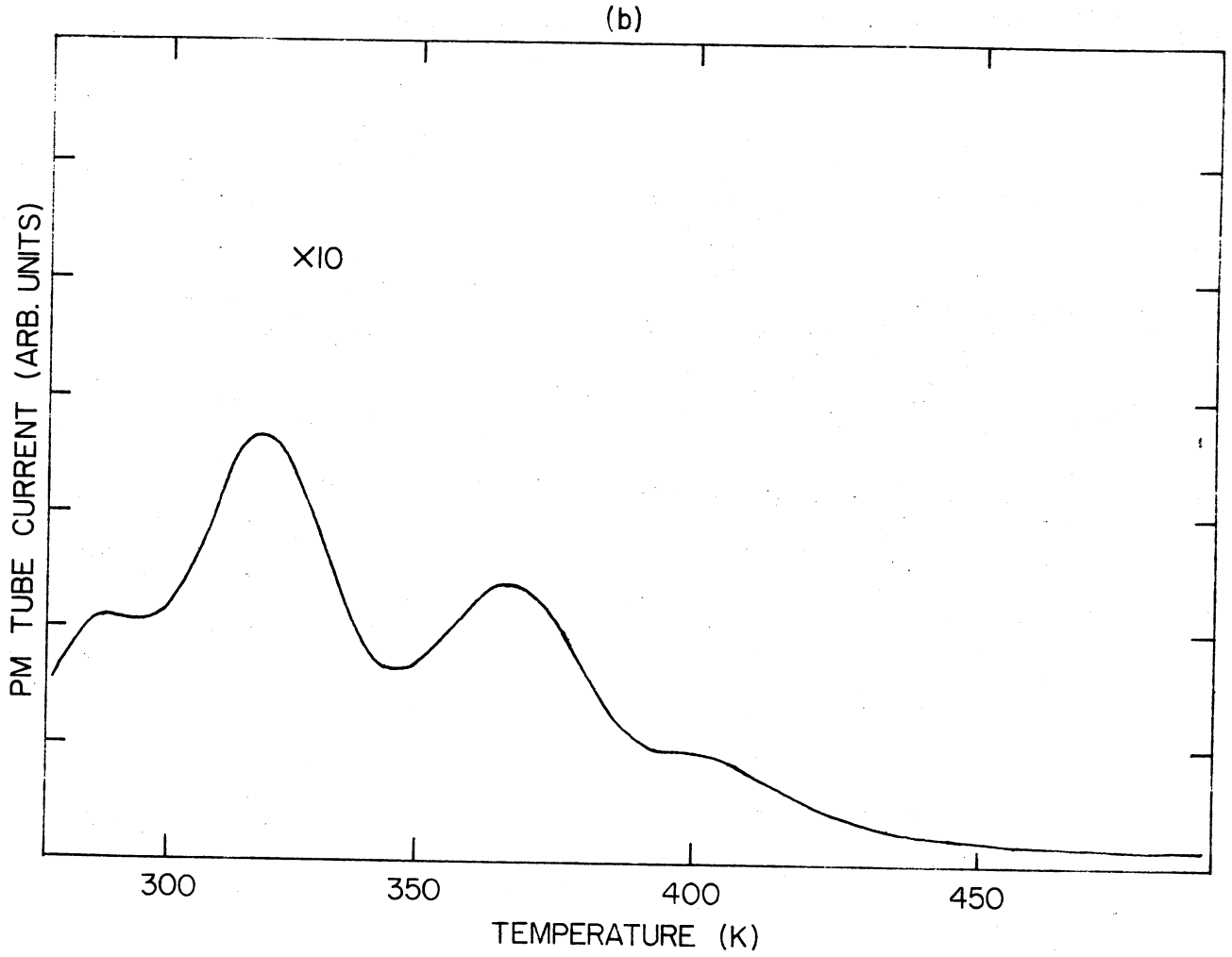

Figure 28. Thermoluminescence Obtained for $NaMgF_3$ Following Electron Irradiation at 77 K: (b) 273 K → 485 K

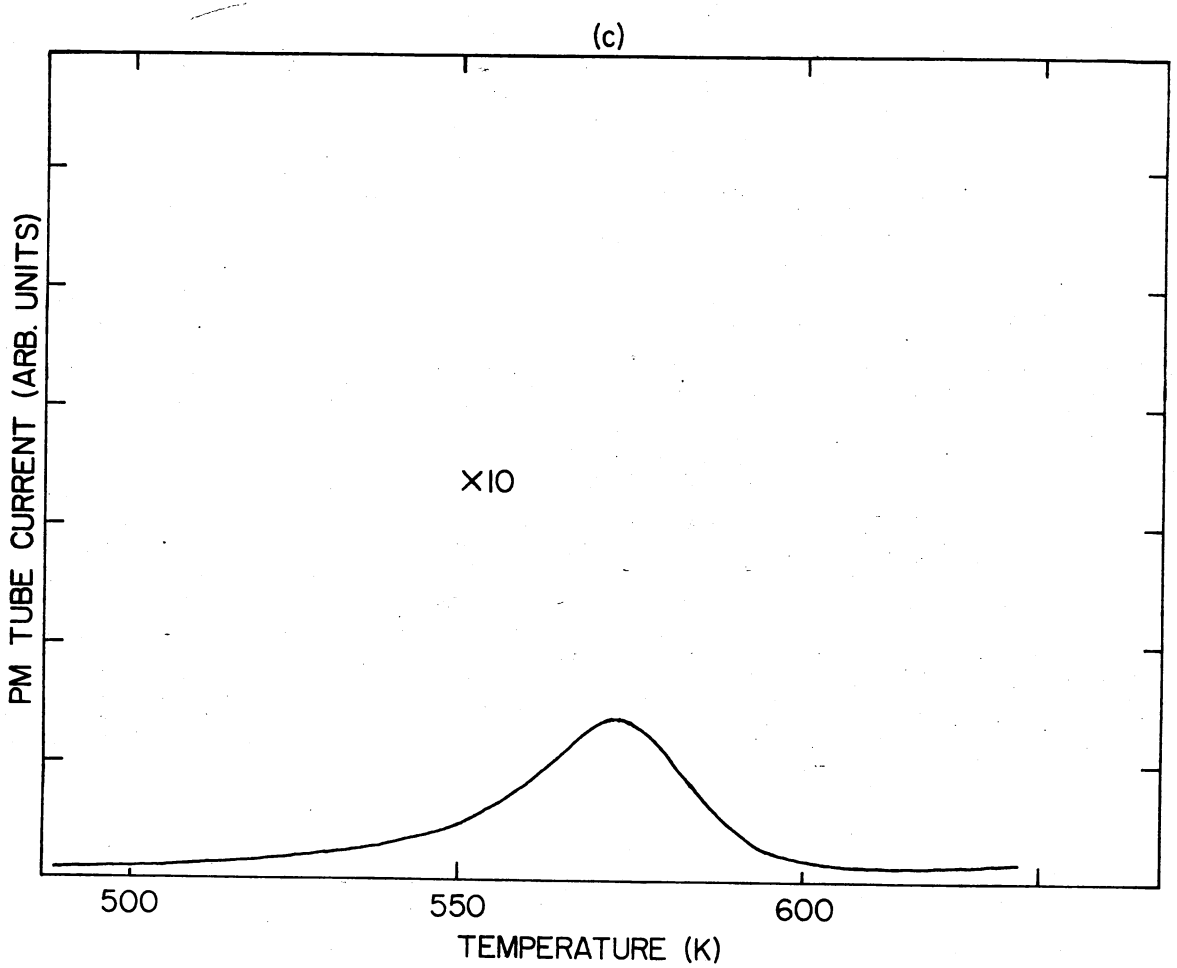

Figure 28. Thermoluminescence Obtained for $NaMgF_3$ Following Electron Irradiation at 77 K: (c) 485 K → 600 K

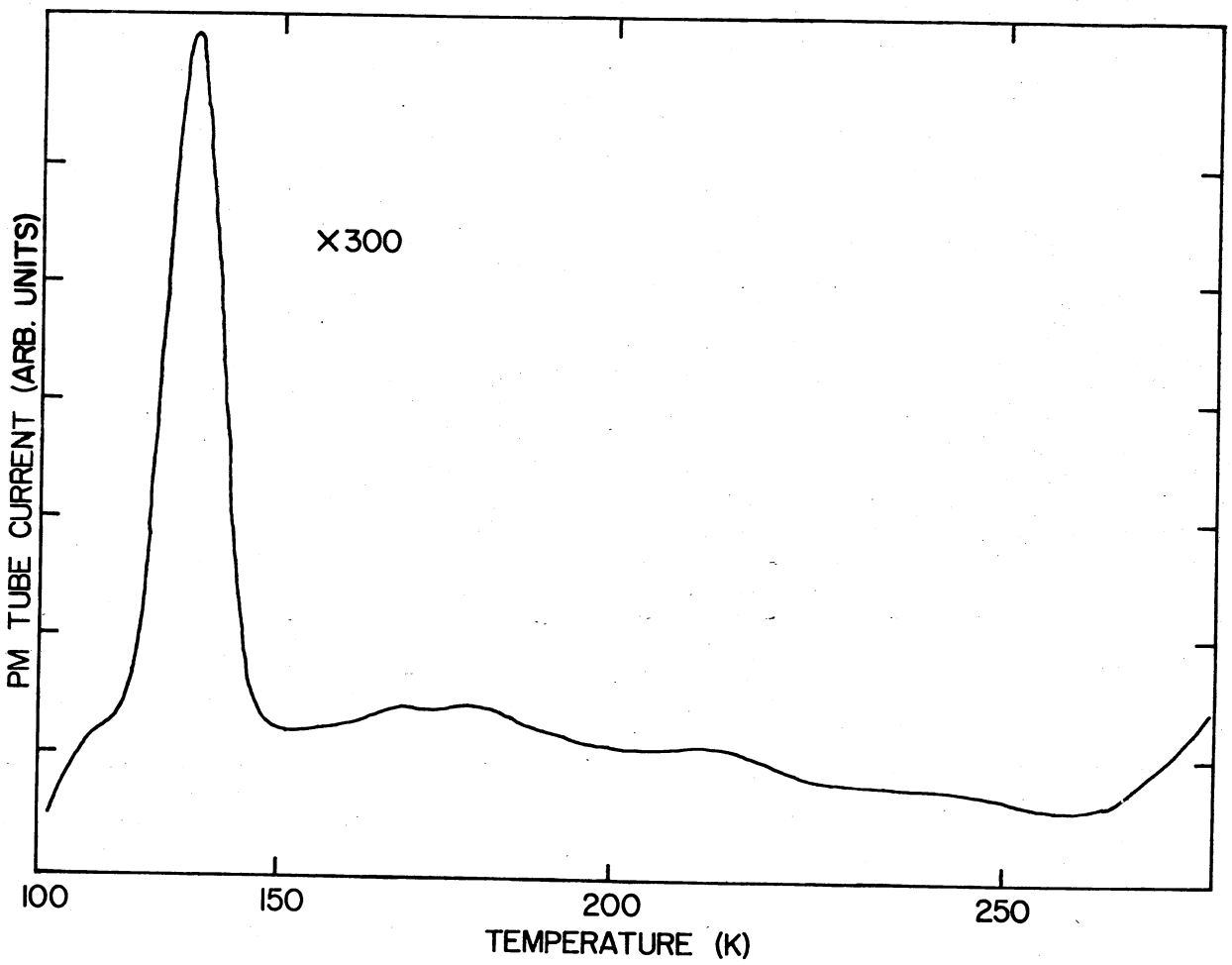

Figure 29. Thermoluminescence Obtained for $NaMgF_3$ Following Electron Irradiation at 77 K and Application of uv Light (100 K - 273 K)

CHAPTER IV

ANALYSIS AND DISCUSSION

A complete analysis of the experimental results will be given in this chapter. As in the previous chapter, this presentation will be divided into two separate parts with the first section being devoted to an analysis of the Mn^{2+}-fluorine vacancy ESR spectrum and a discussion of the complementary TSL measurements. The second part will be concerned primarily with an analysis of the ESR spectra associated with self-trapped holes in $NaMgF_3$.

A. Analysis of the Mn^{2+}-Fluorine Vacancy Center

In the as-grown $KMgF_3$:Mn crystals only the cubic Mn^{2+} ESR spectrum was present, and no additional spectra were observed to grow in as a result of room temperature electron irradiation. However, following the room temperature irradiation, a new spectrum appeared (Figure 12) when samples were exposed to an unfiltered mercury lamp at 77 K. This data was immediately recognized as arising from Mn^{2+} since the spectrum was characterized by a division into six-line hyperfine groups with an associated splitting of ~ 100 gauss typical for this ion. Since irradiation of a crystal was necessary to produce the spectrum, then it could not have arisen simply from a change in the electronic structure of a nearby associated defect, present in the crystal prior to irradiation, otherwise a perturbed Mn^{2+} ESR spectrum would have been observed

prior to irradiation. The spectrum required relatively large doses to produce and slowly increased in intensity with increasing duration of the initial room temperature electron irradiation. This indicated that it could not be due to a straight ionization process but must have its origin in an intrinsic defect growing in slowly with irradiation. This was further substantiated by the fact that the spectrum could be generated in the more heavily doped (8000 ppm) crystals so that the defect responsible for the spectrum was characteristic of $KMgF_3$:Mn crystals in general and not a peculiarity of the more lightly doped (400 ppm) boule. Furthermore, the spectrum was shown to have [100] symmetry, since the maximum splitting of the lines was observed to occur for orientations of the applied magnetic field parallel to [100] directions. This fact indicated that the defect associated with the Mn^{2+} ion was situated in a [100] direction relative to the Mn^{2+}.

The above observations were consistent with a model in which the initial room temperature irradiation creates an F center next to a Mn^{2+} ion, and the subsequent uv bleach at 77 K removes the F electron leaving a Mn^{2+}-fluorine vacancy center. The proposed model also explained the necessity of pre-irradiating at room temperature since exposure to uv light alone will not produce F centers in this material. Since the formation of F centers was necessary, then any irradiation procedure which produced F centers should have led to the production of the observed ESR spectrum. This was supported by the fact that γ irradiation at room temperature followed by a 77 K uv bleach as well as direct electron irradiation at 77 K would produce the ESR spectrum. The direct production at 77 K was not nearly as efficient as the combined room temperature irradiation and 77 K bleach, but this was expected since in

this irradiation procedure both F center production and ionization were necessary to produce the fluorine vacancies.

The ESR pulse anneal study yielded a thermal decay temperature of approximately 185 K for the Mn^{2+}-fluorine vacancy spectrum (Figure 16). From a study of M center formation in $KMgF_3$, Riley (64) has shown that fluorine vacancies become mobile in the temperature range 180 K - 200 K. The results of the present study provide independent confirmation of this fact when one interprets the thermal decay of the Mn^{2+}-fluorine vacancy center as resulting from movement of the vacancy away from the Mn^{2+} ion. Thus the study of similar defects in other halide compounds may be of use in the determination of unknown vacancy mobility temperatures.

Following an anneal to room temperature, the Mn^{2+}-fluorine vacancy ESR spectrum could be regenerated if an additional uv bleach was performed at 77 K (Figure 17). This regeneration effect was in fact due primarily to an incomplete ionization of the originally produced Mn^{2+}-F center pairs. However, since after attaining the saturation ESR intensity and then warming the sample to room temperature, approximately 10% of the maximum ESR intensity could be regenerated by a subsequent 1 hr. 77 K uv bleach, then a partial reformation of F centers in the process of warming the sample to room temperature could occur.

Thermoluminescence was generated following the same irradiation procedure that produced the Mn^{2+}-fluorine vacancy ESR spectrum and possessed a similar regeneration behaviour (Figure 18). However, none of the TSL glow peaks coincided with the thermal decay temperature (185 K) of the Mn^{2+}-fluorine vacancy ESR spectrum. This lack of correlation implies that no significant electron-hole recombination accom-

panies the disappearance of the ESR spectrum and thus lends further support to the proposed vacancy migration mode of thermal decay. The TSL glow peaks occurring below the thermal instability temperature of the Mn^{2+}-fluorine vacancy center must be associated with a hole release process, since thermally released electrons would have partially annihilated the Mn^{2+}-fluorine vacancy ESR spectrum and this was not observed.

The ESR spectrum associated with the Mn^{2+}-fluorine vacancy center exhibits a strong crystal field splitting. The two more widely split groups of lines in Figure 13 were observed to have turning points for <100> orientations of the applied magnetic field. The <100> orientations also gave the best resolution of the superhyperfine structure (Figure 14). These results implied that the principal axes of the crystal field interaction must be the three mutually perpendicular <100> crystalline directions. In the initial ESR analysis of the Mn^{2+}-fluorine vacancy spectrum, it was assumed that the crystal field symmetry was perfectly axial. However, a good fit of the experimental line positions to a simple axial spin Hamiltonian could not be achieved. For a complete description of the ESR spectrum, the following spin Hamiltonian was necessary:

$$H = g\beta\vec{H}\cdot\vec{S} + \frac{a}{6}[S_x^4 + S_y^4 + S_z^4 - \frac{1}{5}S(S+1)(3S^2 + 3S - 1)]$$

$$+ D[S_z^2 - \frac{1}{3}S(S+1)] + E[S_x^2 - S_y^2] + \frac{F}{180}[35S_z^4 - 30S(S+1)S_z^2$$

$$+ 25S_z^2 - 6S(S+1) + 3S^2(S+1)^2] + A\vec{I}\cdot\vec{S} \qquad (12)$$

The first term is the Zeeman splitting, and the terms involving the parameters a, D, E, and F arise from the splitting of the $^6S_{5/2}$ ground

state of Mn^{2+} by the crystalline electric field. The parameter a represents the cubic field contribution while D and F represent the axial field contributions of second and fourth degree respectively. The parameter E represents the non-zero rhombic contribution for symmetries lower than axial. The last term, $A\vec{I}\cdot\vec{S}$, gives the hyperfine interaction between the unpaired electrons and the manganese nucleus.

Rewriting the spin Hamiltonian in terms of the operators S_z, S_+, and S_- gives:

$$\begin{aligned} H = {} & g\beta H_z S_z + \frac{(a + 2F/3)}{120}\left[35S_z^4 - \frac{475}{2}S_z^2 + \frac{2835}{16}\right] \\ & + D\left[S_z^2 - \frac{35}{12}\right] + \frac{a}{48}\left[S_+^4 + S_-^4\right] + \frac{E}{2}\left[S_+^2 + S_-^2\right] \\ & + \tfrac{1}{2}g\beta\left[H_x - iH_y\right]S_+ + \tfrac{1}{2}g\beta\left[H_x + iH_y\right]S_- \\ & + \frac{A}{2}\left[I_+S_- + I_-S_+\right] + AI_zS_z \end{aligned} \tag{13}$$

where H_x, H_y, and H_z are the components of the magnetic field along the principal axes of the center. Note that the term $\frac{a}{48}\left[S_+^4 + S_-^4\right]$ connects states which are well separated in energy and results in only a small perturbation on the energy levels. The significant fourth order parameter is (a + 2F/3) which can be determined with much greater certainty than either a or F individually.

Twelve transformations were necessary in order to take the principal axes for the crystal field interaction into the fixed crystal axes. These transformations were

$$T = \begin{bmatrix} 0 & 1 & 0 \\ 0 & 0 & 1 \\ 1 & 0 & 0 \end{bmatrix}, \begin{bmatrix} 0 & -1 & 0 \\ 0 & 0 & -1 \\ 1 & 0 & 0 \end{bmatrix}, \begin{bmatrix} 0 & 0 & 1 \\ 0 & -1 & 0 \\ 1 & 0 & 0 \end{bmatrix},$$

$$\begin{bmatrix} 0 & 0 & -1 \\ 0 & 1 & 0 \\ 1 & 0 & 0 \end{bmatrix}, \begin{bmatrix} -1 & 0 & 0 \\ 0 & 0 & 1 \\ 0 & 1 & 0 \end{bmatrix}, \begin{bmatrix} 1 & 0 & 0 \\ 0 & 0 & -1 \\ 0 & 1 & 0 \end{bmatrix}, \tag{14}$$

$$\begin{bmatrix} 0 & 0 & 1 \\ 1 & 0 & 0 \\ 0 & 1 & 0 \end{bmatrix}, \begin{bmatrix} 0 & 0 & -1 \\ -1 & 0 & 0 \\ 0 & 1 & 0 \end{bmatrix}, \begin{bmatrix} -1 & 0 & 0 \\ 0 & -1 & 0 \\ 0 & 0 & 1 \end{bmatrix},$$

$$\begin{bmatrix} 1 & 0 & 0 \\ 0 & 1 & 0 \\ 0 & 0 & 1 \end{bmatrix}, \begin{bmatrix} 0 & -1 & 0 \\ 1 & 0 & 0 \\ 0 & 0 & 1 \end{bmatrix}, \begin{bmatrix} 0 & 1 & 0 \\ -1 & 0 & 0 \\ 0 & 0 & 1 \end{bmatrix}.$$

The crystal axes were then transformed into the magnetic field system for an arbitrary orientation of H through the use of

$$R = \begin{bmatrix} \cos\theta & -\sin\theta \sin\phi & \sin\theta \cos\phi \\ 0 & \cos\phi & \sin\phi \\ -\sin\theta & -\cos\theta \sin\phi & \cos\theta \cos\phi \end{bmatrix}. \tag{15}$$

The spin Hamiltonian was expressed in the form of a 36 x 36 matrix by using the $|m_S, m_I>$ basis set where S = 5/2 and I = 5/2. The determination of the parameters was accomplished through repeated diagonalization of the 36 x 36 matrix (Appendix E). The computer program (Appendix A) was designed to systematically increment the Hamiltonian para-

meters until a "best" fit to experimentally measured line positions in the [100] spectrum was obtained. The values for the calculated parameters are:

$$\begin{aligned} g &= 2.0018 \pm 0.001 \\ D &= -588.4 \pm 1 \text{ gauss} \\ |E| &= 115.5 \pm 0.5 \text{ gauss} \\ a + 2F/3 &= 3.5 \pm 1 \text{ gauss} \\ A &= -100.3 \pm 1.5 \text{ gauss} \end{aligned} \tag{16}$$

The signs of the parameters were determined by assuming that A was negative. The tolerances were arrived at by assuming that the magnetic field measurements were accurate to within ± 1 gauss. A separate program (Appendix B) was used to predict line positions.

The most striking feature of the Mn^{2+}-fluorine vacancy ESR spectrum is the deviation from purely axial symmetry. Such a deviation is not unreasonable when one considers the degree of openness in the cubic perovskite structure (Figure 3). The effective charge of the fluorine vacancy exerts a repulsive electrostatic force on the Mn^{2+} ion. This in turn causes the axial fluorine on the opposite side of the Mn^{2+} ion from the vacancy to be displaced slightly in one of four equivalent <100> directions at right angles to the defect axis. These four equivalent <100> directions are relatively open in the cubic perovskite structure and thus easily allow such displacements. This suggested structural model is illustrated in Figure 30. Further investigation of the partially resolved fluorine superhyperfine structure by means of the ENDOR technique may provide additional evidence to support the proposed model.

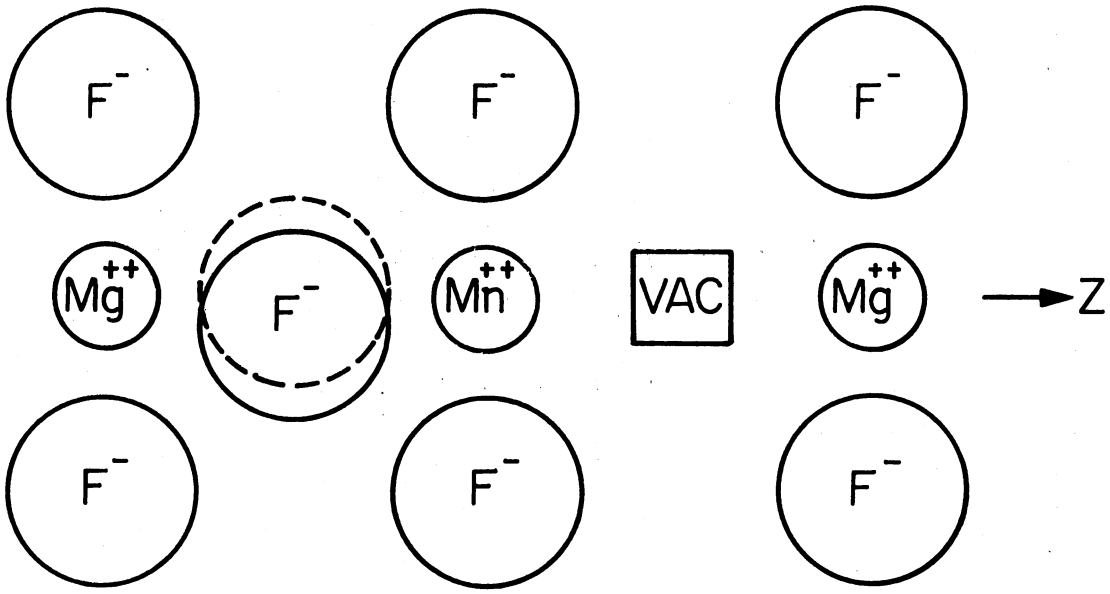

Figure 30. Defect Model for the Mn^{2+}-Fluorine Vacancy Center

B. Analysis of Intrinsic V_K Centers in $NaMgF_3$

[110]-Type V_K Centers

As stated in Chapter I, the MgF_6 octahedra in $NaMgF_3$ are expected to remain regular with fluorine-fluorine separations comparable to those found for octahedra in $KMgF_3$. One therefore would expect V_K centers to be formed in $NaMgF_3$ which are morphologically the same as those found in $KMgF_3$ in that they are formed between fluorines on an octahedron. This has been confirmed by the analysis, which is given in this section of the experimental data obtained following electron irradiation at 77 K; and the self-trapped holes so formed are labeled [110]-type V_K centers by analogy with the symmetry of comparable defects in the ideal structure ($KMgF_3$). Before discussing the details involved in the diagonalization of the matrix representation of the spin Hamiltonian and the sophisticated computer programming techniques used therein, a presentation of the evolution of the logic which resulted in the final model for the spectra will be given.

In the crystal structure of $NaMgF_3$ (see Chapter I), the tilting of the individual octahedra may be understood in terms of a resolution of the resultant tilt into two distinct rotations. The initial rotation (ω) is about a tetrad axis parallel to an [010] direction. This is followed by a rotation (ϕ) about a diad axis of the octahedron. In a specific layer of octahedra in an (010) plane of the crystal, there are two inequivalent octahedra distinguishable by the sense ($\pm$) of each component rotation relative to the ideal (untilted) structure. The octahedra in a mirror layer above or below this specified layer will individually have the same sense of rotation about the tetrad axis

([010]), but respectively opposite rotations about a diad axis. Thus there are four distinguishable octahedra which are individually characterized by the sense of each rotation. These four octahedra are shown in segregated form in Figure 31. The labels A^{++} and B^{--} are assigned to the dissimilar octahedra found in the layer illustrated in Figure 4, and the labels C^{+-} and D^{-+} are assigned to the inequivalent octahedra in the mirror layer directly above (or below) this layer. The first superscript to the right of each letter indicates the sense (±) of the tetrad rotation, and the second superscript indicates the sense of the diad rotation. For example consider the A^{++} type of octahedron. The rotation about the tetrad axis perpendicular to the plane of the figure is counterclockwise (+). This is followed by the diad rotation (+) which lifts two fluorines out of the plane of the figure (denoted by +) and lowers two fluorines through the plane of the figure (denoted by -). In the orthorhombic crystal structure, the C^{+-} type of octahedron is found directly above the A^{++} type and has the same tetrad rotation, but the diad rotation is constrained, by the octahedra above and below the C^{+-}, to have an opposite sense (-).

Of the twelve possible [110]-type V_K centers that can potentially be formed on an octahedron, there are at most six that can be inequivalent for an arbitrary orientation of the applied magnetic field, i.e., there can be no more than six different angles between the applied magnetic field and the twelve V_K center molecular axes. This simplification enables one to consider without loss of generality only those V_K centers formed on the upper half of each octahedron. These six inequivalent V_K centers are labeled 1-6 in Figure 31.

Note that for orientations of the applied magnetic field parallel

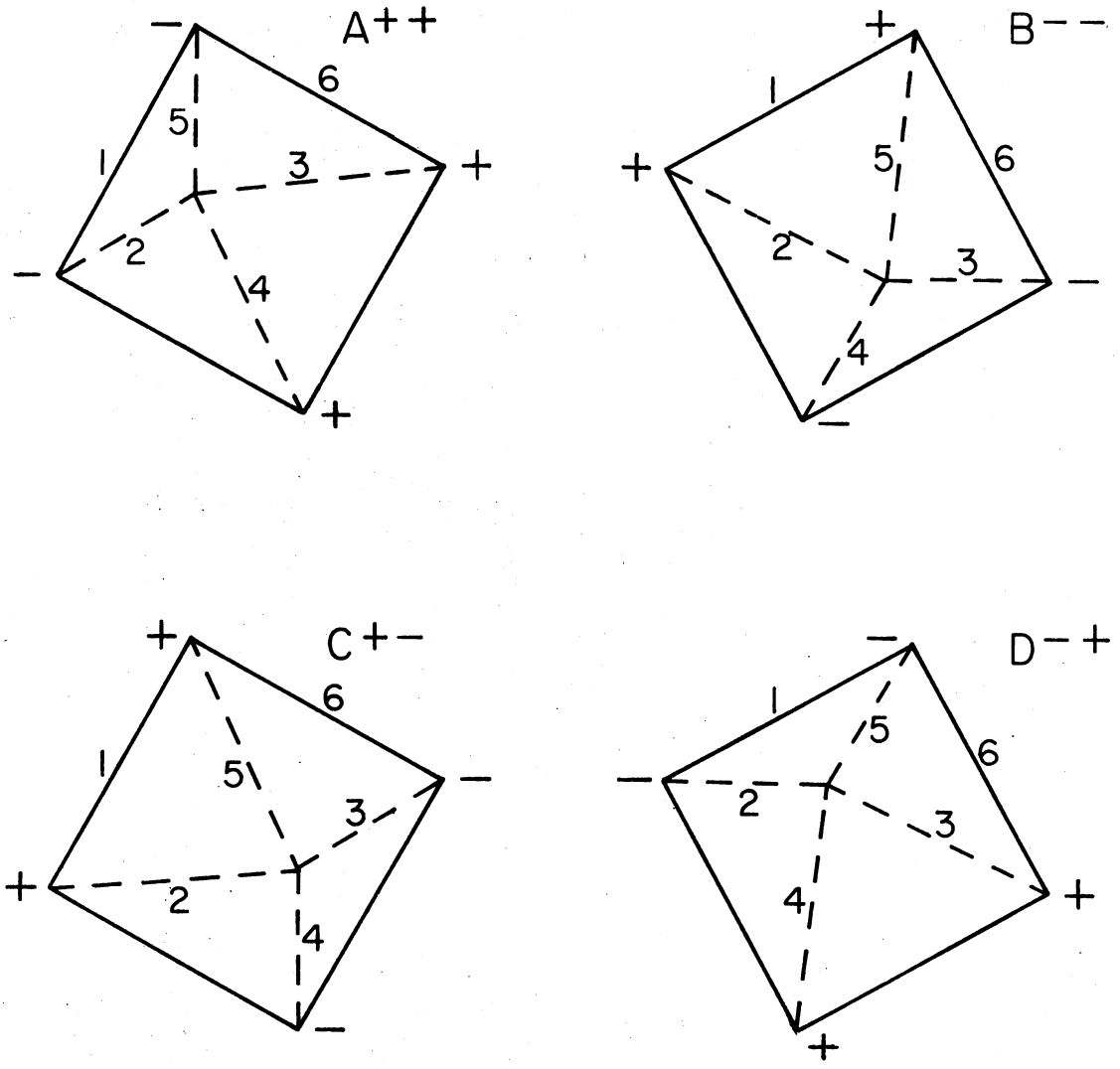

Figure 31. The Four Types of Octahedra in the Crystal Structure of $NaMgF_3$

to the tetrad axis, which is perpendicular to the plane of Figure 31, that the magnitude of the tetrad rotation (ω) will have only second order effects on the angles between the magnetic field and the V_K center molecular axes. Thus the ESR spectrum obtained for this orientation of the magnetic field will contain no information pertinent to the evaluation of ω. Furthermore, all four types of octahedra (A, B, C, D)* will be equivalent for this orientation of the magnetic field so that in the analysis of the ESR data it is necessary to consider only one octahedron. This equivalency may be explicitly expressed in terms of the individual V_K centers on each octahedron as:

$$
\begin{aligned}
&H \,||\, [010] \\
&1A = 1B = 1C = 1D \\
&2A = 3B = 3C = 2D \\
&3A = 2B = 2C = 3D \\
&4A = 5B = 5C = 4D \\
&5A = 4B = 4C = 5D \\
&6A = 6B = 6C = 6D
\end{aligned}
\qquad (17)
$$

where the = sign is interpreted to mean the same angle between the V_K center molecular axis and the magnetic field. An additional simplification occurs since, for example, on the A-type octahedron 2A = 5A and 3A = 4A for orientations of the magnetic field parallel to [010].

For orientations of the magnetic field perpendicular to the tetrad axis and parallel to [100] (or [001] equivalently), the A-type octahedra

---

*The superscripts (±) serve no further explanatory purpose and will henceforth be deleted.

will be equivalent to the C-type octahedra, and the B-type octahedra will be equivalent to the D-type octahedra. In terms of the individual V_K centers, these equivalencies may be written:

$$H \parallel [100]$$

A = C	B = D
1A = 1C	1B = 1D
2A = 3C	2B = 3D
3A = 2C	3B = 2D
4A = 5C	4B = 5D
5A = 4C	5B = 4D
6A = 6C	6B = 6D

(18)

Thus it is necessary to consider only the A and B-type octahedra in the analysis of the ESR data for orientations of the magnetic field parallel to the [100] or [010] pseudocubic directions. The analysis of the ESR spectra was restricted to these two orientations, since any other orientations would have not only yielded extremely complicated spectra, but also would have supplied no significant additional information.

Consider now the structures of the octahedra (A and B) of interest in the analysis relative to their specific placements within the environment of the pseudocubes defined by the Na^+ ions (Figure 32). It is clear that not all of the V_K centers that can potentially be formed will have the same environment with respect to the Na^+ ions or nearest fluorine ions. However, the defects may be grouped together or subdivided into classes in which the environments are essentially the same. There will be six such classes as given in Table III. This class scheme was devised in anticipation of the expected result that the

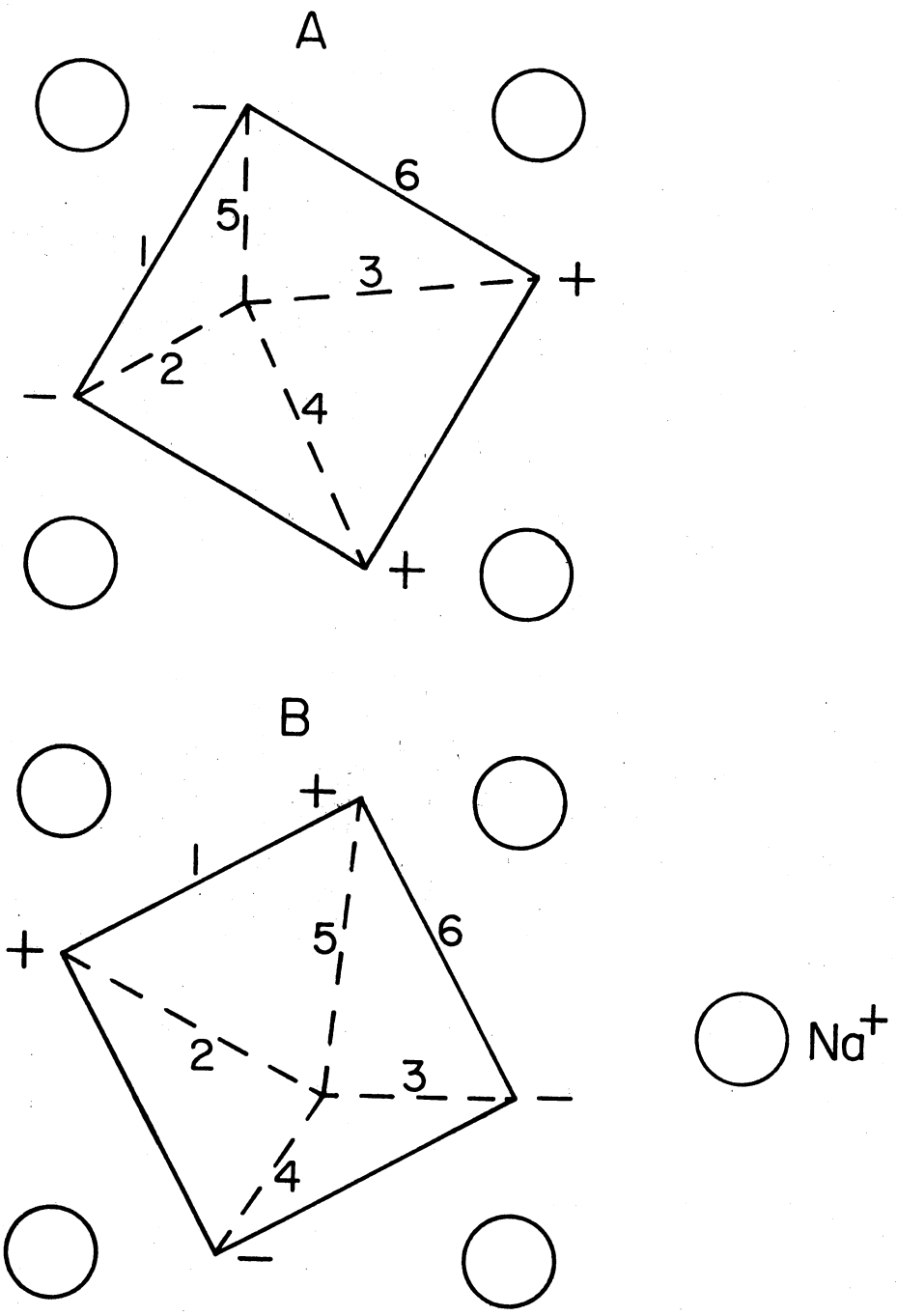

Figure 32. The Two Inequivalent Octahedra in $NaMgF_3$ Necessary for the Analysis of the [110]-Type V_K Center ESR Spectra

values of the spin Hamiltonian parameters would be slightly different for each class. Having made this division of V_K centers, the method will now be given by which the correspondence was made between the individual lines in the ESR spectra and the classified defects.

TABLE III

CLASSES OF [110]-TYPE V_K CENTERS IN $NaMgF_3$

Class	I	II	III	IV	V	VI
Elements	1A,1B	6A,6B	2A,3B	3A,2B	4A,5B	5A,4B

The spin Hamiltonian appropriate for the analysis of ESR spectra associated with self-trapped holes is given by (13)

$$\hat{H} = \beta' \vec{H} \cdot \overleftrightarrow{g} \cdot \vec{S} + \vec{I}_1 \cdot \overleftrightarrow{A}_1 \cdot \vec{S} + \vec{I}_2 \cdot \overleftrightarrow{A}_2 \cdot \vec{S} - g_{NF} \beta_N \vec{H} \cdot (\vec{I}_1 + \vec{I}_2) \qquad (19)$$

where

β' = Bohr magneton = $9.274096 \times 10^{-21} \frac{\text{erg}}{\text{Gauss}}$

$\vec{S}$ = the spin operator

$\overleftrightarrow{g}$ = the g tensor

$\vec{H}$ = the direction and magnitude of the applied magnetic field

$\overleftrightarrow{A}_i$ = the hyperfine tensor representing primarily dipole-dipole interaction between the unpaired spin and the two fluorine nuclei, as well as an isotropic Fermi contact interaction

$\overleftrightarrow{I}_i$ = the nuclear spin operator

$g_{NF}\beta_N$ = the gyromagnetic ratio pertinent to fluorine nuclei times Plank's constant h divided by $2\pi = 2.654144 \times 10^{-20}$ erg/Gauss

and

$|\overleftrightarrow{A}_1| = |\overleftrightarrow{A}_2|$ by symmetry.

The values of the spin Hamiltonian parameters obtained for the intrinsic V_K center in $KMgF_3$(20) are given in Table IV.

TABLE IV

SPIN HAMILTONIAN PARAMETERS FOR THE INTRINSIC SELF-TRAPPED HOLE IN $KMgF_3$

$g_x = 2.024$	$A_x = 160$ MHz
$g_y = 2.018$	$A_y = 160$ MHz
$g_z = 2.0024$	$A_z = 2479$ MHz
(Bent Bond) = 7^o	

If one initially assumes that values of the spin Hamiltonian parameters for the [110]-type V_K centers in $NaMgF_3$ are equal to those for the intrinsic self-trapped holes in $KMgF_3$, then the ESR spectra arising from the [110]-type defects may be roughly predicted if one uses the estimated room temperature tilt angles of $\omega = 8.88^o$ and $\phi = 12.95^o$.

The results of this initial calculation are given in Table V for

TABLE V

PREDICTED LINE POSITIONS (IN GAUSS) FOR THE [110]-TYPE V_K CENTERS IN $NaMgF_3$ USING $KMgF_3$ V_K CENTER SPIN HAMILTONIAN PARAMETERS

	H || [100]			
V_K	1	2	3	4
1A	2663.47	3167.86	3335.41	3690.36
2A	2683.60	3163.59	3337.02	3659.62
3A	2511.86	3202.34	3322.93	3937.68
4A	2938.45	3236.83	3250.75	3351.72
5A	3091.34	3144.20	3235.44	3287.08
6A	2530.69	3197.79	3324.49	3904.69
1B	2517.34	3200.36	3323.93	3927.86
2B	2532.39	3196.73	3325.17	3901.57
3B	2657.76	3168.42	3335.46	3699.01
4B	2951.40	3234.70	3250.24	3339.75
5B	3095.47	3140.48	3236.71	3285.53
6B	2673.77	3164.99	3336.75	3674.34
	H || [010]			
1A,1B	3105.91	3130.13	3235.28	3286.44
2A,3B	2521.63	3199.79	3323.89	3920.44
3A,2B	2672.04	3165.85	3336.23	3677.13
4A,5B	2672.02	3165.85	3336.23	3677.16
5A,4B	2521.64	3199.79	3323.89	3920.41
6A,6B	2940.56	3237.19	3250.06	3350.61

orientations of the magnetic field parallel to [010] and [100]. If one focuses attention on the farthest split lines associated with each V_K center, i.e., neglecting columns 2 and 3, the outer lines in the ESR spectra (Table II, lines 2, 3, 4, 11, 12, 13, 15, 16, 17, 18, 19, 23, 24, 25, 26, 27 and 28) may be roughly matched to the predicted line positions. Consider first lines 2, 3, 4, 11, 12, and 13 in the spectrum obtained (Figure 25) for orientations of the magnetic field parallel to the tetrad axis ([010]). The following correspondence can be made:

(H || [010])

V_K	ESR Lines
1A,1B	(indeterminate)
2A,3B	2,13
3A,2B	3,12
4A,5B	3,12
5A,4B	2,13
6A,6B	4,11

(20)

Since the 1A and 1B V_K center molecular axes remain perpendicular to the magnetic field for this orientation, they will give rise to lines in the center portion of the spectrum and therefore no definite initial correspondence could be made. Next, consider lines 15, 16, 17, 18, 19, 23, 24, 25, 26, 27, and 28 in the spectrum obtained for orientations of the magnetic field perpendicular to the tetrad axis (Figure 26). The correspondence here is not as obvious as for the previous case, but a close comparison of Table V with the measured field values will yield the following initial assignments:

(H || [100])

V_K	ESR Lines
1A	17,26
1B	15,28
2A	18,25
2B	16,27
3A	15,28
3B	17,26
4A	19,24
4B	19,24
5A	23
5B	23
6A	16,27
6B	18,25

(21)

Thus using these correspondences, the outer lines in the ESR spectra for orientations of the applied magnetic field parallel and perpendicular to the tetrad axis were fitted to exactly by varying the spin Hamiltonian parameters and the two tilt angles. This fitting was performed for each V_K center class separately since the values of the adjusted parameters were expected to vary from class to class. The results of these calculations are given in Table VI. In order to insure that sufficient information was provided in the fitting calculations to properly determine the parameters, the number of parameters was effectively reduced from eight to six by setting the x and y components of the $\vec{g}$ and $\vec{A}$ tensors equal to each other within the iteration scheme used in the calculations. This was a reasonable assumption since these components are typically quite close in value (65). In particular for class I, these parameters (g_x,g_y,A_x,A_y) were held constant since only four lines were fitted to. It is immediately discernable from Table VI that there is generally poor agreement between results obtained for the different classes. Furthermore, the values obtained for some parameters border on being unphysical, i.e., they are vastly different from

TABLE VI

INITIAL CALCULATION OF SPIN HAMILTONIAN PARAMETERS FOR EACH OF THE SIX CLASSES OF [110]-TYPE V_K CENTERS IN $NaMgF_3$

V_K Center Class		Lines Fitted to	$g_x = g_y$	g_z	$A_x = A_y$ (MHz)	A_z (MHz)	ω	ϕ
I:	1A 1B	17,26 15,28	2.0250 (Not Varied)	2.0000	100 (Not Varied)	2557	14.35°	16.85°
II:	6A 6B	4,11,16,27 4,11,18,25	2.0250	2.0076	110	2499	15.6°	18.45°
III:	2A 3B	2,13,18,25 2,13,17,26	2.0241	2.0047	97	2534	6.85°	22.45°
IV:	3A 2B	3,12,15,28 3,12,16,27	2.0250	2.0040	135	2532	10.55	20.05°
V:	4A 5B	3,12,19,24 3,12,23	2.0160	2.0200	70	2572	9.15°	20.85°
VI:	5A 4B	2,13,23 2,13,19,24	2.0140	2.0030	~0	2602	14.35°	16.85°

the values obtained for other V_K centers (65). For example, the value of g_z for class V is significantly larger than that found for any other fluorine molecular ions. Note also that the values of the tetrad rotations (ω) calculated for classes III, IV, and V are approximately the same or less than the value of this angle calculated from room temperature lattice parameters (8.88^o). However, in consideration of the fact that a continuous increase in the tilting of the octahedra occurs simultaneously with the decreasing size of the pseudocubic cell (Figure 6), a larger value for the 77 K tetrad rotation was expected. Finally, it must be noted that the simplicity of the ESR spectra made it necessary to assume a number of fortuitous degeneracies. For example, the 4A and 4B V_K centers are members of different classes (V and VI, respectively) and are therefore assumed to have slightly different spin Hamiltonian parameters, and yet both are assumed to give rise to lines 19 and 24 in the [100] ESR spectrum (Figure 26). Such degeneracies are expected to occur rather infrequently, and the number required to explain the spectrum was, therefore, unsatisfying. These results posed a dilemna which had to be resolved before confidence in the calculated parameters could be realized.

The first step in the resolution of the cited inconsistencies involved a reevaluation of the importance of the difference in the relative intensities of the lines in the ESR spectra. The constructed correspondence between the specific V_K centers and their line positions (Eq. 20) in the ESR spectrum indicated that the intensities of lines 2, 3, 12, and 13 should be identical and individually twice as intense as lines 4 and 11. As can be observed (Figure 25) this is not the case. Furthermore, lines 3, 5, 7 and 12 are broadened with linewidths ranging

from ~16 gauss to ~20 gauss, whereas the other lines in the spectrum are sharper with linewidths of less than ~15 gauss. Lines 17 and 26 in the [100] ESR spectrum (Figure 26) are also broadened and occur at nearly the same positions of magnetic field as lines 3 and 12 (Table II). The line broadening was not an orientation effect since the spectra reproduced exactly for a number of different measurements. The most logical explanation consistent with these facts was to assume that the broadened lines were not part of the [110]-type V_K center ESR spectra, but belong to other fluorine molecular ions which are formed as a consequence of the lower symmetry crystal structure. No model has been developed for these centers in this study. The loss of the broadened lines (3, 5, 7, 12, 17, and 26) for use in interpreting the [110]-type V_K center ESR spectra imposed the requirement that certain V_K center orientations were missing, since the only alternative would involve assuming an increase in the "accidental" degeneracies. The logic behind the assignments of the missing orientations will now be given.

For classes IV and V (see Table VI), lines 3 and 12 in the [010] ESR spectrum were the only possible choices for the assignments of the transitions associated with the 3A, 2B, 4A, and 5B V_K centers (compare Tables II and V). Thus if lines 3 and 12 are not part of the [110]-type V_K center ESR spectrum, then classes IV and V must be missing, i.e., the 3A, 2B, 4A, and 5B V_K centers are not present. If lines 17 and 26 in the [100] ESR spectrum are not associated with [110]-type V_K centers, then it would initially appear that classes I and III are missing. However, lines 15, 26, and 28 must be accounted for and therefore both classes cannot be absent. In fact, since lines 15 and 28 are associated with class I only, then this class must be present, and the

assignment of lines 17 and 26 to the 1A V_K must be modified. This can be done if one observes that this assignment was not as absolute as for the previously considered cases, and assignments of lines 18 and 25 to the 1A V_K are equally valid. Further justification for the choice of class I over class III may be obtained through a reexamination of Figure 25 and noting that lines 8 and 9 arise from V_K centers with their molecular axes ~ perpendicular to the applied field. The 1A and 1B V_K centers are the only possible defects which will exhibit this behaviour since, as can be seen in Figure 31, only the tetrad rotation will affect these V_K centers relative to orientations of the magnetic field parallel to [010] or [100].

Thus it is concluded that only three of the possible six classes of [110]-type V_K centers are present in $NaMgF_3$ crystals following electron irradiation at 77 K. Even though only half of the V_K center orientations are present, all the outer lines in the spectra may be accounted for and only one degeneracy is assumed, namely the assignment of lines 18 and 25 to both 1A and 6B V_K centers. The missing orientations may be explained by considering the fact that the Na^+ ions are shifted in the distorted low temperature crystal structure from their high symmetry positions in the cubic structure ($\geq$ ~ 900°C). These small relative displacements may be sufficient to make some V_K center orientations preferentially unstable due to the repulsion of the effective positive charge of the self-trapped holes by the shifted Na^+ ions. Thus when a [110]-type V_K center is formed at 77 K in one of the less stable orientations, it immediately makes a single jump to an orientation of lower energy on the octahedron. This reorientation must be limited to the octahedron on which the V_K center is initially formed since the relative

intensities of the ESR lines for the [110] and [100]-type V_K centers are always the same. Similar thermal reorientation behaviour has been observed to occur at ~120 K for V_K centers in $RbCaF_3$ (66). That compound has a tetragonal crystal structure at low temperatures, and the intrinsic self-trapped holes are divided into two classes. The ESR spectra associated with the intrinsic V_K centers in this latter material for orientations of the magnetic field parallel and perpendicular to the unique (tetrad) axis are shown in Figures 33 and 34.

The fact that only three classes of [110]-type V_K centers were present in crystals of $NaMgF_3$ indicated that certain unknown distortions accompanying the formation of self-trapped holes in this material might exist. This may have been reflected in the result that realistic spin Hamiltonian parameters could not be calculated, however, the tilt angles calculated for the existing classes were not unreasonable (Table VI). It was further recognized that the fitting calculations could not independently distinguish between small changes of A_z, ω, and ϕ.

Thus, since the spin Hamiltonian parameters were not expected to depart significantly from those obtained for V_K centers in $KMgF_3$, then these values (Table IV) were used in a final set of fitting calculations with only the tilt angles being allowed to vary. The results of these calculations are given in Table VII. The tilt angles for classes II and VI which gave the best prediction of the experimental line positions based on the preceding assumptions were determined first, and an average value for the diad rotation of 18.5° was obtained. Since the class I V_K centers were expected to be insensitive to the value of ϕ, then the average value (18.5°) was assumed to be correct for this class and only the tetrad rotation was allowed to vary. The tilt angles calculated in

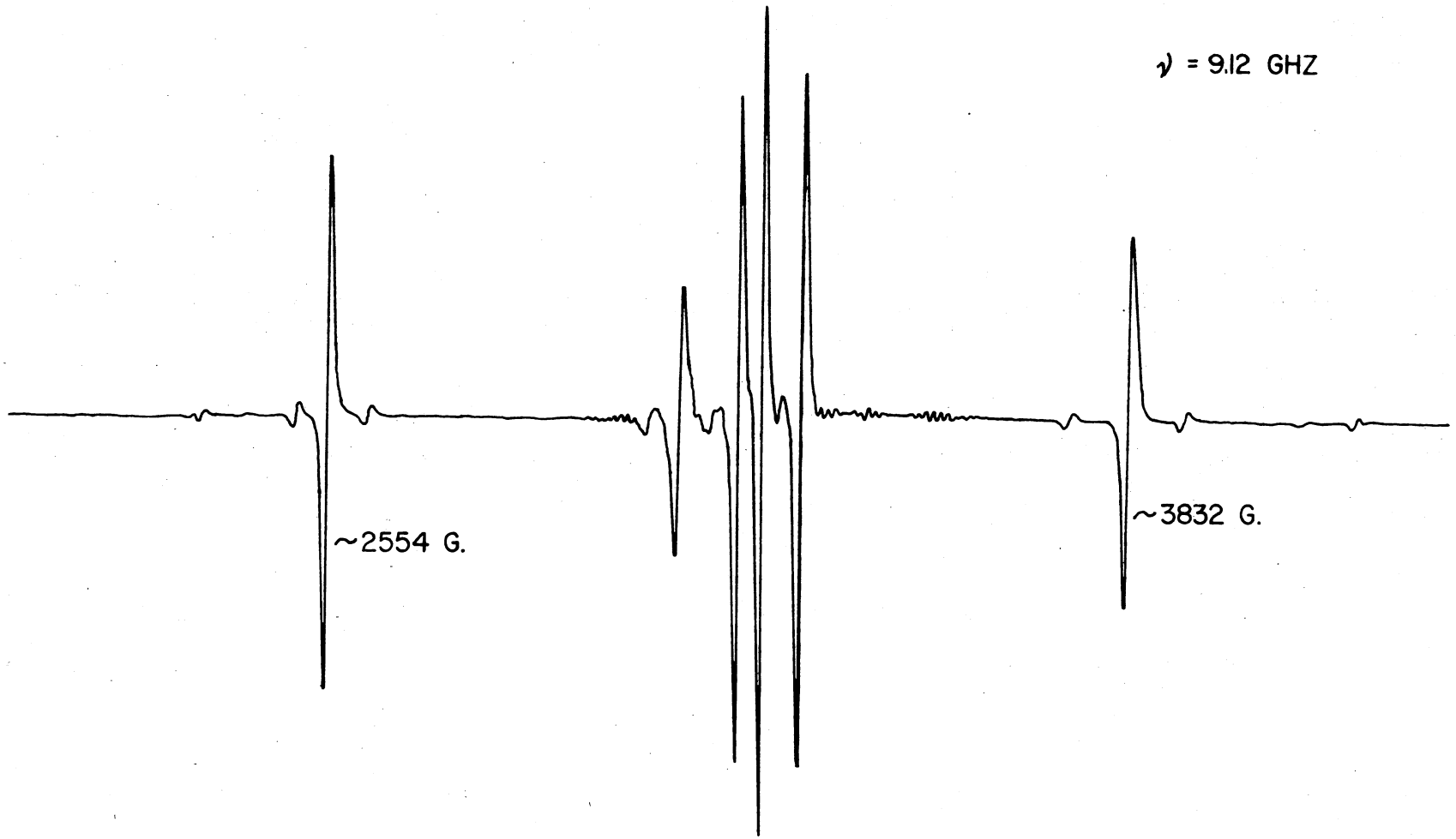

Figure 33. The ESR Spectrum for V_K Centers in $RbCaF_3$ for H Parallel to the Unique Axis

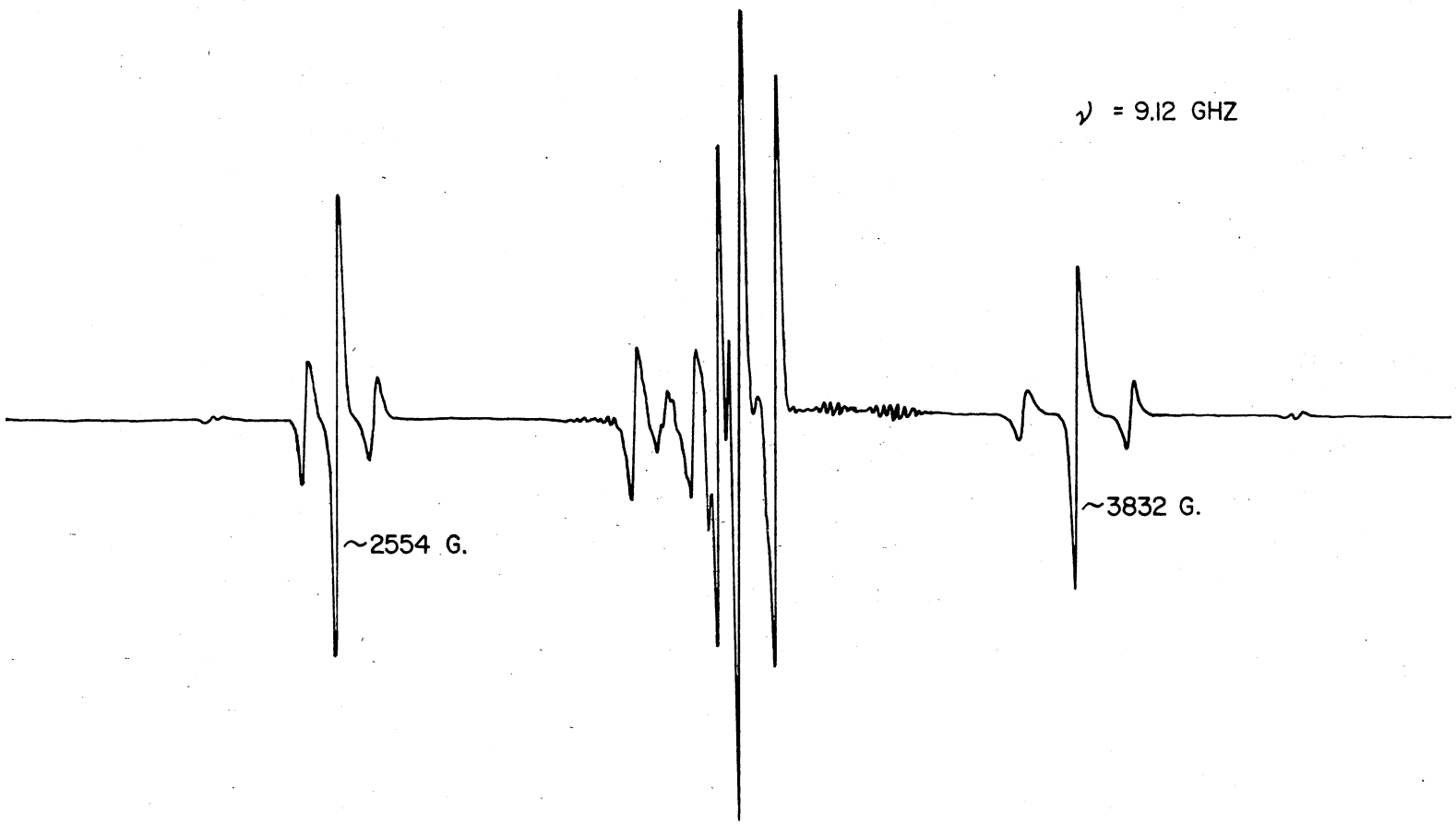

Figure 34. The ESR Spectrum for V_K Centers in $RbCaF_3$ for H Perpendicular to the Unique Axis

TABLE VII

CALCULATION OF THE TILT ANGLES FOR THE OCTAHEDRA IN $NaMgF_3$ BASED ON AN ANALYSIS OF THE V_K CENTER ESR SPECTRA

V_K Center Class		Lines Fit to	ω (Effective)	ϕ (Effective)
I:	1A 1B	18,25 15,28	17.1°	18.5°
II:	6A 6B	4,11,16,27 4,11,18,25	15.5°	18.55°
VI:	5A 4B	2,13,23 2,13,19,24	15.3°	18.45°
		Crystalline Tilt Angles:	$\omega = 16.0^\circ \pm 3^\circ$	$\phi = 18.5^\circ \pm 3^\circ$

this way were "effective" values since they also contained the inherent influence of distortions of the V_K center molecular axes away from the true lines of fluorine ions (i.e. [110]-type directions) within the octahedra. Thus the average values of these calculated angles were assumed to be representative of the true crystalline tilt angles, and liberal tolerances ($\pm 3^{\circ}$) were placed on these values to account for the effect of the local distortion created by the V_K center itself. Using the tilt angles for each V_K center class separately, the line positions were predicted and are given in Table II (Chapter III). It can be seen that the agreement with the experimental field values is far from perfect but for a given resonance is generally within a line-width (~15 gauss).

At the heart of the calculations used in the analysis of the [110]-type V_K center ESR spectra is the spin Hamiltonian (Eq. 19) and the diagonalization of its matrix representation. There were five coordinate systems necessary for a complete treatment. These are defined as:

x_g, y_g, z_g: g tensor principal axis system

x_1, y_1, z_1: nucleus 1 hyperfine principal axis system

x_2, y_2, z_2: nucleus 2 hyperfine principal axis system

x_u, y_u, z_u: "untilted" crystal axes

x, y, z : magnetic field system

Rewriting the Hamiltonian in the various coordinate systems:

$$
\begin{aligned}
H = \beta'(&H_{x_g} g_x S_{x_g} + H_{y_g} g_y S_{y_g} + H_{z_g} g_z S_{z_g}) \\
&+ I^1_{x_1} A_x S_{x_1} + I^1_{y_1} A_y S_{y_1} + I^1_{z_1} A_z S_{z_1} \\
&+ I^2_{x_2} A_x S_{x_2} + I^2_{y_2} A_y S_{y_2} + I^2_{z_2} A_z S_{z_2} \\
&- g_{NF}\beta_N H(I^1_z + I^2_z)
\end{aligned}
\tag{22}
$$

where the superscripts denote nuclei 1 and 2. It was then necessary to reexpress the Hamiltonian in the magnetic field system. This was accomplished through the use of the five different transformation matrices defined by:

$$
BB = \begin{bmatrix} \cos\beta & 0 & \sin\beta \\ 0 & 1 & 0 \\ -\sin\beta & 0 & \cos\beta \end{bmatrix} \tag{23}
$$

which transforms the nucleus 1 hyperfine system into the g tensor system ($\beta \equiv$ bent bond),

$$
BBB = \begin{bmatrix} \cos\beta & 0 & -\sin\beta \\ 0 & 1 & 0 \\ \sin\beta & 0 & \cos\beta \end{bmatrix} \tag{24}
$$

which transforms the nucleus 2 hyperfine system into the g tensor system,

$$G = \begin{bmatrix} 1 & 0 & 0 \\ 0 & 1 & 0 \\ 0 & 0 & 1 \end{bmatrix}, \begin{bmatrix} 1/2 & \sqrt{2}/2 & -1/2 \\ -\sqrt{2}/2 & 0 & -\sqrt{2}/2 \\ -1/2 & \sqrt{2}/2 & 1/2 \end{bmatrix}, \begin{bmatrix} -1/2 & \sqrt{2}/2 & 1/2 \\ \sqrt{2}/2 & 0 & \sqrt{2}/2 \\ 1/2 & \sqrt{2}/2 & -1/2 \end{bmatrix},$$

$$\begin{bmatrix} -1/2 & \sqrt{2}/2 & -1/2 \\ -\sqrt{2}/2 & 0 & \sqrt{2}/2 \\ 1/2 & \sqrt{2}/2 & 1/2 \end{bmatrix}, \begin{bmatrix} 1/2 & \sqrt{2}/2 & 1/2 \\ \sqrt{2}/2 & 0 & -\sqrt{2}/2 \\ -1/2 & \sqrt{2}/2 & -1/2 \end{bmatrix}, \begin{bmatrix} 0 & 0 & 1 \\ 0 & -1 & 0 \\ 1 & 0 & 0 \end{bmatrix} \quad (25)$$

which transforms the g tensor system for V_K centers 1 through 6 (see Figure 31) into the g tensor system of V_K occupying position 1 (V_K1),

$$T = \begin{bmatrix} \cos\phi\cos\omega & \sin\phi & \cos\phi\sin\omega \\ -\sin\phi\cos\omega & \cos\phi & -\sin\phi\sin\omega \\ -\sin\omega & 0 & \cos\omega \end{bmatrix} \quad (26)$$

which transforms the g tensor system of V_K 1 into the "untilted" crystal axes (ω = tetrad rotation, ϕ = diad rotation), and

$$R = \begin{bmatrix} \cos\phi & \sin\theta\sin\alpha & -\sin\theta\cos\alpha \\ 0 & \cos\alpha & \sin\alpha \\ \sin\theta & -\cos\theta\sin\alpha & \cos\theta\cos\alpha \end{bmatrix} \quad (27)$$

which transforms the "untilted" axis system into the magnetic field system for an arbitrary orientation of H. The complete transformation was thus of the form:

$$(G)(T)(R) = GTR$$

$$(BB)(G)(T)(R) = BBGTR \qquad (28)$$

or

$$(BBB)(G)(T)(R) = BBBGTR$$

For example,

$$I^1_{x_1} = BBGTR(1,1)I^1_x + BBGTR(1,2)I^1_y + BBGTR(1,3)I^1_z$$

After the Hamiltonian had been reexpressed in the magnetic field system, it was then necessary to introduce raising and lowering operators given by:

$$S_x = (S_+ + S_-)/2 \qquad I_x = (I_+ + I_-)/2$$
$$S_y = (S_+ - S_-)/2i \qquad I_y = 1/2i(I_+ - I_-) \qquad (29)$$

The matrix representation of the spin Hamiltonian was then constructed using the eight basis vectors defined by:

$$|m_S m_{I_1} m_{I_2}>$$

where

$m_S = \pm\frac{1}{2}$ ≡ spin magnetic quantum no's.

$m_{I_1} = \pm\frac{1}{2}$, $m_{I_2} = \pm\frac{1}{2}$ ≡ nuclear magnetic quantum no's. for nuclei 1 and 2

which yields an 8 x 8 matrix of the form:

$$
\begin{bmatrix}
A(1,1) & & & & & & & \\
A(2,1) & A(2,2) & & & & & & \\
A(3,1) & 0 & A(3,3) & & & & & \\
0 & A(4,2) & A(4,3) & A(4,4) & & & & \\
A(5,1) & A(5,2) & A(5,3) & 0 & A(5,5) & & & \\
A(6,1) & A(6,2) & 0 & A(6,4) & A(6,5) & A(6,6) & & \\
A(7,1) & 0 & A(7,3) & A(7,4) & A(7,5) & 0 & A(7,7) & \\
A(8,1) & A(8,2) & A(8,3) & A(8,4) & 0 & A(8,6) & A(8,7) & A(8,8)
\end{bmatrix}
$$

The eigenvalues of this hermitian matrix were calculated using the diagonalizing subroutines (Appendix E) since the matrix is hermitian only the lower half was needed in the calculations.

The eight energy eigenvalues obtained from this diagonalization could then be used to determine the magnetic field positions associated with the four transitions for each V_K center in the ESR spectra. One program (Appendix D) was used to predict the line positions assuming constant values of the eight parameters ($g_x, g_y, g_z, A_x, A_y, A_z, \omega$, and ϕ). In another "fitting" program (Appendix C), each parameter was adjusted independently until a "best" fit to measured field values, comprising part of the program input, was obtained.

[100]-Type V_K Centers

As described in Chapter III, when crystals of $NaMgF_3$ were electron irradiated at 77 K and then warmed to room temperature, a subsequent ESR measurement revealed that a spectrum remained which possessed [100]-type symmetry, i.e., the maximum splitting of the lines occurred for orientations of the static magnetic field perpendicular to a pseudo-

cubic face. For the single domain crystal, the presence of only three resonances in the spectrum (Figure 24) with an intensity ratio of approximately 1:2:1 was indicative of an interaction with two spin ½ nuclei. Furthermore, the roughly measured hyperfine splitting of ~2600 MHz was typical for fluorine molecular ions. These facts suggested that the defect giving rise to this spectrum was a V_K center with its molecular axis parallel to a pseudocubic direction. The simple three-line pattern indicated that there was only one orientation of this V_K center within the crystal. This self-trapped hole has been labeled a [100]-type V_K center because of its observed symmetry.

A careful study of the assumed 77 K crystal structure for $NaMgF_3$ resulted in the conclusion that only one possible model could be constructed for this defect consistent with the crystal symmetry and the restriction that a unique orientation of this center existed in the crystal. This structural model is depicted in Figure 35 which shows two octahedra for <010> pseudocubic directions. This type of V_K center is capable of forming as a result of the diad tilts (ϕ) which bring the fluorine ions, specified in the figure, into close enough proximity for the V_K centers to be formed. Note that since the two octahedra have the same tetrad rotation (ω), then the fluorines that could potentially form these V_K centers will still be aligned parallel to an [010] pseudocubic direction. No other relatively simple defect model could be envisioned which would yield only one possible orientation for the V_K center molecular axes in the crystal.

The distance between the fluorines prior to formation of the [100]-type V_K center may be calculated from the value obtained for the diad rotation (18.5°) in the [110]-type V_K center analysis. Upon examining

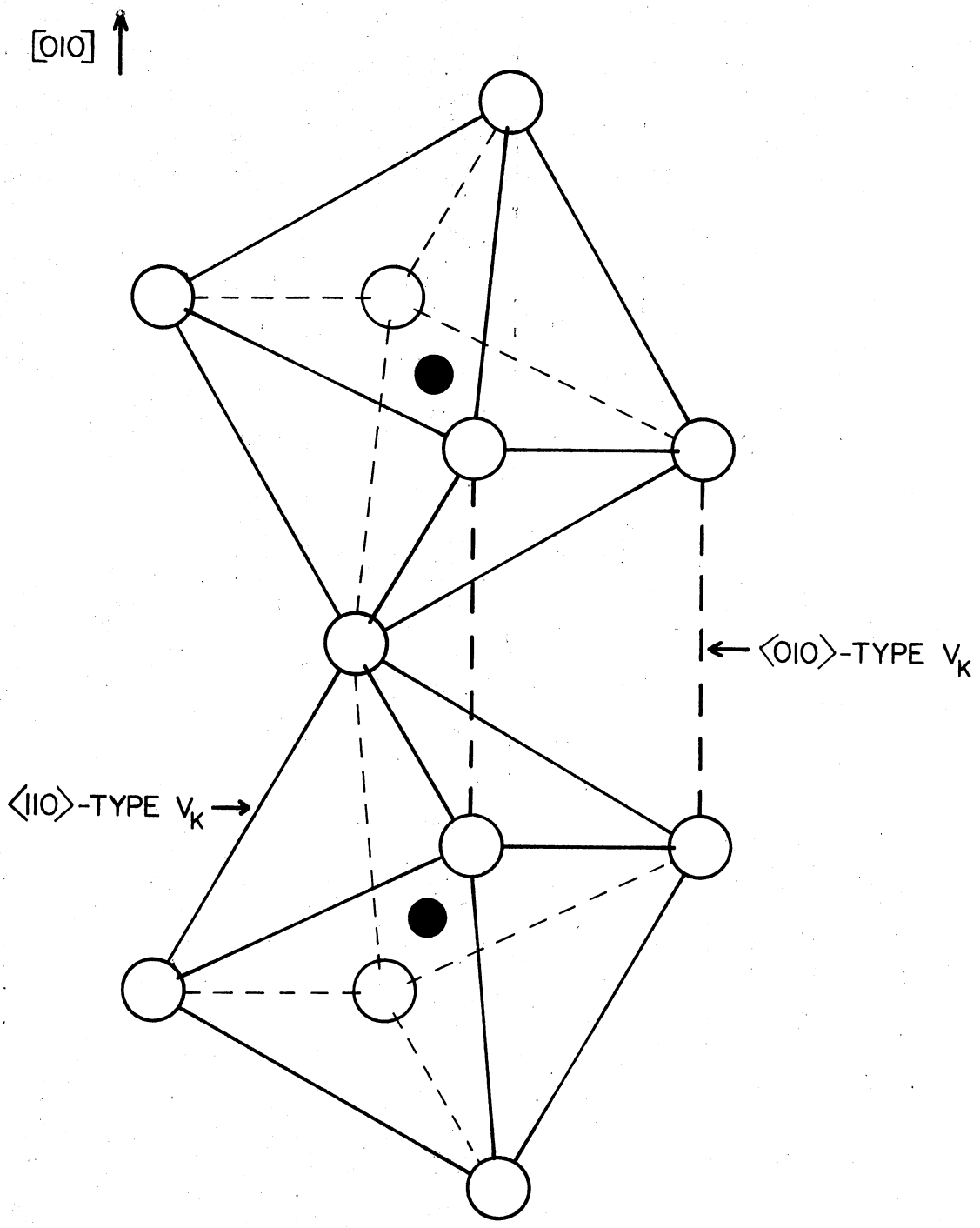

Figure 35. Model for the [100]-Type V_K Center in $NaMgF_3$

the geometry of the tilted octahedra in the plane perpendicular to the axis of the diad rotation, the following equation may be arrived at which relates the diad rotation (ϕ) to the intra-octahedral fluorine-fluorine separation (ℓ) and the distance (s) between the two inter-octahedral fluorine ions potentially giving rise to the [100]-type V_K center:

$$\sin(45^\circ - \phi) = \frac{s}{2\ell} \tag{30}$$

and for $\phi = 18.5^\circ$ this gives $s = .892\ell$. Thus the fluorine-fluorine separation for [100]-type V_K centers is comparable to and in fact slightly less than that for [110]-type V_K centers.

This simple calculation would initially appear to be inconsistent with the experimental result that the [100]-type V_K center has a greater thermal stability than the [110]-type V_K center, since larger ionic separations are expected to provide an increase in the amount of lattice distortion available and therefore allow a deeper self-trapping of the hole. However, since the analysis of the [110]-type V_K center ESR spectra indicated that some distortions arising from the shifted Na^+ ions and the presence of the self-trapped hole itself were present, then it is reasonable to assume that similar effects may contribute to increasing the thermal stability of the [100]-type V_K centers.

The values of the parameters A_z and g_z associated with this defect were calculated directly from the experimental line positions (Table II) and were determined to be:

$$A_z = 2602 \text{ MHz} \qquad g_z = 2.0034 \tag{31}$$

No determination of the other components of the hyperfine and $\overleftrightarrow{g}$ tensors was attempted, since this would have required a measurement of the magnetic field positions associated with the isolated spectrum for an exact alignment of the applied magnetic field parallel to [100]. Such a measurement was not possible because, as argued in Chapter III, exact alignments of the magnetic field for the isolated spectra could not be achieved. The values of A_z and g_z were determined solely from the measurement of lines 1 and 14 in the spectrum obtained following direct electron irradiation at 77 K (Figure 25).

It is interesting to speculate that the [100]-type V_K center may be preferred over the [110]-type V_K center in regard to the production of defects by way of the Pooley-Hersh (excitonic) mechanism (Chapter I). This conjecture arises from the fact that the lines of fluorine ions are uniform in the direction of alignment of the [100]-type V_K center molecular axes but are staggered in the direction of alignment of the [110]-type V_K center molecular axes. Thus, after formation of the self-trapped excitons, the subsequent dissociation and ionic replacement sequence may proceed more efficiently for those $X_2^{=*}$ molecular ions formed at [100]-type V_K center sites. Verification of this speculation could possibly be realized by way of an experiment similar to that performed by Keller and Patten (Chapter I) once the interstitial molecular ions in $NaMgF_3$ are characterized.

Finally, it should be pointed out that the structure of the [100]-type V_K center has to our knowledge no precedent among the self-trapped holes studied in various halide materials in the sense that it is formed as a consequence of the particular tilting of the octahedra in $NaMgF_3$. This suggests that similar centers may also be found to occur in other

compounds with tilted octahedra such as the low temperature ($\leq 25^{o}C$) form of $KMgCl_3$ (67).

Thermoluminescence

Following electron irradiation of $NaMgF_3$ at 77 K, thermoluminescence was found to occur continuously from 77 K to 600 K and was characterized by a number of well defined glow peaks (Figure 28). The strongest glow peak occurred at ~133 K and was believed to be associated with the thermal decay (120 ± 10 K) of the [110]-type V_K centers. This interpretation is supported by the results obtained for $KMgF_3$ in which a relatively sharp and intense glow peak was found to occur at approximately the same temperature as that corresponding to the thermal decay of the intrinsic V_K centers in that compound. A specific model for the origin of the luminescence involves assuming that electron-hole recombination occurs at an impurity ion which in the process changes valence state. The recombination energy is then transferred to the impurity ion which subsequently deexcites through the emission of a photon, thus yielding the luminescence. The luminescence will therefore be characteristic of the impurity ion in the newly formed valence state. This model has been found to agree well with results obtained in a comprehensive study of TSL in rare earth doped CaF_2 obtained following irradiation with x-rays at low temperatures (68).

ESR measurements taken after samples had been warmed through the first TSL glow peak and then subsequently recooled to 77 K revealed the presence of weak spectra associated with fluorine molecular ions other than [100]-type V_K centers. These centers were assumed to be perturbed defects and were not analyzed in this study. However, the thermal decay

of these centers may have been responsible for the weaker glow peaks (212 K, 246 K, and 286 K) in the TSL data since only [100]-type V_K centers were observed with ESR to be present after samples had been warmed completely to room temperature. The thermal decay of the [100]-type V_K center cannot be unambiguously correlated with a TSL glow peak due to the presence of several peaks in the temperature range of thermal instability for this center.

The TSL generated above room temperature may originate in interstitial-F center recombination near an impurity. This explanation differs from the electron-hole recombination model proposed for the low temperature TSL in that it does not specifically require any changes in impurity valence states. Such a model has been suggested previously (69) for the high temperature TSL observed in $KMgF_3$ following electron or γ irradiation at room temperature.

No detailed spectroscopic analysis of the TSL emission was performed, but visual observation of the emission revealed a predominantly blue luminescence for the TSL emission in all temperature ranges. This emission is most likely associated with a transition metal ion such as V^{2+}.

CHAPTER V

SUMMARY

This study has resulted in the ESR identification and characterization of several defects produced by irradiation in crystals of $KMgF_3$:Mn and $NaMgF_3$. The production and thermal decay of these defects have been correlated with complementary thermoluminescence measurements.

In $KMgF_3$:Mn, the ESR identification of the ionized form of the Mn^{2+}-F center pair (Mn^{2+}-fluorine vacancy center) has been made, and a defect model has been proposed based on the analysis. This study has provided independent verification that the increase in oscillator strengths of the optical transitions for the defect associated Mn^{2+} ions in $KMgF_3$ is a result of exchange interaction rather than a change in site symmetry. A list of further radiation damage studies related to those performed for $KMgF_3$:Mn which would be useful might include:

(1) An ESR investigation of the Mn^{2+}-F center pairs directly. Such a study may provide more information concerning the exchange interactions between the two defects.

(2) An ENDOR study of the Mn^{2+}-fluorine vacancy center may provide a more detailed and accurate model for this defect.

(3) A more complete study of the TSL generated at low temperatures (<295 K) following room temperature electron irradiation and 77 K UV bleaching is in order. In particular, the correlation between ESR results obtained for the pure samples following this same irradiation

procedure should be performed since a brief ESR investigation indicated that fluorine molecular ions grew in under such irradiation treatments.

(4) The study of Mn^{2+}-F center type defects may be extended to such halide compounds as MgF_2 and $RbMgF_3$ and the same series of experiments performed.

(5) A determination of the concentration of Mn^{2+}-F center pairs in the crystal would be useful in determining if a preferential production of F centers next to Mn^{2+} occurs.

(6) A more complete study of the unknown ESR spectrum that remained after electron irradiating at 77 K and subsequently warming to room temperature (Chapter III) may provide more information about the electron traps in this compound.

A study of $NaMgF_3$ electron irradiated at 77 K revealed the existence of two distinct and yet both intrinsic self-trapped holes in this material. The two fluorines sharing the hole were found to be on the same octahedron for one V_K center ([110]-type V_K) and on adjacent octahedra for the other V_K center ([100]-type V_K). The thermal decay of the [110]-type V_K center was found to be accompanied by both a strong thermoluminescence glow peak and a conversion into [100]-type V_K centers. The analysis of the ESR spectra associated with the [110]-type V_K center yielded values for previously undetermined 77 K octahedral tilts of 16.0° about a tetrad axis and 18.5° about a diad axis. All the low temperature TSL in $NaMgF_3$ is associated with a hole release process since the [100]-type V_K center remains stable throughout the low temperature luminescence range (77 K to room temperature).

The following topics are suggested for future study in $NaMgF_3$:

(1) An ESR investigation of fluorine molecular ions which are pro-

duced by electron irradiation at room temperature followed by a 77 K uv bleach. These defects are most likely interstitial centers.

(2) An ESR investigation of $NaMgF_3$ electron irradiated at ~4.2K should have all classes of [110]-type V_K centers formed. This would thus be a test of the thermal reorientation behaviour assumed in the analysis.

(3) More precise measurements of the thermal decay temperatures for the intrinsic self-trapped holes are needed to establish the relationship with the TSL more precisely.

(4) The optical absorption bands associated with the intrinsic radiation induced defects in $NaMgF_3$ are in need of absolute identification.

SELECTED BIBLIOGRAPHY

1. Holmes-Siedle, A., Nature 251, 191 (1974).

2. Schneider, I., Appl. Opt. 6, 2197 (1967).

3. Borg, J., J. Mat. Sci. 8, 484 (1973).

4. Schulman, J. H. and W. D. Compton, Color Centers in Solids (Pergamon, N. Y., 1971).

5. Fowler, W. B., The Physics of Color Centers (Academic Press, N. Y., 1968).

6. Crawford, J. H., and L. M. Slifkin, eds. Point Defects in Solids, Volume 1: New York: Plenum Press, 1972. Chapter 4 by E. Sonder and W. A. Sibley.

7. Hayes, W. and J. W. Twidwell, J. Chem. Phys. 35, 1521 (1961).

8. McClure, D. S. and Z. J. Kiss, J. Chem. Phys. 39, 3251 (1963).

9. Sabisky, E. S., Phys. Rev. 141, 352 (1966).

10. Davidge, R. W., J. Mat. Sci. 2, 339 (1967).

11. Delbecq, C. J., W. Hayes, M. C. M. O'Brien, and P. H. Yuster, Proc. Roy. Soc. 271A, 243 (1963).

12. Delbecq, C. J., A. K. Ghosh, and P. H. Yuster, Phys. Rev. 151, 599 (1966).

13. Castner, T. G., and W. Känzig, J. Phys. Chem. Solids 3, 178 (1957).

14. Delbecq, C. J., W. Hayes, and P. H. Yuster, Phys. Rev. 121, 1043 (1961).

15. Jones, G. D., Phys. Rev. 150, 539 (1966).

16. Murray, R. B., and F. J. Keller, Phys. Rev. 153, 993 (1967).

17. Patten, F. W., and M. J. Marrone, Phys. Rev. 142, 513 (1966).

18. Hayes, W., and J. W. Twidell, Proc. Phys. Soc. 79, 1295 (1962).

19. Beaumont, J. H., W. Hayes, D. L. Kirk, and G. P. Summers, Proc. Roy. Soc. London A315, 69 (1970).

20. Hall, T. P. P., Brit. J. Appl. Phys. 17, 1011 (1966).

21. Norman, C. D. and L. E. Halliburton (private communication).

22. Hutchison, C. A., Phys. Rev. 75, 1769 (1949).

23. Feher, G., Phys. Rev. 114, 1219 (1959).

24. Känzig, W. and T. O. Woodruff, J. Phys. Chem. Solids 9, 70 (1958).

25. Rose, B. H., J. E. Rhoads, and L. E. Halliburton (accepted by Phys. Rev. B).

26. Crawford, J. H. and L. M. Slifkin, eds. Point Defects in Solids, Volume 1: New York: Plenum Press, 1972. Chapter 5 by C. C. Klick.

27. Crawford, J. H. and L. M. Slifkin, eds. Point Defects in Solids, Volume 1: New York: Plenum Press, 1972. Chapter 6, by M. N. Kabler.

28. Seitz, F., Phys. Rev. 79, 529 (1950).

29. Balzer, R., H. Peisi, and W. Waidelich, Phys. Letters 27A, 31 (1968).

30. Parker, J. H., Phys. Rev. 124, 703 (1961).

31. Kaplan, E. Nuclear Physics. Addison-Wesley Publishing Co., Inc., Reading, Massachusetts, copyright 1962.

32. Varley, J. H. O., Nature 174, 886 (1954).

33. Ritz, V. H., Phys. Rev. 142, 505 (1966).

34. Dexter, D. L., Phys. Rev. 118, 934 (1960).

35. Pooley, D., Proc. Phys. Soc. 87, 245 (1966).

36. Hughes, A. E., D. Pooley, H. V. Rohman, and W. A. Runciman. AERE R 5604 (1967).

37. Keller, J. F. and F. W. Patten, Solid State Comm. 7, 1603 (1969).

38. Pooley, D., and W. A. Runciman, Solid State Comm. 4, 351 (1966).

39. Hersh, H. N., Phys. Rev. 148, 928 (1966).

40. Ueta, M., Y. Kondo, M. Hirai, and T. Yoshinary., J. Phys. Soc. Japan 26, 1000 (1969).

41. Still, P. B., and D. Pooley, Phys. Stat. Sol. 32K, 147 (1969).

42. Hayes, W., and R. F. Lambourn, J. Phys. C. 7, 2429 (1974).

43. Sibley, W. A., and O. E. Facey, Phys. Rev. 174, 1076 (1968).

44. Riley, C. R., and W. A. Sibley, Phys. Rev. B1, 2789 (1970).

45. Koumvakalis, N. and W. A. Sibley (private communication).

46. Sonder, E., Phys. Stat. Sol. 35, 523 (1969).

47. Pooley, D., Proc. Phys. Soc. 89, 723 (1966).

48. Ikeya, M., N. Itoh and T. Suita, J. Phys. Soc. Japan 26, 291 (1969).

49. Al'tshuler, N. S., E. Kh. Ivoilova, L. D. Livanova, V. G. Stepanov, and A. L. Stolov, Sov. Phys. Solid State 15, 1973 (1974).

50. Vehse, W. E. and W. A. Sibley, Phys. Rev. B6, 2443 (1972).

51. Sibley, W. A., S. I. Yun, and W. E. Vehse, J. Phys. C6, 1105 (1973).

52. Yun, S. I., K. H. Lee, W. A. Sibley, and W. E. Vehse, Phys. Rev. B10, 1665 (1974).

53. Chao, E. C. T., H. T. Evans, and B. J. Skinner, Amer. Mineral. 46, 379 (1961).

54. Megaw, H. D., Crystal Structures: A Working Approach. W. B. Saunders Company, Philadelphia, Pennsylvania, Copyright, 1973.

55. Modine, F. A., E. Sonder, and W. P. Unruh, Phys. Rev. B10, 1623 (1974).

56. Martin, J. J. (private communication).

57. Kay, H. F., and P. C. Bailey, Acta Cryst. 10, 219 (1957).

58. Marezio, M., P. D. Dernier, and J. P. Remeika, J. Sol. State Chem. 4, 11 (1972).

59. Rhoads, J. E., Ph.D. Thesis (Oklahoma State University, 1974).

60. Abragam, A. and B. Bleaney, Electron Paramagnetic Resonance of Transition Ions (Clarendon Press, Oxford, 1970).

61. Ogawa, S., and Y. Yokozawa, J. Phys. Soc. Japan 14, 1116 (1959).

62. Newman, D. J., and W. Urban, Advances in Physics 24, 793 (1975).

63. Riley, C. R., S. I. Yun, and W. A. Sibley, Phys. Rev. B5, 3285 (1972).

64. Riley, C. R., Ph.D. Thesis (University of Tennessee, 1970).

65. Schoemaker, D., Phys. Rev. B7, 786 (1973).

66. Halliburton, L. E. (private communication).

67. Brynestad, J., H. L. Yakel, and G. P. Smith, J. Chem. Phys. 45, 4652 (1966).

68. Mertz, J. L., and P. S. Persham, Phys. Rev. 141, 352 (1966).

69. MacInerney, J. A., Ph.D. Thesis (Oklahoma State University, 1974).

APPENDIX A

Mn^{2+}-FLUORINE VACANCY CENTER FITTING PROGRAM

```
0001                IMPLICIT REAL*8(A-H,O-Z)
0002                REAL*8 AR(36,36),AI(36,36),E(36),E2(36),TAU(2,36)
                   C,B(36),P(6),FREQ(22),T2(3,3)
0003                P(1) = 2.0027D+00
0004                P(2) = 3.2D+01
0005                P(3) = 1.5567ID+03
0006                P(4) = 3.2176D+02
0007                P(5) = -2.3D+01
0008                P(6) = -2.81250+02
0009                B = 9.27D+00/6.626D+00
0010                FREQ0 = 9.242362D+03
0011                N = 36
0012                NM = 36
0013              1 DO 90 LL = 1,6
0014                KK = 1
0015              2 J = 1
0016              3 GO TO (60,5,6,60,60,60,60,11,60,13,60,
                   C60,16,17,60,60,60,21,60,60,24,60),J
0017              4 H = 5.58555D+03
0018                I = 3
0019                GO TO 26
0020              5 H = 5.68071D+03
0021                I = 4
0022                GO TO 26
0023              6 H = 5.78247D+03
0024                I = 5
0025                GO TO 26
0026              7 H = 5.88871D+03
0027                I = 6
0028                GO TO 26
0029              8 H = 4.39518D+03
0030                I = 9
0031                GO TO 26
0032              9 H = 4.49540D+03
0033                I = 10
0034                GO TO 26
0035             10 H = 4.59811D+03
0036                I = 11
0037                GO TO 26
0038             11 H = 4.70317D+03
0039                I = 12
0040                GO TO 26
0041             12 H = 2.07956D+03
0042                I = 22
0043                GO TO 26
0044             13 H = 1.97247D+03
0045                I = 23
0046                GO TO 26
0047             14 H = 1.8641 0D+03
0048                I = 34
0049                GO TO 27
0050             15 H = 4.9350 0D+03
0051                I = 30
0052                GO TO 27
0053             16 H = 5.0345 0D+03
0054                I = 29
0055                GO TO 27
0056             17 H = 5.1208 0D+03
```

```
0057                I = 28
0058                GO TO 27
0059             18 H = 2.22390D+03
0060                I = 27
0061                GO TO 27
0062             19 H = 5.83491D+03
0063                I = 26
0064                GO TO 27
0065             20 H = 3.85509D+03
0066                I = 24
0067                GO TO 27
0068             21 H = 3.95140D+03
0069                I = 23
0070                GO TO 27
0071             22 H = 4.04839D+03
0072                I = 22
0073                GO TO 27
0074             23 H = 2.60320D+03
0075                I = 12
0076                GO TO 27
0077             24 H = 2.51065D+03
0078                I = 11
0079                GO TO 27
0080             25 H = 2.41831D+03
0081                I = 10
0082                GO TO 27
0083             26 TR(1,3) = 0.0D+00
0084                TR(2,3) = 0.0D+00
0085                TR(3,3) = 1.0D+00
0086                GO TO 28
0087             27 TR(1,3) = 0.0D+00
0088                TR(2,3) = 1.0D+00
0089                TR(3,3) = 0.0D+00
0090             28 WI = P(1)*B*H*TR(2,3)/2.0D+00
0091                W2 = P(1)*B*H*TR(3,3)
0092                W3 = P(5)
0093                DO 29 K = 1,36
0094                DO 29 L = 1,36
0095                AR(K,L) = 0.0D+00
0096             29 AI(K,L) = 0.0D+00
0097                DO 30 K = 1,6
0098                AR(K,K) = 2.5D+00*(W2-P(6)*(K-1))+5.0D-01*W3
                   C+1.0D+01*P(3)/3.0D+00+6.25D+00*P(6)
0099                AI(6+K,K) = DSQRT(5.0D+01)*WI
0100                AR(7,2) = 2.5D+00*P(6)
0101                AR(8,3) = DSQRT(1.0D+01)*P(6)
0102                AR(9,4) = 1.5D+00*DSQRT(5.0D+00)*P(6)
0103                AR(10,5) = AR(8,3)
0104                AR(11,6) = AR(7,2)
0105                AR(12+K,K) = DSQRT(1.0D+01)*P(4)
0106                AR(24+K,K) = DSQRT(5.0D+00)*P(2)/2.0D+00
0107                AR(6+K,6+K) = 1.5D+00*(W2-W3-P(6)*(K-1))
                   C-2.0D+00*P(3)/3.0D+00+3.75D+00*P(5)
0108                AI(13+K,6+K) = 2.0D+00*DSQRT(2.0D+00)*WI
0109                AR(13,8) = DSQRT(1.0D+01)*P(6)
0110                AR(14,9) = 4.0D+00*P(6)
0111                AR(15,10) = 3.0D+00*DSQRT(2.0D+00)*P(6)
0112                AR(16,11) = AR(14,9)
```

```
0113                AR(17,12) = AR(13,8)
0114                AR(18+K,6+K) = 3.0D+00*DSQRT(2.0D+00)*P(4)
0115                AR(30+K,6+K) = DSQRT(5.0D+00)*P(2)/2.0D+00
0116                AR(12+K,12+K) = 5.0D-01*(W2-P(6)*(K-1))
                   C+W3-8.0D+00*P(3)/3.0D+00+1.25D+00*P(6)
0117                AI(18+K,12+K) = 3.0D+00*WI
0118                AR(19,14) = 1.5D+00*DSQRT(5.0D+00)*P(6)
0119                AR(20,15) = 3.0D+00*DSQRT(2.0D+00)*P(6)
0120                AR(21,16) = 4.5D+00*P(6)
0121                AR(22,17) = AR(20,15)
0122                AR(23,18) = AR(19,14)
0123                AR(24+K,12+K) = 3.0D+00*DSQRT(2.0D+00)*P(4)
0124                AR(18+K,18+K) = 5.0D-01*(P(6)*(K-1)-W2)+W3-8.0D+00*P(3)
                   C/3.0D+00-1.25D+00*P(6)
0125                AI(24+K,18+K) = 2.0D+00*DSQRT(2.0D+00)*WI
0126                AR(24+K,24+K) = 1.5D+00*(P(6)*(K-1)-W2-W3)-2.0D+00*P(3)
                   C/3.0D+00-3.75D+00*P(6)
0127                AI(30+K,24+K) = DSQRT(5.0D+00)*WI
0128                AR(30+K,30+K) = 2.5D+00*(P(6)*(K-1)-W2)+5.0D-01*W3
                   C+1.0D+01*P(3)/3.0D+00-6.25D+00*P(6)
0129             30 AR(30+K,18+K) = DSQRT(1.0D+01)*P(4)
0130                AR(25,20) = DSQRT(1.0D+01)*P(6)
0131                AR(26,21) = 4.0D+00*P(6)
0132                AR(27,22) = 3.0D+00*DSQRT(2.0D+00)*P(6)
0133                AR(28,25) = AR(26,21)
0134                AR(29,24) = AR(25,20)
0135                AR(31,26) = 2.5D+00*P(6)
0136                AR(32,27) = DSQRT(1.0D+01)*P(6)
0137                AR(33,28) = 1.5D+00*DSQRT(5.0D+00)*P(6)
0138                AR(34,29) = AR(32,27)
0139                AR(35,30) = AR(31,26)
0140                CALL HTRIDI(NM,N,AR,AI,D,E,E2,TAU)
0141                CALL IMTQLI(N,D,E,IERR)
0142                FREQ(J) = D(I+6)-D(I)
0143                GO TO 70
0144             60 FREQ(J) = FREQQ
0145             70 J = J+1
0146                IF(J-22)31,31,32
0147             31 GO TO 3
0148             32 SUM = 0.0D+00
0149                DO 33 J = 1,22
0150             33 SUM = SUM+(FREQ(J)-FREQQ)**2
0151                WRITE(6,50)SUM
0152                GO TO (34,43,45),KK
0153             34 SUM2 = SUM
0154                IF(LL-1)35,35,36
0155             35 SUM1 = SUM
0156             36 GO TO (37,38,39,40,41,55),LL
0157             37 DD = 3.0D-04
0158                GO TO 42
0159             38 DD = 1.0D+00
0160                GO TO 42
0161             39 DD = 1.0D+00
0162                GO TO 42
0163             40 DD = 1.0D+00
0164                GO TO 42
0165             41 DD = 1.0D+00
0166                GO TO 42
```

```
0167            55 DD = 1.0D+00
0168            42 P(LL) = P(LL) + DD
0169               KK = KK+1
0170               GO TO 2
0171            43 IF(SUM-SUM2)90,44,44
0172            44 P(LL) = P(LL)-2.0D+00*DD
0173               KK = KK+1
0174               GO TO 2
0175            45 IF(SUM-SUM2)90,46,46
0176            46 P(LL) = P(LL)+DD
0177            90 CONTINUE
0178               IF(SUM-SUM2)47,48,48
0179            47 SUM2 = SUM
0180            48 CONTINUE
0181               WRITE(6,50)SUM2
0182               WRITE(6,51) (P(I),I = 1,6)
0183               WRITE(6,52) (FREQ(J),J = 1,22)
0184               IF(SUM1-SUM2)49,49,1
0185            49 CONTINUE
0186            50 FORMAT('0','0',F22.5)
0187            51 FORMAT('0',4F17.4)
0188            52 FORMAT('0',8F13.2)
0189               STOP
0190               END
```

APPENDIX B

PROGRAM USED IN PREDICTING LINE POSITIONS FOR THE Mn^{2+}-FLUORINE VACANCY CENTER

```
0001                  IMPLICIT REAL*8 (A-H,O-Z)
0002                  REAL*8 AR(36,36),AI(36,36),E(36),E2(36),TAU(2,36),
                     CD(36),WP(30),T(3,3),TR(3,3),R(3,3),P(6)
0003                  P(1) = 2.0018D+00
0004                  P(2) = 2.0D+01
0005                  P(3) = -1.54871D+03
0006                  P(4) = 3.2376D+02
0007                  P(5) = -7.29D+00
0008                  P(6) = -2.8425D+02
0009                  WRITE (6,1 ) ( P(I),I=1,6 )
0010                1 FORMAT ( 6F14.4 )
0011                  B=9.27D+00/6.626D+00
0012                  FREQC = 6.2423e2D+03
0013                  N=36
0014                  NM=36
0015                  THETA = 0.0D+00
0016                  PHI = 0.0D+00
0017                2 C=1.0D+00
0018                  WRITE (6,3) THETA,PHI
0019                3 FORMAT ('0',2F15.3 )
0020                  THETAR=THETA*(3.14150+00/1.8D+02)
0021                  PHIR=PHI*(3.1415D+00/1.8D+02)
0022                  R(1,3)=DSIN(THETAR)*DCOS(PHIR)
0023                  R(2,3)=DSIN(PHIR)
0024                  R(3,3) = DCOS(THETAR)*DCOS(PHIR)
0025                5 I=1
0026                6 H=5.7D+03
0027                  DO 7 K=1,3
0028                  DO 7 L=1,3
0029                7 T(K,L)=0.0D+00
0030                8 T(1,1)=C
0031                  T(2,2)=C
0032                  T(3,3)=C
0033               20 DO 21 K=1,3
0034               21 TR(K,3)=T(K,1)*R(1,3)+T(K,2)*R(2,3)+T(K,3)*R(3,3)
0035               22 W1R=P(1)*B*H*TR(1,3)/2.0D+00
0036                  W1I=P(1)*B*H*TR(2,2)/2.0D+00
0037                  W2=P(1)*B*H*TR(3,3)
0038                  W3=P(2)+2.0D+00*P(5)/3.0D+00
0039                  DO 23 K=1,36
0040                  DO 23 L=1,36
0041                  AR(K,L)=0.0D+00
0042               23 AI(K,L)=0.0D+00
0043                  DO 24 K=1,6
0044                  AR(K,K)=2.0D+00*(W2-P(6)*(K-1))+5.0D-01*W3+1.0D+01*P(3)
                     6/3.0D+00+6.25D+00*P(6)
0045                  AR(6+K,K)=DSQRT(5.0D+00)*W1R
0046               24 AI(6+K,K)=DSQRT(5.0D+00)*W1I
0047                  AR(7,2)=2.5D+00*P(6)
0048                  AR(8,3)=DSQRT(1.0D+01)*P(6)
0049                  AR(9,4)=1.5D+00*DSQRT(5.0D+00)*P(6)
0050                  AR(10,5)=AR(8,3)
0051                  AR(11,6)=AR(7,2)
0052                  DO 25 K=1,5
0053                  AR(12+K,K)=DSQRT(1.0D+01)*P(4)
0054                  AR(24+K,K)=DSQRT(5.0D+00)*P(2)/2.0D+00
0055                  AR(3+K,6+K)=1.5D+00*(W2-W3-P(6)*(K-1))-2.0D+00*P(3)
                     6/3.0D+00+5.75D+00*P(6)
```

```
0056                AR(12+K,6+K)=2.0D+00*DSQRT(2.0D+00)*W1R
0057             25 AI(12+K,6+K)=2.0D+00*DSQRT(2.0D+00)*W1I
0058                AR(13,8)=DSQRT(1.0D+01)*P(6)
0059                AR(14,9)=4.0D+00*P(6)
0060                AR(15,10)=3.0D+00*DSQRT(2.0D+00)*P(6)
0061                AR(16,11)=AR(14,9)
0062                AR(17,12)=AR(13,8)
0063                DO 26 K=1,6
0064                AR(18+K,6+K)=2.0D+00*DSQRT(2.0D+00)*P(4)
0065                AR(30+K,6+K)=DSQRT(5.0D+00)*P(2)/2.0D+00
0066                AR(12+K,12+K)=5.0D-01*(W2-P(6)*(K-1))+W3-8.0D+00*P(3)
                   C/3.0D+00+1.25D+00*P(6)
0067                AR(18+K,12+K)=3.0D+00*W1R
0068             26 AI(18+K,12+K)=3.0D+00*W1I
0069                AR(19,14)=1.5D+00*DSQRT(5.0D+00)*P(6)
0070                AR(20,15)=3.0D+00*DSQRT(2.0D+00)*P(6)
0071                AR(21,16)=4.5D+00*P(6)
0072                AR(22,17)=AR(20,15)
0073                AR(23,18)=AR(19,14)
0074                DO 27 K=1,6
0075                AR(24+K,12+K)=2.0D+00*DSQRT(2.0D+00)*P(4)
0076                AR(18+K,18+K)=5.0D-01*(P(6)*(K-1)-W2)+W3-8.0D+00*P(3)
                   C/3.0D+00-1.25D+00*P(6)
0077                AR(24+K,18+K)=2.0D+00*DSQRT(2.0D+00)*W1R
0078                AI(24+K,18+K)=2.0D+00*DSQRT(2.0D+00)*W1I
0079                AR(24+K,24+K)=1.5D+00*(P(6)*(K-1)-W2-W3)-2.0D+00*P(3)
                   C/3.0D+00-3.75D+00*P(6)
0080                AR(30+K,24+K)=DSQRT(5.0D+00)*W1R
0081                AI(30+K,24+K)=DSQRT(5.0D+00)*W1I
0082                AR(30+K,30+K)=2.5D+00*(P(6)*(K-1)-W2)+5.0D-01*W3+1.0D+01*P(3)
                   C/3.0D+00-9.25D+00*P(6)
0083             27 AR(30+K,18+K)=DSQRT(1.0D+01)*P(4)
0084                AR(25,20)=DSQRT(1.0D+01)*P(6)
0085                AR(26,21)=4.0D+00*P(6)
0086                AR(27,22)=3.0D+00*DSQRT(2.0D+00)*P(6)
0087                AR(28,23)=AR(26,21)
0088                AR(29,24)=AR(25,20)
0089                AR(31,25)=2.5D+00*P(6)
0090                AR(32,27)=DSQRT(1.0D+01)*P(6)
0091                AR(33,28)=1.5D+00*DSQRT(5.0D+00)*P(6)
0092                AR(34,29)=AR(32,27)
0093                AR(35,30)=AR(31,26)
0094                CALL EIGDI (NM,N,AR,AI,D,E,E2,TAU)
0095                CALL IMTQL1 (N,D,E,IERR)
0096                WRITE (6,33) H
0097             33 FORMAT (F25.4)
0098                FREQ=D(I+6)-D(I)
0099                IF(DABS(FREQ-FREQ0)-3.0D+00) 28,28,29
0100             28 PP(I)=H
0101                WRITE (6,34) P(I)
0102                GO TO 30
0103             29 H=H*(FREQ0/FREQ)
0104                GO TO 22
0105             30 IF (I-30) 31,30,32
0106             31 I = I+1
0107                H=H+9.0D+01
0108                GO TO 22
0109             32 WRITE(6,33) (PP(I),I=1,30)
```

```
0110          35 FORMAT (6F18.2)
0111             STOP
0112             END
```

APPENDIX C

[110]-TYPE V_K CENTER FITTING PROGRAM

```
0001                  IMPLICIT REAL*8(A-H,O-Z)
0002                  REAL*8 AR(8,8),AI(8,8),E(8),E2(8),TAU(2,8),D(8),P(8),FREQ(14),
                     CG(3,3),T(3,3),R(3,3),TR(3,3),GTR(3,3),W(21),BB(3,3),BBB(3,3),
                     CF(3,3),S(3,3)
0003                  BETA = 7.0D+00
0004                  BETAR = BETA*(3.1415D+00/1.8D+02)
0005                  P(1) = 2.02D+00
0006                  P(2) = 2.02D+00
0007                  P(3) = 2.0025D+00
0008                  P(4) = 5.0D+01
0009                  P(5) = 5.0D+01
0010                  P(6) = 2.5D+03
0011                  P(7) = 1.56D+01
0012                  P(8) = 1.84D+01
0013                  B = 9.27D+00/6.626D+00
0014                  FREQQ = 9.1779522D+03
0015                  GBN = 5.6446D+01/1.4092D+04
0016                  N = 8
0017                  NM = 8
0018                1 DO 75 LL = 1,8
0019                  GO TO (91,75,75,75,75,75,91,91),LL
0020               91 KK = 1
0021                2 J = 1
0022                  P(2) = P(1)
0023                  P(5) = P(4)
0024                3 GO TO (4,5,6,7),J
0025                4 H = 3.55678D+03
0026                  I = 4
0027                  JJ = 1
0028                  GO TO 27
0029                5 H = 2.74035D+03
0030                  I = 1
0031                  JJ = 1
0032                  GO TO 27
0033                6 H = 4.01144D+03
0034                  I = 4
0035                  JJ = 1
0036                  GO TO 28
0037                7 H = 2.45731D+03
0038                  I = 1
0039                  JJ = 1
0040                  GO TO 28
0041               26 THETA = 4.5D+01
0042                  ALPHA = 9.0D+01
0043                  OMEGA = P(7)
0044                  PSI = P(8)
0045                  GO TO 60
0046               27 OMEGA = -P(7)
0047                  PSI = -P(8)
0048                  THETA = 4.5D+01
0049                  ALPHA = 0.0D+00
0050                  GO TO 60
0051               28 THETA = 4.5D+01
0052                  ALPHA = 0.0D+00
0053                  OMEGA = P(7)
0054                  PSI = P(8)
0055               60 DO 30 K = 1,3
0056                  DO 30 L = 1,3
```

```
0057            30 G(K,L) = 0.0D+00
0058               GO TO (18,19,20,21,22,23),JJ
0059            18 G(1,1) = 1.0D+00
0060               G(2,2) = 1.0D+00
0061               G(3,3) = 1.0D+00
0062               GO TO 31
0063            19 G(1,1) = 0.5D+00
0064               G(1,2) = DSQRT(2.0D+00)/2.0D+00
0065               G(1,3) = -G(1,1)
0066               G(2,1) = -G(1,2)
0067               G(2,3) = -G(1,2)
0068               G(3,1) = -G(1,1)
0069               G(3,2) = G(1,2)
0070               G(3,3) = G(1,1)
0071               GO TO 31
0072            20 G(1,1) = -0.5D+00
0073               G(1,2) = DSQRT(2.0D+00)/2.0D+00
0074               G(1,3) = -G(1,1)
0075               G(2,1) = G(1,2)
0076               G(2,3) = G(1,2)
0077               G(3,1) = -G(1,1)
0078               G(3,2) = G(1,2)
0079               G(3,3) = G(1,1)
0080               GO TO 31
0081            21 G(1,1) = -0.5D+00
0082               G(1,2) = DSQRT(2.0D+00)/2.0D+00
0083               G(1,3) = G(1,1)
0084               G(2,1) = -G(1,2)
0085               G(2,3) = G(1,2)
0086               G(3,1) = -G(1,1)
0087               G(3,2) = G(1,2)
0088               G(3,3) = -G(1,1)
0089               GO TO 31
0090            22 G(1,1) = 0.5D+00
0091               G(1,2) = DSQRT(2.0D+00)/2.0D+00
0092               G(1,3) = G(1,1)
0093               G(2,1) = G(1,2)
0094               G(2,3) = -G(1,2)
0095               G(3,1) = -G(1,1)
0096               G(3,2) = G(1,2)
0097               G(3,3) = -G(1,1)
0098               GO TO 31
0099            23 G(1,3) = 1.0D+00
0100               G(2,2) = -1.0D+00
0101               G(3,1) = G(1,3)
0102            31 OMEGAR = OMEGA*(3.1415D+00/1.8D+02)
0103               PSIR = PSI*(3.1415D+00/1.8D+02)
0104               THETAR = THETA*(3.1415D+00/1.8D+02)
0105               ALPHAR = ALPHA*(3.1415D+00/1.8D+02)
0106               T(1,1) = DCOS(PSIR)*DCOS(OMEGAR)
0107               T(1,2) = DSIN(PSIR)
0108               T(1,3) = DCOS(PSIR)*DSIN(OMEGAR)
0109               T(2,1) = -DSIN(PSIR)*DCOS(OMEGAR)
0110               T(2,2) = DCOS(PSIR)
0111               T(2,3) = -DSIN(PSIR)*DSIN(OMEGAR)
0112               T(3,1) = -DSIN(OMEGAR)
0113               T(3,2) = 0.0D+00
0114               T(3,3) = DCOS(OMEGAR)
```

```
0115          32 R(1,1) = DCOS(THETAR)
0116             R(1,2) = DSIN(THETAR)*DSIN(ALPHAR)
0117             R(1,3) = -DSIN(THETAR)*DCOS(ALPHAR)
0118             R(2,1) = 0.0D+00
0119             R(2,2) = DCOS(ALPHAR)
0120             R(2,3) = DSIN(ALPHAR)
0121             R(3,1) = DSIN(THETAR)
0122             R(3,2) = -DCOS(THETAR)*DSIN(ALPHAR)
0123             R(3,3) = DCOS(THETAR)*DCOS(ALPHAR)
0124             DO 33 K = 1,3
0125             DO 33 L = 1,3
0126          33 TR(K,L) = T(K,1)*R(1,L)+T(K,2)*R(2,L)+T(K,3)*R(3,L)
0127             DO 34 K = 1,3
0128             DO 34 L = 1,3
0129          34 GTR(K,L) = G(K,1)*TR(1,L)+G(K,2)*TR(2,L)+G(K,3)*TR(3,L)
0130             BB(1,1) = DCOS(BETAR)
0131             BB(1,2) = 0.0D+00
0132             BB(1,3) = DSIN(BETAR)
0133             BB(2,1) = 0.0D+00
0134             BB(2,2) = 1.0D+00
0135             BB(2,3) = 0.0D+00
0136             BB(3,1) = -DSIN(BETAR)
0137             BB(3,2) = 0.0D+00
0138             BB(3,3) = DCOS(BETAR)
0139             BBB(1,1) = BB(1,1)
0140             BBB(1,2) = BB(1,2)
0141             BBB(1,3) = -BB(1,3)
0142             BBB(2,1) = BB(2,1)
0143             BBB(2,2) = BB(2,2)
0144             BBB(2,3) = BB(2,3)
0145             BBB(3,1) = -BB(3,1)
0146             BBB(3,2) = BB(3,2)
0147             BBB(3,3) = BB(3,3)
0148             DO 95 K = 1,3
0149             DO 95 L = 1,3
0150          95 F(K,L) = BB(K,1)*GTR(1,L)+BB(K,2)*GTR(2,L)+BB(K,3)*GTR(3,L)
0151             DO 96 K = 1,3
0152             DO 96 L = 1,3
0153          96 S(K,L) = BBB(K,1)*GTR(1,L)+BBB(K,2)*GTR(2,L)+BBB(K,3)*GTR(3,L)
0154             W(1) = B*H*(GTR(1,3)*GTR(1,1)*P(1)+GTR(2,3)*GTR(2,1)*P(2)
               C+GTR(3,3)*GTR(3,1)*P(3))
0155             W(2) = B*H*(GTR(1,3)*GTR(1,2)*P(1)+GTR(2,3)*GTR(2,2)*P(2)
               C+GTR(3,3)*GTR(3,2)*P(3))
0156             W(3) = B*H*(GTR(1,3)*GTR(1,3)*P(1)+GTR(2,3)*GTR(2,3)*P(2)
               C+GTR(3,3)*GTR(3,3)*P(3))
0157             W(4) = F(1,1)*F(1,1)*P(4)+F(2,1)*F(2,1)*P(5)+F(3,1)*F(3,1)*P(6)
0158             W(5) = F(1,1)*F(1,2)*P(4)+F(2,1)*F(2,2)*P(5)+F(3,1)*F(3,2)*P(6)
0159             W(6) = F(1,1)*F(1,3)*P(4)+F(2,1)*F(2,3)*P(5)+F(3,1)*F(3,3)*P(6)
0160             W(7) = F(1,2)*F(1,1)*P(4)+F(2,2)*F(2,1)*P(5)+F(3,2)*F(3,1)*P(6)
0161             W(8) = F(1,2)*F(1,2)*P(4)+F(2,2)*F(2,2)*P(5)+F(3,2)*F(3,2)*P(6)
0162             W(9) = F(1,2)*F(1,3)*P(4)+F(2,2)*F(2,3)*P(5)+F(3,2)*F(3,3)*P(6)
0163             W(10) = F(1,3)*F(1,1)*P(4)+F(2,3)*F(2,1)*P(5)+F(3,3)*F(3,1)*P(6)
0164             W(11) = F(1,3)*F(1,2)*P(4)+F(2,3)*F(2,2)*P(5)+F(3,3)*F(3,2)*P(6)
0165             W(12) = F(1,3)*F(1,3)*P(4)+F(2,3)*F(2,3)*P(5)+F(3,3)*F(3,3)*P(6)
0166             W(13) = S(1,1)*S(1,1)*P(4)+S(2,1)*S(2,1)*P(5)+S(3,1)*S(3,1)*P(6)
0167             W(14) = S(1,1)*S(1,2)*P(4)+S(2,1)*S(2,2)*P(5)+S(3,1)*S(3,2)*P(6)
0168             W(15) = S(1,1)*S(1,3)*P(4)+S(2,1)*S(2,3)*P(5)+S(3,1)*S(3,3)*P(6)
0169             W(16) = S(1,2)*S(1,1)*P(4)+S(2,2)*S(2,1)*P(5)+S(3,2)*S(3,1)*P(6)
```

```
0170              W(17) = S(1,2)*S(1,2)*P(4)+S(2,2)*S(2,2)*P(5)+S(3,2)*S(3,2)*P(6)
0171              W(18) = S(1,2)*S(1,3)*P(4)+S(2,2)*S(2,3)*P(5)+S(3,2)*S(3,3)*P(6)
0172              W(19) = S(1,3)*S(1,1)*P(4)+S(2,3)*S(2,1)*P(5)+S(3,3)*S(3,1)*P(6)
0173              W(20) = S(1,3)*S(1,2)*P(4)+S(2,3)*S(2,2)*P(5)+S(3,3)*S(3,2)*P(6)
0174              W(21) = S(1,3)*S(1,3)*P(4)+S(2,3)*S(2,3)*P(5)+S(3,3)*S(3,3)*P(6)
0175              DO 97 K = 1,8
0176              DO 97 L = 1,8
0177              AR(K,L) = 0.0D+00
0178           97 AI(K,L) = 0.0D+00
0179              AR(1,1) = 0.5D+00*W(3)+0.25D+00*(W(12)+W(21))-GBN*H
0180              AR(2,2) = 0.5D+00*W(3)+0.25D+00*(W(12)-W(21))
0181              AR(3,3) = 0.5D+00*W(3)-0.25D+00*(W(12)-W(21))
0182              AR(4,4) = 0.5D+00*W(3)-0.25D+00*(W(12)+W(21))+GBN*H
0183              AR(5,5) = -0.5D+00*W(3)-0.25D+00*(W(12)+W(21))-GBN*H
0184              AR(6,6) = -0.5D+00*W(3)-0.25D+00*(W(12)-W(21))
0185              AR(7,7) = -0.5D+00*W(3)+0.25D+00*(W(12)-W(21))
0186              AR(8,8) = -0.5D+00*W(3)+0.25D+00*(W(12)+W(21))+GBN*H
0187              AR(2,1) = W(15)/4.0D+00
0188              AI(2,1) = W(18)/4.0D+00
0189              AR(3,1) = W(6)/4.0D+00
0190              AI(3,1) = W(9)/4.0D+00
0191              AR(5,1) = 0.5D+00*W(1)+0.25D+00*(W(10)+W(19))
0192              AI(5,1) = 0.5D+00*W(2)+0.25D+00*(W(11)+W(20))
0193              AR(6,1) = 0.25D+00*(W(13)-W(17))
0194              AI(6,1) = 0.25D+00*(W(14)+W(16))
0195              AR(7,1) = 0.25D+00*(W(4)-W(8))
0196              AI(7,1) = 0.25D+00*(W(5)+W(7))
0197              AR(4,2) = AR(3,1)
0198              AI(4,2) = AI(3,1)
0199              AR(5,2) = 0.25D+00*(W(13)+W(17))
0200              AI(5,2) = 0.25D+00*(W(14)-W(16))
0201              AR(6,2) = W(1)/2.0D+00+(W(10)-W(19))/4.0D+00
0202              AI(6,2) = W(2)/2.0D+00+(W(11)-W(20))/4.0D+00
0203              AR(8,2) = AR(7,1)
0204              AI(8,2) = AI(7,1)
0205              AR(4,3) = AR(2,1)
0206              AI(4,3) = AI(2,1)
0207              AR(5,3) = 0.25D+00*(W(4)+W(8))
0208              AI(5,3) = 0.25D+00*(W(5)-W(7))
0209              AR(7,3) = W(1)/2.0D+00-(W(10)-W(19))/4.0D+00
0210              AI(7,3) = W(2)/2.0D+00-(W(11)-W(20))/4.0D+00
0211              AR(8,3) = AR(6,1)
0212              AI(8,3) = AI(6,1)
0213              AR(6,4) = AR(5,3)
0214              AI(6,4) = AI(5,3)
0215              AR(7,4) = AR(5,2)
0216              AI(7,4) = AI(5,2)
0217              AR(8,4) = W(1)/2.0D+00-(W(10)+W(19))/4.0D+00
0218              AI(8,4) = W(2)/2.0D+00-(W(11)+W(20))/4.0D+00
0219              AR(6,5) = -AR(2,1)
0220              AI(6,5) = -AI(2,1)
0221              AR(7,5) = -AR(3,1)
0222              AI(7,5) = -AI(3,1)
0223              AR(8,6) = -AR(3,1)
0224              AI(8,6) = -AI(3,1)
0225              AR(8,7) = -AR(2,1)
0226              AI(8,7) = -AI(2,1)
0227              CALL HTRIDI (NM,N,AR,AI,D,E,E2,TAU)
```

```
0228                CALL IMTQL1 (N,D,E,IERR)
0229                FREQ(J) = D(9-I)-D(I)
0230                J = J+1
0231                IF(J-4)35,35,36
0232             35 GO TO 3
0233             36 SUM = 0.0D+00
0234                DO 37 J = 1,4
0235             37 SUM = SUM+(FREQ(J)-FREQQ)**2
0236                WRITE(6,50) SUM
0237                GO TO (38,70,80),KK
0238             38 SUM2 = SUM
0239                IF(LL-1)39,39,40
0240             39 SUM1 = SUM
0241             40 GO TO (75,75,41,75,75,42,85,86),LL
0242             41 DD = 1.0D-04
0243                GO TO 43
0244             42 DD = 1.0D+00
0245                GO TO 43
0246             85 DD = 0.05D+00
0247                GO TO 43
0248             86 DD = 0.05D+00
0249             43 P(LL) = P(LL)+DD
0250                KK = KK+1
0251                GO TO 2
0252             70 IF(SUM-SUM2)75,44,44
0253             44 P(LL) = P(LL)-2.0D+00*DD
0254                KK = KK+1
0255                GO TO 2
0256             80 IF(SUM-SUM2)75,45,45
0257             45 P(LL) = P(LL)+DD
0258             75 CONTINUE
0259                IF(SUM-SUM2)46,47,47
0260             46 SUM2 = SUM
0261             47 CONTINUE
0262                WRITE(6,50)SUM2
0263                WRITE(6,51) (P(I),I = 1,8)
0264                WRITE(6,52) (FREQ(J),J = 1,4)
0265                IF(SUM1-SUM2)48,48,1
0266             48 CONTINUE
0267             50 FORMAT('0',F22.5)
0268             51 FORMAT('0',4F17.4)
0269             52 FORMAT('0',8F13.2)
0270                STOP
0271                END
```

APPENDIX D

PROGRAM USED IN PREDICTING LINE POSITIONS FOR THE [110]-TYPE V_K CENTER

```
0001                  IMPLICIT REAL*8 (A-H,O-Z)
0002                  REAL*8 P(6),E(8),E2(8),TAU(2,8),D(8),HF(4),G(3,3),T(3,3),R(3,3),
                     1GTR(3,3),GTR(3,3),W(21),AP(8,8),AI(8,8),DOMROT(3,3),TD(3,3),
                     2RB(3,3),BBB(3,3),F(3,3),S(3,3)
0003                  BETA = 7.0D+00
0004                  BETAR = BETA*(3.1415D+00/1.8D+02)
0005                  P(1) = 2.024D+00
0006                  P(2) = 2.018D+00
0007                  P(3) = 2.0024D+00
0008                  P(4) = 1.60D+02
0009                  P(5) = 1.60D+02
0010                  P(6) = 2.479D+03
0011                  WRITE(6,1) (P(I),I = 1,6)
0012                1 FORMAT(6F15.4)
0013                  R = 9.27D+00/6.626D+00
0014                  FREQQ = 9.1779522D+03
0015                  GBN = 5.6446D+01/1.4092D+04
0016                  N = 8
0017                  NM = 8
0018                  THETA = 4.5D+01
0019                  OMEGA = 1.52D+01
0020                  ALPHA = 0.0D+00
0021                170 JJ = 1
0022                 70 OMEGA = DABS(OMEGA)
0023                  PSI = 1.84D+01
0024                 65 WRITE(6,3) OMEGA,PSI,THETA,ALPHA,BETA
0025                  3 FORMAT('0',4F15.3)
0026                    OMEGAR = OMEGA*(3.1415D+00/1.8D+02)
0027                    PSIR = PSI*(3.1415D+00/1.8D+02)
0028                    THETAR = THETA*(3.1415D+00/1.8D+02)
0029                    ALPHAR = ALPHA*(3.1415D+00/1.8D+02)
0030                    J = 1
0031                 60 DO 30 K = 1,3
0032                    DO 30 L = 1,3
0033                 30 G(K,L) = 0.0D+00
0034                    GO TO (4,5,6,7,8,9),J
0035                  4 G(1,1) = 1.0D+00
0036                    G(2,2) = 1.0D+00
0037                    G(3,3) = 1.0D+00
0038                    GO TO 11
0039                  5 G(1,1) = 0.5D+00
0040                    G(1,2) = DSQRT(2.0D+00)/2.0D+00
0041                    G(1,3) = -G(1,1)
0042                    G(2,1) = -G(1,2)
0043                    G(2,3) = -G(1,2)
0044                    G(3,1) = -G(1,1)
0045                    G(3,2) = G(1,2)
0046                    G(3,3) = G(1,1)
0047                    GO TO 11
0048                  6 G(1,1) = -0.5D+00
0049                    G(1,2) = DSQRT(2.0D+00)/2.0D+00
0050                    G(1,3) = -G(1,1)
0051                    G(2,1) = G(1,2)
0052                    G(2,3) = G(1,2)
0053                    G(3,1) = -G(1,1)
0054                    G(3,2) = G(1,2)
0055                    G(3,3) = G(1,1)
0056                    GO TO 11
```

```
0057            7 G(1,1) = -0.5D+00
0058              G(1,2) = DSQRT(2.0D+00)/2.0D+00
0059              G(1,3) = G(1,1)
0060              G(2,1) = -G(1,2)
0061              G(2,2) = G(1,2)
0062              G(3,1) = -G(1,1)
0063              G(3,2) = G(1,2)
0064              G(3,3) = -G(1,1)
0065              GO TO 11
0066            8 G(1,1) = 0.5D+00
0067              G(1,2) = DSQRT(2.0D+00)/2.0D+00
0068              G(1,3) = G(1,1)
0069              G(2,1) = G(1,2)
0070              G(2,2) = -G(1,2)
0071              G(3,1) = -G(1,1)
0072              G(3,2) = G(1,2)
0073              G(3,3) = -G(1,1)
0074              GO TO 11
0075            9 G(1,3) = 1.0D+00
0076              G(2,2) = -1.0D+00
0077              G(3,1) = G(1,3)
0078           11 T(1,1) = DCOS(PSIR)*DCOS(OMEGAR)
0079              T(1,2) = DSIN(PSIR)
0080              T(1,3) = DCOS(PSIR)*DSIN(OMEGAR)
0081              T(2,1) = -DSIN(PSIR)*DCOS(OMEGAR)
0082              T(2,2) = DCOS(PSIR)
0083              T(2,3) = -DSIN(PSIR)*DSIN(OMEGAR)
0084              T(3,1) = -DSIN(OMEGAR)
0085              T(3,2) = 0.0D+00
0086              T(3,3) = DCOS(OMEGAR)
                C     THE DOMROT TRANSFORMATION TAKES INTO ACCOUNT THE EFFECT OF
                C     DOMAINS IN THE CRYSTAL. TWELVE DOMAINS WILL BE CONSIDERED. EACH
                C     DOMAIN IS DISTINGUISHABLE BY THE SENSE OF THE ROTATIONS OF THE
                C     TILT ANGLES OMEGA AND PSI. OMEGA IS A ROTATION ABOUT A TETRAD
                C     AXIS, AND THERE ARE THREE DIFFERENT TETRAD AXES. THE PSI ROTATION
                C     FOLLOWS THE OMEGA ROTATION AND MAY OCCUR ABOUT ANY ONE OF FOUR
                C     DIFFERENT DIAD AXES. NOTE THAT OMEGA ROTATIONS ABOUT THE THREE
                C     NEGATIVE TETRAD AXES DO NOT CONSTITUTE DIFFERENT DOMAINS SINCE
                C     SUCH ROTATIONS ARE ALREADY INCLUDED IN EACH DOMAIN BY DEFINITION
                C     AND WITHIN THE COMPUTER PROGRAM THROUGH A CHANGE IN SIGN OF
                C     OMEGA AND PSI. THE ROTATIONS UNIQUELY DEFINE THE XYZ CRYSTAL AXES.
0087          100 DO 101 K = 1,3
0088              DO 101 L = 1,3
0089           10 DOMROT(K,L) = 0.0D+00
0090              GO TO (102,103,104,105,106,107,115,116,117,118,119,120),JJ
0091           102 DOMROT(1,1) = 1.0D+00
0092              DOMROT(2,2) = 1.0D+00
0093              DOMROT(3,3) = 1.0D+00
0094              GO TO 110
0095           103 DOMROT(1,3) = 1.0D+00
0096              DOMROT(2,2) = 1.0D+00
0097              DOMROT(3,1) = -1.0D+00
0098              GO TO 110
0099           104 DOMROT(1,1) = -1.0D+00
0100              DOMROT(2,2) = 1.0D+00
0101              DOMROT(3,3) = -1.0D+00
0102              GO TO 110
0103           105 DOMROT(1,3) = -1.0D+00
```

```
0104                DDMROT(2,2) = 1.0D+00
0105                DDMROT(3,1) = 1.0D+00
0106                GO TO 110
0107          106   DDMROT(1,1) = 0.5D+00
0108                DDMROT(1,2) = DSQRT(2.0D+00)/2.0D+00
0109                DDMROT(1,3) = -0.5D+00
0110                DDMROT(2,1) = -DSQRT(2.0D+00)/2.0D+00
0111                DDMROT(2,2) = -DSQRT(2.0D+00)/2.0D+00
0112                DDMROT(3,1) = -0.5D+00
0113                DDMROT(3,2) = DSQRT(2.0D+00)/2.0D+00
0114                DDMROT(3,3) = 0.5D+00
0115                GO TO 110
0116          107   DDMROT(1,1) = -0.5D+00
0117                DDMROT(1,2) = DSQRT(2.0D+00)/2.0D+00
0118                DDMROT(1,3) = 0.5D+00
0119                DDMROT(2,1) = -DSQRT(2.0D+00)/2.0D+00
0120                DDMROT(2,2) = -DSQRT(2.0D+00)/2.0D+00
0121                DDMROT(3,1) = -0.5D+00
0122                DDMROT(3,2) = -DSQRT(2.0D+00)/2.0D+00
0123                DDMROT(3,3) = 0.5D+00
0124                GO TO 110
0125          115   DDMROT(1,1) = -0.5D+00
0126                DDMROT(1,2) = -DSQRT(2.0D+00)/2.0D+00
0127                DDMROT(1,3) = 0.5D+00
0128                DDMROT(2,1) = -DSQRT(2.0D+00)/2.0D+00
0129                DDMROT(2,3) = -DSQRT(2.0D+00)/2.0D+00
0130                DDMROT(3,1) = 0.5D+00
0131                DDMROT(3,2) = -DSQRT(2.0D+00)/2.0D+00
0132                DDMROT(3,3) = -0.5D+00
0133                GO TO 110
0134          116   DDMROT(1,1) = 0.5D+00
0135                DDMROT(1,2) = -DSQRT(2.0D+00)/2.0D+00
0136                DDMROT(1,3) = -0.5D+00
0137                DDMROT(2,1) = -DSQRT(2.0D+00)/2.0D+00
0138                DDMROT(2,3) = -DSQRT(2.0D+00)/2.0D+00
0139                DDMROT(3,1) = 0.5D+00
0140                DDMROT(3,2) = DSQRT(2.0D+00)/2.0D+00
0141                DDMROT(3,3) = -0.5D+00
0142                GO TO 110
0143          117   DDMROT(1,1) = 0.5D+00
0144                DDMROT(1,2) = -DSQRT(2.0D+00)/2.0D+00
0145                DDMROT(1,3) = 0.5D+00
0146                DDMROT(2,1) = DSQRT(2.0D+00)/2.0D+00
0147                DDMROT(2,3) = -DSQRT(2.0D+00)/2.0D+00
0148                DDMROT(3,1) = 0.5D+00
0149                DDMROT(3,2) = DSQRT(2.0D+00)/2.0D+00
0150                DDMROT(3,3) = 0.5D+00
0151                GO TO 110
0152          118   DDMROT(1,1) = 0.5D+00
0153                DDMROT(1,2) = DSQRT(2.0D+00)/2.0D+00
0154                DDMROT(1,3) = 0.5D+00
0155                DDMROT(2,1) = DSQRT(2.0D+00)/2.0D+00
0156                DDMROT(2,3) = -DSQRT(2.0D+00)/2.0D+00
0157                DDMROT(3,1) = -0.5D+00
0158                DDMROT(3,2) = DSQRT(2.0D+00)/2.0D+00
0159                DDMROT(3,3) = -0.5D+00
0160                GO TO 110
0161          119   DDMROT(1,1) = -0.5D+00
```

```
                      DCMROT(1,2) = DSQRT(2.0D+00)/2.0D+00
                      DCMROT(1,3) = -0.5D+00
                      DCMROT(2,1) = DSQRT(2.0D+00)/2.0D+00
                      DCMROT(2,2) = -DSQRT(2.0D+00)/2.0D+00
                      DCMROT(2,3) = 0.5D+00
                      DCMROT(3,1) = DSQRT(2.0D+00)/2.0D+00
                      DCMROT(3,2) = 0.5D+00
                      DCMROT(3,3) = 0.5D+00
                      GO TO 110
                  120 DCMROT(1,1) = -0.5D+00
                      DCMROT(1,2) = -DSQRT(2.0D+00)/2.0D+00
                      DCMROT(1,3) = -0.5D+00
                      DCMROT(2,1) = DSQRT(2.0D+00)/2.0D+00
                      DCMROT(2,2) = -DSQRT(2.0D+00)/2.0D+00
                      DCMROT(3,1) = 0.5D+00
                      DCMROT(3,2) = -DSQRT(2.0D+00)/2.0D+00
                      DCMROT(3,3) = 0.5D+00
                  110 R(1,1) = DCOS(THETAR)
                      R(1,2) = DSIN(THETAR)*DSIN(ALPHAR)
                      R(1,3) = -DSIN(THETAR)*DCOS(ALPHAR)
                      R(2,1) = 0.0D+00
                      R(2,2) = DCOS(ALPHAR)
                      R(2,3) = DSIN(ALPHAR)
                      R(3,1) = DSIN(THETAR)
                      R(3,2) = -DCOS(THETAR)*DSIN(ALPHAR)
                      R(3,3) = DCOS(THETAR)*DCOS(ALPHAR)
                      DO 111 K = 1,3
                      DO 111 L = 1,3
                  111 T(K,L) = T(K,1)*DCMROT(1,L)+T(K,2)*DCMROT(2,L)+T(K,3)*DCMROT(3,L)
                      DO 12 K = 1,3
                      DO 12 L = 1,3
                   12 TD(K,L) = TD(K,1)*R(1,L)+TD(K,2)*R(2,L)+TD(K,3)*R(3,L)
                      DO 13 K = 1,3
                      DO 13 L = 1,3
                   13 GTR(K,L) = G(K,1)*TR(1,L)+G(K,2)*TR(2,L)+G(K,3)*TR(3,L)
                      BB(1,1) = DCOS(BETAR)
                      BB(1,2) = 0.0D+00
                      BB(1,3) = DSIN(BETAR)
                      BB(2,1) = 0.0D+00
                      BB(2,2) = 1.0D+00
                      BB(2,3) = 0.0D+00
                      BB(3,1) = -DSIN(BETAR)
                      BB(3,2) = 0.0D+00
                      BB(3,3) = DCOS(BETAR)
                      BBB(1,1) = BB(1,1)
                      BBB(1,2) = BB(1,2)
                      BBB(1,3) = -BB(1,3)
                      BBB(2,1) = BB(2,1)
                      BBB(2,2) = BB(2,2)
                      BBB(2,3) = BB(2,3)
                      BBB(3,1) = -BB(3,1)
                      BBB(3,2) = BB(3,2)
                      BBB(3,3) = BB(3,3)
                      DO 40 K = 1,3
                      DO 40 L = 1,3
                   40 S(K,L) = BB(K,1)*GTR(1,L)+BB(K,2)*GTR(2,L)+BB(K,3)*GTR(3,L)
                      DO 41 K = 1,3
                      DO 41 L = 1,3
                   41 S(K,L) = BBB(K,1)*GTR(1,L)+BBB(K,2)*GTR(2,L)+BBB(K,3)*GTR(3,L)
```

```
0220                  T = 1
0221                50 H = 0.00+00
0222                14 W(1) = H*H*(GTR(1,2)*GTR(1,1)*P(1)+GTR(2,3)*GTR(2,1)*P(2)
                     0 +GTR(3,2)*GTR(3,1)*P(3))
0223                   W(2) = .5*H*(GTR(1,3)*GTR(1,2)*P(1)+GTR(2,3)*GTR(2,2)*P(2)
                     0 +GTR(3,3)*GTR(3,2)*P(3))
0224                   W(3) = H*H*(GTR(1,3)*GTR(1,3)*P(1)+GTR(2,3)*GTR(2,3)*P(2)
                     0 +GTR(3,3)*GTR(3,3)*P(3))
0225                   W(4) = F(1,1)*F(1,1)*P(4)+F(2,1)*F(2,1)*P(5)+F(3,1)*F(3,1)*P(6)
0226                   W(5) = F(1,1)*F(1,2)*P(4)+F(2,1)*F(2,2)*P(5)+F(3,1)*F(3,2)*P(6)
0227                   W(6) = F(1,1)*F(1,3)*P(4)+F(2,1)*F(2,3)*P(5)+F(3,1)*F(3,3)*P(6)
0228                   W(7) = F(1,2)*F(1,1)*P(4)+F(2,2)*F(2,1)*P(5)+F(3,2)*F(3,1)*P(6)
0229                   W(8) = F(1,2)*F(1,2)*P(4)+F(2,2)*F(2,2)*P(5)+F(3,2)*F(3,2)*P(6)
0230                   W(9) = F(1,2)*F(1,3)*P(4)+F(2,2)*F(2,3)*P(5)+F(3,2)*F(3,3)*P(6)
0231                   W(10) = F(1,3)*F(1,1)*P(4)+F(2,3)*F(2,1)*P(5)+F(3,3)*F(3,1)*P(6)
0232                   W(11) = F(1,3)*F(1,2)*P(4)+F(2,3)*F(2,2)*P(5)+F(3,3)*F(3,2)*P(6)
0233                   W(12) = F(1,3)*F(1,3)*P(4)+F(2,3)*F(2,3)*P(5)+F(3,3)*F(3,3)*P(6)
0234                   W(13) = S(1,1)*S(1,1)*P(4)+S(2,1)*S(2,1)*P(5)+S(3,1)*S(3,1)*P(6)
0235                   W(14) = S(1,1)*S(1,2)*P(4)+S(2,1)*S(2,2)*P(5)+S(3,1)*S(3,2)*P(6)
0236                   W(15) = S(1,1)*S(1,3)*P(4)+S(2,1)*S(2,3)*P(5)+S(3,1)*S(3,3)*P(6)
0237                   W(16) = S(1,2)*S(1,1)*P(4)+S(2,2)*S(2,1)*P(5)+S(3,2)*S(3,1)*P(6)
0238                   W(17) = S(1,2)*S(1,2)*P(4)+S(2,2)*S(2,2)*P(5)+S(3,2)*S(3,2)*P(6)
0239                   W(18) = S(1,2)*S(1,3)*P(4)+S(2,2)*S(2,3)*P(5)+S(3,2)*S(3,3)*P(6)
0240                   W(19) = S(1,3)*S(1,1)*P(4)+S(2,3)*S(2,1)*P(5)+S(3,3)*S(3,1)*P(6)
0241                   W(20) = S(1,3)*S(1,2)*P(4)+S(2,3)*S(2,2)*P(5)+S(3,3)*S(3,2)*P(6)
0242                   W(21) = S(1,3)*S(1,3)*P(4)+S(2,3)*S(2,3)*P(5)+S(3,3)*S(3,3)*P(6)
0243                   DO 15 K = 1,8
0244                   DO 15 L = 1,8
0245                   AP(K,L) = 0.0D+00
0246                15 AI(K,L) = 0.0D+00
0247                   AP(1,1) = 0.5D+00*W(3)+0.25D+00*(W(12)+W(21))-GBN*H
0248                   AP(2,2) = 0.5D+00*W(3)+0.25D+00*(W(12)-W(21))
0249                   AP(3,3) = 0.5D+00*W(3)-0.25D+00*(W(12)-W(21))
0250                   AP(4,4) = 0.5D+00*W(3)-0.25D+00*(W(12)+W(21))+GBN*H
0251                   AP(5,5) = -0.5D+00*W(3)-0.25D+00*(W(12)+W(21))-GBN*H
0252                   AP(6,6) = -0.5D+00*W(3)-0.25D+00*(W(12)-W(21))
0253                   AP(7,7) = -0.5D+00*W(3)+0.25D+00*(W(12)-W(21))
0254                   AP(8,8) = -0.5D+00*W(3)+0.25D+00*(W(12)+W(21))+GBN*H
0255                   AP(2,1) = W(15)/4.0D+00
0256                   AI(2,1) = W(18)/4.0D+00
0257                   AP(3,1) = W(6)/4.0D+00
0258                   AI(3,1) = W(9)/4.0D+00
0259                   AP(5,1) = 0.5D+00*W(1)+0.25D+00*(W(10)+W(19))
0260                   AI(5,1) = 0.5D+00*W(2)+0.25D+00*(W(11)+W(20))
0261                   AP(6,1) = 0.25D+00*(W(12)-W(17))
0262                   AI(6,1) = 0.25D+00*(W(14)+W(16))
0263                   AP(7,1) = 0.25D+00*(W(4)-W(8))
0264                   AI(7,1) = 0.25D+00*(W(5)+W(7))
0265                   AP(4,2) = AP(3,1)
0266                   AI(4,2) = AI(3,1)
0267                   AP(6,2) = 0.25D+00*(W(12)+W(17))
0268                   AI(6,2) = 0.25D+00*(W(14)-W(16))
0269                   AP(8,2) = W(1)/2.0D+00+(W(10)-W(19))/4.0D+00
0270                   AI(8,2) = W(2)/2.0D+00+(W(11)-W(20))/4.0D+00
0271                   AP(8,3) = AP(7,1)
0272                   AI(8,2) = AI(7,1)
0273                   AP(4,3) = AP(2,1)
0274                   AI(4,3) = AI(2,1)
```

```
0277                AR(5,3) = 0.25D+00*(W(4)+W(8))
0278                AI(5,3) = 0.25D+00*(W(5)-W(7))
0279                AR(7,3) = W(1)/2.0D+00-(W(10)-W(19))/4.0D+00
0280                AI(7,3) = W(2)/2.0D+00-(W(11)-W(20))/4.0D+00
0281                AR(8,3) = AR(6,1)
0282                AI(8,3) = AI(6,1)
0283                AR(6,4) = AR(5,3)
0284                AI(6,4) = AI(5,3)
0285                AR(7,4) = AR(5,2)
0286                AI(7,4) = AI(5,2)
0287                AR(8,4) = W(1)/2.0D+00-(W(10)+W(19))/4.0D+00
0288                AI(8,4) = W(2)/2.0D+00-(W(11)+W(20))/4.0D+00
0289                AR(6,5) = -AR(2,1)
0290                AI(6,5) = -AI(2,1)
0291                AR(7,5) = -AR(3,1)
0292                AI(7,5) = -AI(3,1)
0293                AR(8,6) = -AR(3,1)
0294                AI(8,6) = -AI(3,1)
0295                AR(8,7) = -AR(2,1)
0296                AI(8,7) = -AI(2,1)
0297                CALL HTRIDI (NM,N,AR,AI,D,E,E2,TAU)
0298                CALL IMTQL1 (N,D,E,IERR)
0299                FREQ = D(9-I)-D(I)
0300                IF(DABS(FREQQ-FREQ)-3.0D+00)16,16,17
0301             16 HF(I) = H
0302                GO TO 18
0303             17 H = H*(FREQQ/FREQ)
0304                GO TO 14
0305             18 IF(I-4)19,20,20
0306             19 I = I+1
0307                GO TO 50
0308             20 WRITE(6,25) (HF(I),I = 1,4)
0309             25 FORMAT(4F19.2)
0310                IF(J-6)26,10,10
0311             26 J = J+1
0312                GO TO 60
0313             10 IF(OMEGA-0.0D+00)121,121,90
0314             90 OMEGA = -OMEGA
0315                PSI = -PSI
0316                GO TO 65
0317            121 IF(JJ-3)150,203,203
                C
                C   NOTE: JJ=1 IS THE FIRST LAYER OF OCTAHEDRA AND JJ=3 IS THE
                C         SECOND LAYER
0318            150 JJ = JJ+2
0319                GO TO 70
0320            202 IF(THETA-4.5D+01)27,28,28
0321             28 IF(ALPHA-9.0D+01)201,202,202
0322            201 ALPHA = ALPHA+9.0D+01
0323                GO TO 170
0324             27 THETA =THETA
0325            203 CONTINUE
                    STOP
                    END
```

APPENDIX E

DIAGONALIZATION SUBROUTINES

```
0001          SUBROUTINE HTRIDI(NM,N,AR,AI,D,E,E2,TAU)
              C
0002          INTEGER I,J,K,L,N,II,NM,JP1                                        84210005
0003          REAL*8 AR(NM,N),AI(NM,N),D(N),E(N),E2(N),TAU(2,N)                  84210006
0004          REAL*8 F,FI,G,GI,H,HH,SI,SCALE                                     84210007
0005          REAL*8 DSQRT,CDABS,DABS                                            84210008
0006          COMPLEX*16 DCMPLX                                                  84210009
              C                                                                  84210010
              CC    THIS SUBROUTINE IS A TRANSLATION OF A COMPLEX ANALOGUE OF    84210011
              CC    THE ALGOL PROCEDURE TRED1, NUM. MATH. 11, 181-195(1968)      84210012
              CC    BY MARTIN, REINSCH, AND WILKINSON.                           84210013
              CC    HANDBOOK FOR AUTO. COMP., VOL.II-LINEAR ALGEBRA, 212-226(1971).  84210014
              CC                                                                 84210015
              CC    THIS SUBROUTINE REDUCES A COMPLEX HERMITIAN MATRIX            84210016
              CC    TO A REAL SYMMETRIC TRIDIAGONAL MATRIX USING                 84210017
              CC    UNITARY SIMILARITY TRANSFORMATIONS.                          84210018
              CC                                                                 84210019
              CC    ON INPUT:                                                    84210020
              CC                                                                 84210021
              CC       NM MUST BE SET TO THE ROW DIMENSION OF TWO-DIMENSIONAL    84210022
              CC         ARRAY PARAMETERS AS DECLARED IN THE CALLING PROGRAM     84210023
              CC         DIMENSION STATEMENT;                                    84210024
              CC                                                                 84210025
              CC       N IS THE ORDER OF THE MATRIX;                            84210026
              CC                                                                 84210027
              CC       AR AND AI CONTAIN THE REAL AND IMAGINARY PARTS,          84210028
              CC         RESPECTIVELY, OF THE COMPLEX HERMITIAN INPUT MATRIX.    84210029
              CC         ONLY THE LOWER TRIANGLE OF THE MATRIX NEED BE SUPPLIED.  84210030
              C                                                                  84210031
              C                                                                  84210032
0007          CONTINUE
              CC    ON OUTPUT:                                                   84210033
              CC                                                                 84210034
              CC       AR AND AI CONTAIN INFORMATION ABOUT THE UNITARY TRANS-    84210035
              CC         FORMATIONS USED IN THE REDUCTION IN THEIR FULL LOWER    84210036
              CC         TRIANGLES.  THEIR STRICT UPPER TRIANGLES AND THE       84210037
              CC         DIAGONAL OF AR ARE UNALTERED;                          84210038
              CC                                                                 84210039
              CC       D CONTAINS THE DIAGONAL ELEMENTS OF THE THE TRIDIAGONAL MATRIX;  84210040
              CC                                                                 84210041
              CC       E CONTAINS THE SUBDIAGONAL ELEMENTS OF THE TRIDIAGONAL   84210042
              CC         MATRIX IN ITS LAST N-1 POSITIONS.  E(1) IS SET TO ZERO;  84210043
              CC                                                                 84210044
              CC       E2 CONTAINS THE SQUARES OF THE CORRESPONDING ELEMENTS OF E.  84210045
              CC         E2 MAY COINCIDE WITH E IF THE SQUARES ARE NOT NEEDED;   84210046
              CC                                                                 84210047
              CC       TAU CONTAINS FURTHER INFORMATION ABOUT THE TRANSFORMATIONS.  84210048
              CC                                                                 84210049
              CC    ARITHMETIC IS REAL EXCEPT FOR THE USE OF THE SUBROUTINES      84210050
              CC    CDABS AND DCMPLX IN COMPUTING COMPLEX ABSOLUTE VALUES.       84210051
              CC                                                                 84210052
              CC    QUESTIONS AND COMMENTS SHOULD BE DIRECTED TO B. S. GARBOW,   84210053
              CC    APPLIED MATHEMATICS DIVISION, ARGONNE NATIONAL LABORATORY    84210054
              CC                                                                 84210055
              C     ------------------------------------------------------------84210056
                                                                                 84210057
0008          TAU(1,N) = 1.D0                                                    84210058
0009          TAU(2,N) = 0.D0                                                    84210059
              C                                                                  84210060
```

```
0010                DO 100 I = 1, N                                                    84210061
0011           100  D(I) = AR(I,I)                                                    84210062
                C                                                                     84210063
                C     ::::::::::: FOR I=N STEP -1 UNTIL 1 DO -- :::::::::::         84210064
0012                DO 300 II = 1, N                                                  84210065
0013                   I = N + 1 - II                                                 84210066
0014                   L = I - 1                                                      84210067
0015                   H = 0.0D0                                                      84210068
0016                   SCALE = 0.0D0                                                  84210069
0017                   IF (L .LT. 1) GO TO 130                                        84210070
                C     ::::::::::: SCALE ROW (ALGOL TOL THEN NOT NEEDED) :::::::::::  84210071
0018                   DO 120 K = 1, L                                                84210072
0019           120     SCALE = SCALE + DABS(AR(I,K)) + DABS(AI(I,K))                  84210073
                C                                                                     84210074
0020                   IF (SCALE .NE. 0.0D0) GO TO 140                                84210075
0021                   TAU(1,L) = 1.0D0                                               84210076
0022                   TAU(2,L) = 0.0D0                                               84210077
0023           130     E(I) = 0.0D0                                                   84210078
0024                   E2(I) = 0.0D0                                                  84210079
0025                   GO TO 290                                                      84210080
                C                                                                     84210081
0026           140     DO 150 K = 1, L                                                84210082
0027                      AR(I,K) = AR(I,K) / SCALE                                   84210083
0028                      AI(I,K) = AI(I,K) / SCALE                                   84210084
0029                      H = H + AR(I,K) * AR(I,K) + AI(I,K) * AI(I,K)               84210085
0030           150     CONTINUE                                                       84210086
                C                                                                     84210087
0031                   E2(I) = SCALE * SCALE * H                                      84210088
0032                   G = DSQRT(H)                                                   84210089
0033                   E(I) = SCALE * G                                               84210090
0034                   F = CDABS(DCMPLX(AR(I,L),AI(I,L)))                             84210091
                C     ::::::::::: FORM NEXT DIAGONAL ELEMENT OF MATRIX T :::::::::: 84210092
0035                   IF (F .EQ. 0.0D0) GO TO 160                                    84210093
0036                   TAU(1,L) = (AI(I,L) * TAU(2,I) - AR(I,L) * TAU(1,I)) / F       84210094
0037                   SI = (AR(I,L) * TAU(2,I) + AI(I,L) * TAU(1,I)) / F             84210095
0038                   H = H + F * G                                                  84210096
0039                   G = 1.0D0 + G / F                                              84210097
0040                   AR(I,L) = G * AR(I,L)                                          84210098
0041                   AI(I,L) = G * AI(I,L)                                          84210099
0042                   IF (L .EQ. 1) GO TO 270                                        84210100
0043                   GO TO 170                                                      84210101
0044           160     TAU(1,L) = -TAU(1,I)                                           84210102
0045                   SI = TAU(2,I)                                                  84210103
0046                   AR(I,L) = G                                                    84210104
0047           170     F = 0.0D0                                                      84210105
                C                                                                     84210106
0048                   DO 240 J = 1, L                                                84210107
0049                      G = 0.0D0                                                   84210108
0050                      GI = 0.0D0                                                  84210109
                C     ::::::::::: FORM ELEMENT OF A*U :::::::::::                     84210110
0051                      DO 180 K = 1, J                                             84210111
0052                         G = G + AR(J,K) * AR(I,K) + AI(J,K) * AI(I,K)            84210112
0053                         GI = GI - AR(J,K) * AI(I,K) + AI(J,K) * AR(I,K)          84210113
0054           180        CONTINUE                                                    84210114
                C                                                                     84210115
0055                      JP1 = J + 1                                                 84210116
0056                      IF (L .LT. JP1) GO TO 220                                   84210117
                C                                                                     84210118
```

```
0057                        DO 200 K = JP1, L                                   84210119
0058                           G = G + AR(K,J) * AR(I,K) - AI(K,J) * AI(I,K)    84210120
0059                           GI = GI - AR(K,J) * AI(I,K) - AI(K,J) * AR(I,K)  84210121
0060                  200   CONTINUE                                            84210122
                      C     ********** FORM ELEMENT OF P **********            84210123
0061                  220   E(J) = G / H                                        84210124
0062                        TAU(2,J) = GI / H                                   84210125
0063                        F = F + E(J) * AR(I,J) - TAU(2,J) * AI(I,J)         84210126
0064                  240   CONTINUE                                            84210127
                      C                                                         84210128
0065                        HH = F / (H + H)                                    84210129
                      C     ********** FORM REDUCED A **********               84210130
0066                        DO 260 J = 1, L                                     84210131
0067                           F = AR(I,J)                                      84210132
0068                           G = E(J) - HH * F                                84210133
0069                           E(J) = G                                         84210134
0070                           FI = -AI(I,J)                                    84210135
0071                           GI = TAU(2,J) - HH * FI                          84210136
0072                           TAU(2,J) = -GI                                   84210137
                      C                                                         84210138
0073                           DO 250 K = 1, J                                  84210139
0074                              AR(J,K) = AR(J,K) - F * E(K) - G * AR(I,K)    84210140
                             X                  + FI * TAU(2,K) + GI * AI(I,K)  84210141
0075                              AI(J,K) = AI(J,K) - F * TAU(2,K) - G * AI(I,K)84210142
                             X                  - FI * E(K) - GI * AR(I,K)     84210143
0076                  250   CONTINUE                                            84210144
                      C                                                         84210145
0077                  260   DO 280 K = 1, L                                     84210146
0078                           AR(I,K) = SCALE * AR(I,K)                        84210147
0079                           AI(I,K) = SCALE * AI(I,K)                        84210148
0080                  280   CONTINUE                                            84210149
                      C                                                         84210150
0081                        TAU(2,L) = -SI                                      84210151
0082                  290   HH = D(I)                                           84210152
0083                        D(I) = AR(I,I)                                      84210153
0084                        AR(I,I) = HH                                        84210154
0085                        AI(I,I) = SCALE * SCALE * H                         84210155
0086                  300 CONTINUE                                              84210156
                      C                                                         84210157
0087                        RETURN                                              84210158
                      C     ********** LAST CARD OF HTRIDI **********          84210159
0088                        END                                                 84210160
```

```
0001                  SUBROUTINE IMTQL1(N,D,E,IERR)                                   91210004
                      C                                                               91210005
0002                  INTEGER I,J,L,M,N,II,MML,IERR                                   91210006
0003                  REAL*8 D(N),E(N)                                                91210007
0004                  REAL*8 B,C,F,G,P,R,S,MACHEP                                     91210008
0005                  REAL*8 DSQRT,DABS,DSIGN                                         91210009
                      C     ------------------------------------------------------    91210010
                      C                                                               91210011
                      C     THIS SUBROUTINE IS A TRANSLATION OF THE ALGOL PROCEDURE IMTQL1,  91210012
                      C     NUM. MATH. 12, 377-383(1968) BY MARTIN AND WILKINSON,     91210013
                      C     AS MODIFIED IN NUM. MATH. 15, 450(1970) BY DUBRULLE.      91210014
                      C     HANDBOOK FOR AUTO. COMP., VOL.II-LINEAR ALGEBRA, 241-248(1971).  91210015
                      C                                                               91210016
                      C     THIS SUBROUTINE FINDS THE EIGENVALUES OF A SYMMETRIC      91210017
                      C     TRIDIAGONAL MATRIX BY THE IMPLICIT QL METHOD.             91210018
                      C                                                               91210019
                      C     ON INPUT:                                                 91210020
                      C                                                               91210021
                      C        N IS THE ORDER OF THE MATRIX;                          91210022
                      C                                                               91210023
                      C        D CONTAINS THE DIAGONAL ELEMENTS OF THE INPUT MATRIX;  91210024
                      C                                                               91210025
                      C        E CONTAINS THE SUBDIAGONAL ELEMENTS OF THE INPUT MATRIX  91210026
                      C          IN ITS LAST N-1 POSITIONS.  E(1) IS ARBITRARY.       91210027
0006                  CONTINUE                                                        91210028
                      C     ON OUTPUT:                                                91210029
                      C                                                               91210030
                      C        D CONTAINS THE EIGENVALUES IN ASCENDING ORDER.  IF AN  91210031
                      C          ERROR EXIT IS MADE, THE EIGENVALUES ARE CORRECT AND  91210032
                      C          ORDERED FOR INDICES 1,2,...IERR-1, BUT MAY NOT BE    91210033
                      C          THE SMALLEST EIGENVALUES;                            91210034
                      C                                                               91210035
                      C        E HAS BEEN DESTROYED;                                  91210036
                      C                                                               91210037
                      C        IERR IS SET TO                                         91210038
                      C          ZERO       FOR NORMAL RETURN,                        91210039
                      C          J          IF THE J-TH EIGENVALUE HAS NOT BEEN       91210040
                      C                     DETERMINED AFTER 30 ITERATIONS.           91210041
                      C                                                               91210042
                      C     QUESTIONS AND COMMENTS SHOULD BE DIRECTED TO B. S. GARBOW,  91210043
                      C     APPLIED MATHEMATICS DIVISION, ARGONNE NATIONAL LABORATORY  91210044
                      C     ------------------------------------------------------    91210045
                      C                                                               91210046
                      C     ********** MACHEP IS A MACHINE DEPENDENT PARAMETER SPECIFYING  91210047
                      C                THE RELATIVE PRECISION OF FLOATING POINT ARITHMETIC.  91210048
                      C                MACHEP = 16.000**(-13) FOR LONG FORM ARITHMETIC  91210049
                      C                ON S360 **********                             91210050
0007                  DATA MACHEP/Z3410000000000000/                                  91210051
                      C                                                               91210052
0008                  IERR = 0                                                        91210053
0009                  IF (N .EQ. 1) GO TO 1001                                        91210054
                      C                                                               91210055
0010                  DO 100 I = 2, N                                                 91210056
0011                100 E(I-1) = E(I)                                                 91210057
                      C                                                               91210058
0012                  F = 0.0D0                                                       91210059
                      C                                                               91210060
```

```
0013                DO 280 L = 1, N                                                    91210061
0014                   J = 0                                                           91210062
                C      ********** LOOK FOR SMALL SUB-DIAGONAL ELEMENT **********      91210063
0015             105   DO 110 M = L, N                                                 91210064
0016                      IF (M .EQ. N) GO TO 120                                      91210065
0017                      IF (DABS(E(M)) .LE. MACHEP * (DABS(D(M)) + DABS(D(M+1))))    91210066
                X                GO TO 120                                           91210067
0018             110   CONTINUE                                                        91210068
                C                                                                     91210069
0019             120   P = D(L)                                                        91210070
0020                   IF (M .EQ. L) GO TO 215                                        91210071
0021                   IF (J .EQ. 30) GO TO 1000                                      91210072
0022                   J = J + 1                                                      91210073
                C      ********** FORM SHIFT **********                              91210074
0023                   G = (D(L+1) - P) / (2.0D0 * E(L))                              91210075
0024                   R = DSQRT(G*G+1.0D0)                                           91210076
0025                   G = D(M) - P + E(L) / (G + DSIGN(R,G))                         91210077
0026                   S = 1.0D0                                                      91210078
0027                   C = 1.0D0                                                      91210079
0028                   P = 0.0D0                                                      91210080
0029                   MML = M - L                                                    91210081
                C      ********** FOR I=M-1 STEP -1 UNTIL L DO -- **********        91210082
0030                   DO 200 II = 1, MML                                             91210083
0031                      I = M - II                                                  91210084
0032                      F = S * E(I)                                                91210085
0033                      B = C * E(I)                                                91210086
0034                      IF (DABS(F) .LT. DABS(G)) GO TO 150                         91210087
0035                      C = G / F                                                   91210088
0036                      R = DSQRT(C*C+1.0D0)                                        91210089
0037                      E(I+1) = F * R                                              91210090
0038                      S = 1.0D0 / R                                               91210091
0039                      C = C * S                                                   91210092
0040                      GO TO 160                                                   91210093
0041             150      S = F / G                                                   91210094
0042                      R = DSQRT(S*S+1.0D0)                                        91210095
0043                      E(I+1) = G * R                                              91210096
0044                      C = 1.0D0 / R                                               91210097
0045                      S = S * C                                                   91210098
0046             160      G = D(I+1) - P                                              91210099
0047                      R = (D(I) - G) * S + 2.0D0 * C * B                          91210100
0048                      P = S * R                                                   91210101
0049                      D(I+1) = G + P                                              91210102
0050                      G = C * R - B                                               91210103
0051             200   CONTINUE                                                      91210104
                C                                                                     91210105
0052                   D(L) = D(L) - P                                                91210106
0053                   E(L) = G                                                       91210107
0054                   E(M) = 0.0D0                                                   91210108
0055                   GO TO 105                                                      91210109
                C      ********** ORDER EIGENVALUES **********                       91210110
0056             215   IF (L .EQ. 1) GO TO 250                                       91210111
                C      ********** FOR I=L STEP -1 UNTIL 2 DO -- **********          91210112
0057                   DO 230 II = 2, L                                               91210113
0058                      I = L + 2 - II                                              91210114
0059                      IF (P .GE. D(I-1)) GO TO 270                                91210115
0060                      D(I) = D(I-1)                                               91210116
0061             230   CONTINUE                                                      91210117
                C                                                                     91210118
```

```
0062          250    I = 1                                                    91210119
0063          270    D(I) = P                                                 91210120
0064          290 CONTINUE                                                   91210121
              C                                                              91210122
0065              GO TO 1001                                                 91210123
              C       :::::::::: SET ERROR -- NO CONVERGENCE TO AN           91210124
              C                  EIGENVALUE AFTER 30 ITERATIONS ::::::::::: 91210125
0066         1000 IERR = L
0067         1001 RETURN
              C       :::::::::: LAST CARD OF IMTQL1 ::::::::::
0068              END
```

VITA

Mark Allen Young

Candidate for the Degree of

Doctor of Philosophy

Thesis: RADIATION DAMAGE IN $KMgF_3$:Mn AND $NaMgF_3$

Major Field: Physics

Biographical:

Personal Data: Born at Stillwater, Oklahoma, July 22, 1950 the son of Melvin T. and Clara Jean Young.

Education: Graduated from C. E. Donart High School in 1968; received Bachelor of Science degree from Oklahoma State University, Stillwater, Oklahoma, in July, 1972; completed the requirements for the degree of Doctor of Philosophy at Oklahoma State University, Stillwater, Oklahoma in July, 1976.